On connectivity in the central nervous system

a magnetic resonance imaging study

On connectivity in the central nervous system

a magnetic resonance imaging study

PROMOTIECOMMISSIE

Promotores
  Prof. Dr. M.A.van Buchem
  Prof. Dr. M. Essig, Deutsches Krebsforschungszentrum, Heidelberg, Germany

Overige leden
  Prof. Dr. S. Mori, Johns Hopkins University, Baltimore, USA
  Prof. dr. A. Webb
  Dr. ir. M.J.P. van Osch
  Mw. Dr. L. van der Weerd

Contents

— 1 —
Introduction and aims

From a black box to neuroimaging

The aspects of the human mind and its (mal-)function have long been the realm of philosophy, religion and, since the last century, of psychology and psychiatry. Before the era of medical imaging, knowledge of the functioning of the central nervous system was sparse and based on case reports of people sustaining injuries of the brain, for instance bullet wounds, after which certain functions were impaired. Nonetheless, as early as in 1881, Mosso found a correlation between brain activity and increased delivery of oxygenated blood during activation[1], further detailed by Fulton in 1925, auscultating a patient with an occipital superficial AVM[2]. He could establish a clear response of blood flow to visual tasks thus demonstrating the neuro-vascular coupling. Neuroanatomy and the white matter connections within the brain were known from *post mortem* studies that were mainly performed in the late 1800s and the beginning of the 1900s. Later, in the mid 1900s *post mortem* cell-tracking techniques mainly applied in primates[3], yielded detailed information on brain connectivity.
Brain connectivity refers to the white matter projections between different brain regions, which is the basis for the functional networks that are needed for proper brain functioning.

Only through the advent of PET, CT and MRI in the last quarter of the last century it became possible to have a glance inside the skull of living humans. Both PET and Blood Oxygen Level Dependency (BOLD) fMRI yielded insight into functional organization of the human brain *in vivo*[4,5] but the structural connectivity between functional regions remained inaccessible.

Novel MRI-based methods hold promise for establishing the presence and nature of structural connectivity in the brain. This thesis describes the development and applications of two of such techniques: diffusion tensor imaging (DTI) and manganese enhanced MRI (MEMRI).

Brownian motion is the microscopic random movement of molecules based on thermal energy. At zero Kelvin, this random motion is completely inhibited. In the human body, the most prominent signal in MRI comes from water protons. Since the human body operates at 37.5 degrees Celsius, these protons contain thermal energy and exhibit Brownian motion. The displacement of these water protons within the body may be depending on the underlying microstructure. In high cellular tissue, the movement may be restricted by cell walls and organelles, whereas in free fluid, the movement may be fast. Thus, the strength of the Brownian motion of protons contains information on the underlying tissue microstructure.

Diffusion Tensor Imaging (DTI) is a technique that allows the characterization of spatial properties of molecular water diffusion.[6] Stejskal and Tanner showed that by using a pair of opposed gradients, MRI could be made sensitive to Brownian motion.[7] Following excitation of a specimen with a 90 degree pulse, all protons precede at the same frequency. When a short gradient is applied, the frequency of these protons is changed in a controlled fashion. This first step is called dephasing. In a second step, called dephasing, an inverted gradient is applied and all protons regain their original frequency.

In the absence of Brownian motion, 100% signal is measured before dephasing, then signal is lost due to the dephasing and after rephasing, the signal is completely recovered. However, when the particles move during the application of the gradient, the signal cannot be recovered completely. The loss of signal is proportional to the amount of diffusion weighting described by the term b following

$$b = \gamma^2 G^2 \delta^2 \left(\Delta - \delta/3 \right)$$

where γ is the gyromagnetic constant, G the gradient strength, δ the gradient duration and Δ the time from the start of the dephasing to the start of rephasing gradient. Thus, b describes the strength of the diffusion weighting used in a diffusion MRI experiment.

To calculate the diffusion constant D, at least two measurements are required. First, a measurement without diffusion weighting, for the measurement of the signal without Brownian motion also referred to as S_0. The second measurement includes the diffusion weighting gradients and the signal measured is referred to as S_i. When S_0 and S_i are known, D can be calculated following

$$S_i = S_0 \, e^{(-bD)}$$

where the only variable not known is D.

 The application of this technique to stroke revealed that D is to some extent dependent on the applied gradient direction[8]. To eliminate this direction dependency, commonly D is measured in three main directions and than averaged yielding the apparent diffusion coefficient . Here, the diffusion is uniform in all directions and called isotropic.

 In white matter, however, the strong directional dependency of the measured D also contains valuable information that should not be averaged out. This directionality has been attributed to highly directionally ordered structures like axons and myelin sheets[9]. It was shown that D is large for gradient directions along axonal tracts and is reduced perpendicular to such structures. Thus, the overall shape of the water displacement resembles an ellipsoid instead of a sphere and is referred to as anisotropic.

 This ellipsoid water displacement can be described using a 3 x 3 matrix or tensor. This tensor has three diagonal components with symmetry along this axis. Thus for a complete Diffusion Tensor Imaging (DTI) experiment, a minimum of seven measurements is required; a non-weighted image and 6 measurements with orientationally independent directions. Using DTI, both the magnitude of anisotropy and the preferential direction of water diffusion can be quantified. The magnitude is commonly described using the fractional anisotropy (FA)

$$FA = \sqrt{\frac{3}{2}} \frac{\sqrt{(\lambda_1 - \bar{\lambda})^2 + (\lambda_2 - \bar{\lambda})^2 + (\lambda_3 - \bar{\lambda})^2}}{\sqrt{\lambda_1^2 + \lambda_2^2 + \lambda_3^2}}$$

that varies from 0 to 1 where 0 represents isotropic and 1 maximal anisotropic diffusion. In highly organized white matter tracts, the FA approaches values of around 0.85 whereas in grey matter it is as low as 0.2. This measure may be used to monitor white matter diseases. Furthermore, the direction of the longest axis of this ellipsoid aligns with the direction of white matter tracts and could thus be used to reconstruct fiber tracts.

MEMRI

Contrast agents are widely used in medical imaging and the most common agents used in human applications are gadolinium chelates. The gadolinium interacts with the surrounding water protons leading to a shortening of the T_1-time where the contrast agent is present, consequently increasing the local signal. This type of contrast agents is injected intravenously and shows tissue contrast in areas with increased vessel permeability such as inflammatory lesions or tumors. Other substances are also known to cause T_1 shortening in a similar fashion and one of these is manganese[10]. In comparison to gadolinium, manganese ions (Mn^{2+}) have chemical properties that make it an interesting tracer for neuroimaging. Mn^{2+} is a divalent ion with chemical properties resembling Ca^{2+}. Since calcium-gated channels are the main trigger for release of neurotransmitters at the synaptic endplate and Mn^{2+} is actively transported into neurons via voltage-gated Ca^{2+} channels[11], it may serve as a marker for neuronal activity.

 Generally, three major applications of MEMRI have been developed: using it as a tissue contrast agent, as a surrogate marker for neuronal cell activity, and for tracing neuronal tracts. First, after systemic $MnCl_2$ injection in rodents, specific uptake patterns of Mn^{2+} giving rise to increased contrast of grey matter structures have been described[10]. Second, Mn^{2+} has been successfully used as a Ca^{2+} analogue to visualize activity-dependent uptake into the rat brain[12]. This has also been shown in songbirds, where an injection of $MnCl_2$ solution into the vocal center in the cortex gave rise to a selective pattern of Mn^{2+} uptake in the nucleus robustus archistriatalis and area X, both regions that are involved in song

formation[13]. Importantly, the amount of uptake was dependent on the level of neuronal activity[13]. Third, Pautler et al. were the first to exploit MEMRI for depicting neuronal connections. Injection of $MnCl_2$ solution into the vitreal chamber of the eye enabled visualization of optical pathways in mice[14]. In another study the same group demonstrated that once inside an axon, Mn^{2+} is transported in both antero- and retrograde direction, and that also trans-synaptic propagation of Mn^{2+} is possible[15].

General goal

The objective of this thesis was to develop and apply novel methods for the *in vivo* evaluation of the connectivity of the central nervous system under healthy conditions and in disease.

Aims

1 To validate *in vivo* DTI-based fiber tracking
2 To develop a DTI-based method that allows reproducible evaluation of fiber integrity and to apply this method to neuronal diseases
3 To develop a method for MEMRI of the spinal cord and to evaluate the potential of MEMRI to detect spinal cord damage and to monitor the effect of therapeutic interventions.

References

1 **Mosso, A.** 1881. Ueber den Kreislauf des Blutes im Menschlichen Gehirn (von Veit, Leipzig).
2 **Fulton, J. F.** Observations on the vascularity of the human occipital lobe during visual activity. 1928, Brain 51: 310–320.
3 **Heimer L,** Robarts M. 1981. Neuroanatomical Tract-Tracing Methods. New York, L, Plenum Press.
4 **Phelps, M.E.,** Mazziotta, J.C. Possitron emission tomography: human brain function and biochemistry. Science, 1985 May 17,228(4701):799-809.
5 **Turner, R.,** Howseman, A., Rees, G.E., Josephs, O., Friston, K., Functional magnetic resonance imaging of the human brain: data acquisition and analysis. Exp Brain Res. 1998 Nov;123(1-2):5-12.
6 **Basser, P. J.,** Mattiello, J., et al. 1994. MR diffusion tensor spectroscopy and imaging. Biophys. J. 66: 259–267.
7 **Stejskal, E.O.,** Tanner, J.E., 1965. Spin diffusion measurements: spin-echoes in the presence of time-dependent field gradient. J. Chem. Phys. 42, 288–292.
8 **Moonen CT,** Pekar J, de Vleeschouwer MH, van Gelderen P, van Zijl PC, DesPres D., Restricted and anisotropic displacement of water in healthy cat brain and in stroke studied by NMR diffusion imaging. Magn Reson Med. 1991 Jun;19(2):327-32.
9 **Beaulieu, C.,** Allen, P.S., 1994. Determinants of anisotropic water diffusion in nerves. Magn. Res. Med. 31, 394-400.
10 **Lin YJ,** Koretsky AP. Manganese ion enhances T1-weighted MRI during brain activation: an approach to direct imaging of brain function. Magn Reson Med 1997 Sep;38(3):378-88.
11 **Drapeau P,** Nachshen DA. Manganese fluxes and manganese-dependent neurotransmitter release in presynaptic nerve endings isolated from rat brain. J Physiol 1984 Mar;348:493-510.
12 **Aoki I,** Wu YJ, Silva AC, Lynch RM, Koretsky AP. *In vivo* detection of neuroarchitecture in the rodent brain using manganese-enhanced MRI. Neuroimage 2004 Jul;22(3):1046-59.
13 **Van der Linden A,** Verhoye M, Van Meir V, Tindemans I, Eens M, Absil P, Balthazart J. *In vivo* manganese-enhanced magnetic resonance imaging reveals connections and functional properties of the songbird vocal control system. Neuroscience. 2002;112(2):467-74.
14 **Pautler RG,** Silva AC, Koretsky AP. *In vivo* neuronal tract tracing using manganese-enhanced magnetic resonance imaging. Magn Reson Med. 1998

Nov;40(5):740-8.

15 **Pautler RG,** Mongeau R, Jacobs RE. *In vivo* trans-synaptic tract tracing from the murine striatum and amygdala utilizing manganese enhanced MRI (MEMRI). Magn Reson Med. 2003 Jul;50(1):33-9.

— 2 —

Diffusion Tensor Imaging and Axonal Tracking in the Human Brainstem

B. Stieltjes, W.E. Kaufmann, P.C.M. van Zijl, K. Fredericksen, G.D. Pearlson, M. Solaiyappan, S. Mori

Diffusion tensor MRI was used to demonstrate *in vivo* anatomical mapping of brainstem axonal connections. It was possible to identify the corticospinal tract (CST), medial lemniscus, and the superior, medial, and inferior cerebellar peduncles. In addition, the cerebral peduncle could be subparcellated into component tracts, namely, the frontopontine tract, the CST, and the temporo-/parieto-/occipitopontine tract. Anatomical landmarks and tracking thresholds were established for each fiber and, using these standards, reproducibility of automated tracking as assessed by intra- and interrater reliability was found to be high (k › 0.82). Reconstructed fibers corresponded well to existing anatomical knowledge, validating the tracking. Information on the location of individual tracts was coregistered with quantitative MRI maps to automatically measure MRI parameters on a tract-by-tract basis. The results reveal that each tract has a unique spatial signature in terms of water relaxation and diffusion anisotropy.

Introduction

The brainstem is a region charaterized by densely packed fibers travelling to and from the cerebrum and the cerebellum (Carpenter, 1976). Some of these fibers, such as the corticospinal tract and the superior cerebellar peduncle, are of critical importance in the initiation, control and execution of movement and are postulated to be involved in higher skills such as motor learning (Orioli and Strick, 1989). Others, such as the spinocerebellar tract and the inferior cerebellar peduncle, carry sensory information to the cerebellum (Yaginuma and Matsushita, 1989). Fiber bundles of the brain stem are involved in a wide spectrum of neurologic disorders, including amyotrophic lateral sclerosis, multiple sclerosis, leukodystrophys, cerebrovascular disease, and brain tumors. Thus, noninvasive *in vivo* visualization and delineation of the brainstem's white matter tracts would not only provide information about the normal neuroanatomy of brain connections, but also might improve the detection and further assessment of many neurology conditions. However, conventional radiological techniques including MRI often lack the appropriate contrast to discretely delineate white matter components of the brainstem and, as a result; their diagnostic value for the aforementioned disorders is far from optimum.

Diffusion Tensor Imaging (DTI) is a technique that can characterize the spatial properties of molecular diffusion processes (Baser et al., 1994a,b; van Gelderen et al., 1994; Mori and van Zijl, 1995). The application of this technique to the central nervous system has revealed that the diffusion of water in white matte is anisotropic. This directionality has been attributed to constraints imposed upon the water movement by the ordered structure of axons and myelin sheets (Moseley et al., 1990; Beaulieu and Allen, 1994; Henkelman et al., 1994; Pierpaoli et al., 1996). Using DTI, both the magnitude of the anisotropy and the orientation in which the water preferentially diffuses can be quantified. By combining these two parameters, anisotropy and orientation, DTI provides new and unique opportunities for studying the white matter architecture. In this study, we explore the capabilities of several types of emerging DTI methods and analysis to study the fiber

pathways in the human brainstem *in vivo*. One is the so-called color-coded map (Douek et al., 1991; Coremans et al., 1994; Nakada and Matsuzawa, 1995; Makris et al. 1997; Pajevic and Pierpaoli, 1999), which provides a template of white matter architecture based on measurements of anisotropy and orientation. Another is the three-dimensional tracking of axonal projections (Mori et al., 1999, 2000; Xue et al., 1999; Conturo et al., 1999; Basser et al., 2000; Poupon et al., 2000). Fiber bundles delineated either by color-coded maps or tracking approaches can also be examined in terms of MR properties. In this paper, we perform such a 3D-guided quantitative analysis of MR parameters of white matter on a tract-by-tract basis. We selected the brainstem for applying these methods for several reasons. First, compared to the cerebral hemispheres, many of the tracts have relatively simple trajectories with few branches. Second, there is accumulated knowledge on the trajectories of these fibers based on post-mortem anatomical studies. These advantages make the brainstem particularly suitable for the implementation and validation of DTI techniques. Using these types of DTI analysis described above, we were able to delineate the corticospinal tract, the medial lemniscus and the superior, medial and inferior cerebellar peduncles in normal young adults. In addition, the cerebral peduncle was parcellated into its fiber system components. Finally, quantification of MRI parameters on individual tracts revealed that each brainstem bundle has a unique spatial signature of water relaxation and diffusion anisotropy.

Materials and Methods

MRI Data Acquisition

Six healthy, right-handed volunteers (three males, three females), aged 22 to 32 (mean age 27) years participated in this study. All studies were performed using a 1.5-T Philips Gyroscan NT system. RF excitation on this system is performed using the body coil, leading to a highly homogeneous B_1 field over all cerebral and brainstem areas. Reception is with a head coil.

Diffusion-weighted imaging was accomplished using multislice segmented echoplanar imaging (EPI), with cardiac triggering and navigator echo phase correction (motion correction) (Ordidge et al., 1994). A data matrix of 64 x 64 over a field of view of 120 x 120 mm was obtained using acquisition of 17 echoes per excitation. Imaging slices were positioned to make the slice perpendicular to the longitudinal axis of the brainstem at the pons level. Slice thickness was 3 mm without a gap (40 slices); TE = 92 ms; TR = 5 heart beats; k-space data were zerofilled to a resolution of 1 x 1 x 3 mm before Fourier transform to image space. Diffusion weighting was performed along six independent axes, using diffusion weighting of b = 600 s/mm^2 at the maximum gradient strength of 2.1 G/cm. A reference image with low diffusion weighting (b = 33 s/mm^2) was also recorded. A single set of these seven measurements took about 4–5 min depending on the heart rate. Measurements were repeated six times to increase signal to noise. Double-echo T_2-weighted imaging (TEs of 22 and 100 ms; image resolution equal to DTI) was also performed for anatomical guidance and T_2 quantification. The entire examination was completed within 50 min. To ensure coregistration of the T_2 and DTI images, the same data acquisition scheme (EPI with 17-echo acquisition) was used for the double-echo imaging.

The brain tumor patient was a 41-year-old woman with a parasellar meningoma, diagnosed 7 years before scanning. Her clinical presentation was characterized by intermittently disturbed balance, temporary loss of voice and difficulties with swallowing. She also had minor disturbances in eye movements.

Data Processing

Data were processed on a SUN Enterprise computer. Images were first realigned using the AIR program (Woods et al., 1992), in order to remove any potential small bulk motions that occurred during the scans. Subsequently, all individual images were visually inspected to discard slices with motion artifacts. This process was needed because, in spite of the navigator echo-based motion correction, image corruption can occur due to motion during

the scan. On average, the fraction of the discarded images in this study was 2.8 +/- 2.1% (SD) for the six subjects. This is a small fraction and we do not expect it to influence signal to noise sufficiently to significantly alter anisotropy and eigenvector values. After the image quality check, the pixel intensities of the multiple diffusion-weighted images were fitted using multivariant linear least square fitting to obtain the six elements of the symmetric diffusion tensor (Basser et al., 1994). The diffusion tensors at each pixel were diagonalized to obtain eigenvalues and eigenvectors for each pixel. The eigenvector (v1) associated with the largest eigenvalue (E1) was assumed to represent the local fiber direction. Anisotropy maps were obtained using the orientation-independent fractional anisotropy (FA) (Pierpaoli and Basser, 1996). DTI-based color maps were created from FA values and the three vector elements of v1. Vector elements were assigned to red (x element, left–right), green (y, anterior–posterior), and blue (z, superior–inferior) (Makris et al., 1997; Pajevic and Pierpaoli, 1999). The intensities of the maps were scaled in proportion to the FA.

Fiber Tracking and Quantitative Analyses

Fiber tracking was performed automatically using our previously described FACT method (Mori et al., 1999; Xue et al., 1999) and a range of different threshold values for the anisotropy and the inner product (IP) between the two eigenvectors to be connected by the tracking. IP is a measure of the angle (inverse relationship) between two connected vectors, and is defined as

$$IP = V1i \times V1j$$

(i and j are indices of two connected pixels).

Briefly, tracking was initiated from a seed pixel from which a line was propagated in both retrograde and orthograde directions according to v1 at each pixel. Tracking was terminated when it reached a pixel with FA and/or IP lower than certain thresholds. These thresholds were first varied and subsequently evaluated
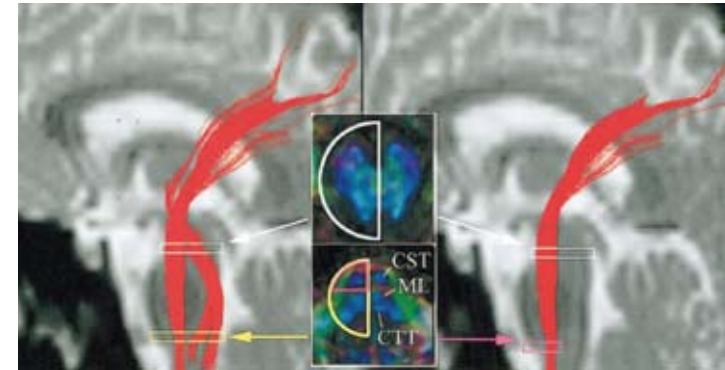
Figure 1 Effect of location and size of the reference ROI on the reconstruction of the corticospinal tract. CST, corticospinal tract; ML, medial lemniscus; CTT, central tegmental tract.

on the basis of the tracking results. There were two strategies for initiation of tracking. One was to begin tracking from each pixel included in the regions of interest (ROI). This approach could delineate only a limited number of branching patterns of the tract of interest (e.g., if the ROI contains 10 pixels, there are only 10 tracking results to delineate the tract). In the second method, fiber tracking was initiated from the center of every single pixel in the brain, but only fibers passing through chosen reference ROIS were retained (Conturo et al., 1999). In this approach, multiple tracking results penetrated the ROI, thus revealing a more comprehensive tract structure. In this study, we used the latter approach. Based on anatomical knowledge of the fiber projections in relation to landmarks, we defined multiple ROI. This principle is illustrated in figure 1 for the tracking of the CST.

Because the CST is known to be a dominant pathway that penetrates the entire brainstem, two large ROIs can be placed at the midbrain and the lower pons level that include the entire right half of the brain. The FACT method then was applied from the center of all pixels in the brain to find all tracts that penetrate these two ROIs. For this example, thresholds for FA and IP were set at 0.35 and 0.75, respectively. The results in figure 1 (left) indicate that the choice of these two large ROIs identifies several combined pathways, namely, the CST, medial lemniscus (ML), and other

tracts, possibly the central tegmental tract and/or the medial longitudinal fasciculus (CTT/MLF). Figure 1 (right) shows the result when the second ROI was changed to exclude ML and CTT/MLF, thereby reconstructing only the CST. Quantitative analyses of size and MRI properties of individual tracts were done on the basis of the established thresholds for the 3D tracking results by superimposing the fiber trajectories on coregistered FA and T2 maps.

Statistical Analysis

For statistical analysis of intra- and interrater reproducibility (reliability), two tracking results performed using the same data set were spatially superimposed. This combined image identified four groups of pixels:

1 pixels that did not contain the tract (nn),
2 pixels that contained the tract in only one of the two results (pn, np), and
3 pixels that contained the tracts in both of the results (pp).

Expected nn (Enn) = (nn + np) (nn + pn)/N
Expected np (Enp) or Epn = (nn + np) (np + pp)/N or (nn + pn)(pn + pp)/N
Expected pp (Epp) = (pn + pp)(np + pp)/N,
where N = nn + np + pn + pp is the total number of pixels.
Then κ can be determined by:
κ = (observed agreement - expected agreement)/(100 - expected agreement) where
observed agreement = (nn + pp)/N * 100
expected agreement = (Enn + Epp)/N * 100.

Expected values for each class were then calculated using the equations:

According to criteria set by Landis and Koch (1977), the κ value of 0.01–0.2 is considered as "slight," 0.21–0.4 as "fair," 0.41–0.60 as "moderate," 0.61–0.80 as "substantial," and 0.81–1.0 as "almost perfect" agreement.

Results

Effect of ROI Location and FA/IP Thresholds

In figure 2, the locations of reference ROIs that are optimized to identify each tract discretely are shown. Tracking of the CST was presented in figure 1. As long as the second reference ROI excluded the regions of the ML and CTT/MLF, and was drawn sufficiently large to contain the entire CST identifiable in the color map, the result was completely reproducible (κ = 1.0, five repeated measurements by the same operator). In practice, the first reference ROI at the midbrain level was always drawn to include only the cerebral peduncle, which could be discretely identified in the color map and is known to contain the CST as shown in figure 2a. For the ML, one ROI was placed at the medullar level close to the decussation at the medulla level (figure 2b). Contamination by adjacent tracts, most notably, the CTT/MLF was avoided by excluding them from the ROI. For the SCP, one ROI was placed in the white matter of the stem (peduncular white matter) of the cerebellum as shown in figure 2c and the other ROI at the dorsomedial aspect of the midbrain. The MCP was tracked by placing two ROIs at the left and right lateral pontine tegmentum, respectively, in a coronal section where a tract compatible with the MCP could be clearly identified on the color map (figure 2d). When the coronal slice was placed anterior to the CST level, the tracking often labeled a portion of the CST; therefore, the slice level for MCP delineation was chosen posterior to the CST. For the ICP, one ROI was placed in the lateral aspect of the rostral medulla where it could be discretely identified and the other in the white matter at the stem of the cerebellum as shown in figure 2e.

The effect of varying the two thresholds, FA and IP, on the tracking results is also shown in figure 2 (middle and right column). For all five tracts, the number of pixels selected decreased with increasing FA threshold. For relatively high FA and IP thresholds of 0.45 and 0.75, respectively, no tracking result was obtained for the MCP due to a low FA region when it crossed the midline. For two other tracts, the SCP and the ICP, the pixel count was also very low for FA > 0.45. When the FA threshold approached that of gray matter (0.15), tracking of the CST, SCP, and ML started to include
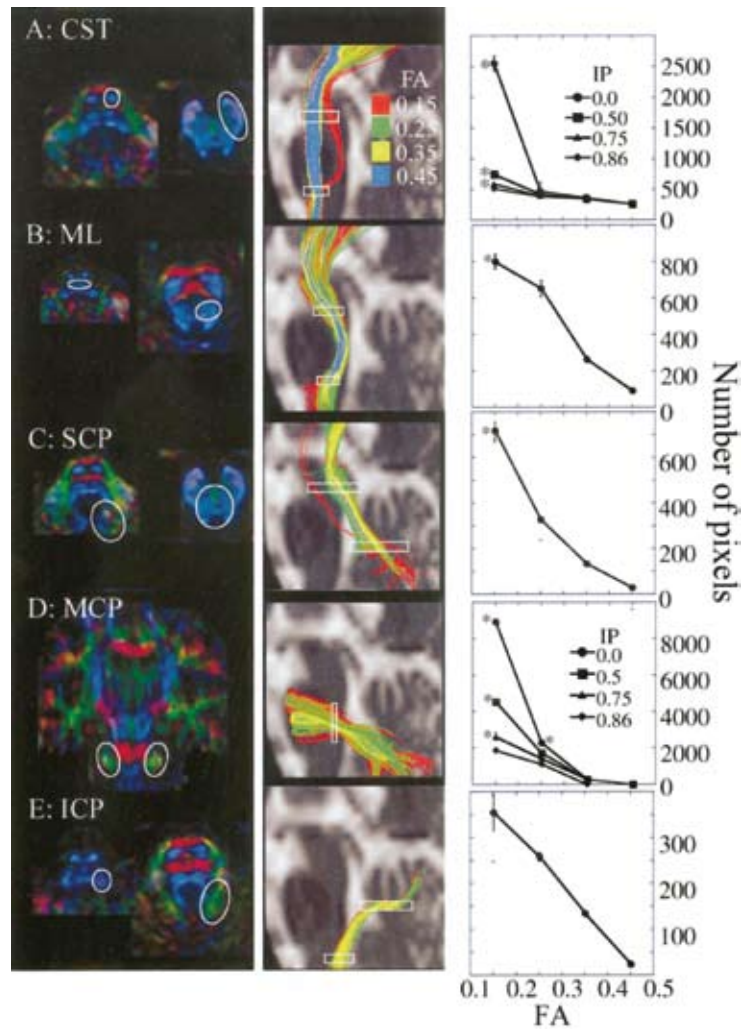
Figure 2 Locations of the anatomical reference ROIS on the DTI color map (left column) and with respect to the final tracking projected on the sagittal plane (middle column). The effect of FA (middle and right column) and IP (right column) threshold values is shown for five major tracts (A-E; specified in figure) with respect to tracking (middle column) and number of pixels (right column) included in the tracts. White boxes in the middle column indicate slice locations of the reference ROIS. The different tract colors in the middle column correspond to different tracking results for various FA threshold values. Results in the right column are the averages and standard deviations of three tracking results performed by the same rater. Asterisks in the graphs indicate that the results contained contamination by other tracts.

	FA threshold	CST	ML	SCP	MCP	ICP
Intrarater	0.25	1.0	0.931	0.886	1.0	0.972
	0.35	1.0	0.911	0.922	1.0	1.0
Interrater	0.25	0.915	0.888	0.900	0.994	0.982
	0.35	0.966	0.893	0.824	0.996	0.938

Table 1 the κ values of intra- and interrater variability for the five major tracts in the brain stem

adjacent tracts, as can be seen in the middle column graph in figure 2 (tracking results with FA > 0.15 are shown in red). Inclusion of adjacent tracts is also indicated by asterisks in the right column of figure 2. Between the FA threshold of 0.25 and 0.35, the tracking reproduced the same trajectories with respect to length and the only difference was the diameter of the trajectories (the lower the threshold, the larger the diameter). For two tracts, the CST (the tract with least curvature) and the MCP (the tract with steepest curvature), this assessment was repeated with different IP thresholds in a range of 0 (no threshold) - 0.86. The effect of varying the IP threshold was small for FA > 0.25, indicating that the FA threshold is the more stringent threshold in this range. Nonetheless, the importance of the IP threshold was apparent from the results without it, which showed significantly more contaminated pixels. For example, for the MCP, the IP threshold of 0.86 significantly reduced the number of the pixels (figure 2, MCP, the right column).

The tracking of the five major fibers bundles described above was repeated three times by the same operator using different FA (0.15 - 0.45) and IP thresholds (0.0 - 0.86). The standard deviations (error bars) of the number of pixels are presented in the right column of figure 2, which shows only small variances for an FA threshold higher than 0.25 and an IP threshold higher than 0.5. The low reproducibility with low FA threshold (FA > 0.25) is caused by higher sensitivity of the tracking result to the size of manually drawn ROI because of the inadvertent inclusion of adjacent gray matter and smaller tracts in the ROI. Intra- and interrater reproducibility of the tracking in terms of the κ value is shown in Table 1 for each tract with the FA threshold of 0.25 and 0.35, which indicates "almost perfect" agreement for all tracts (κ = 0.8).
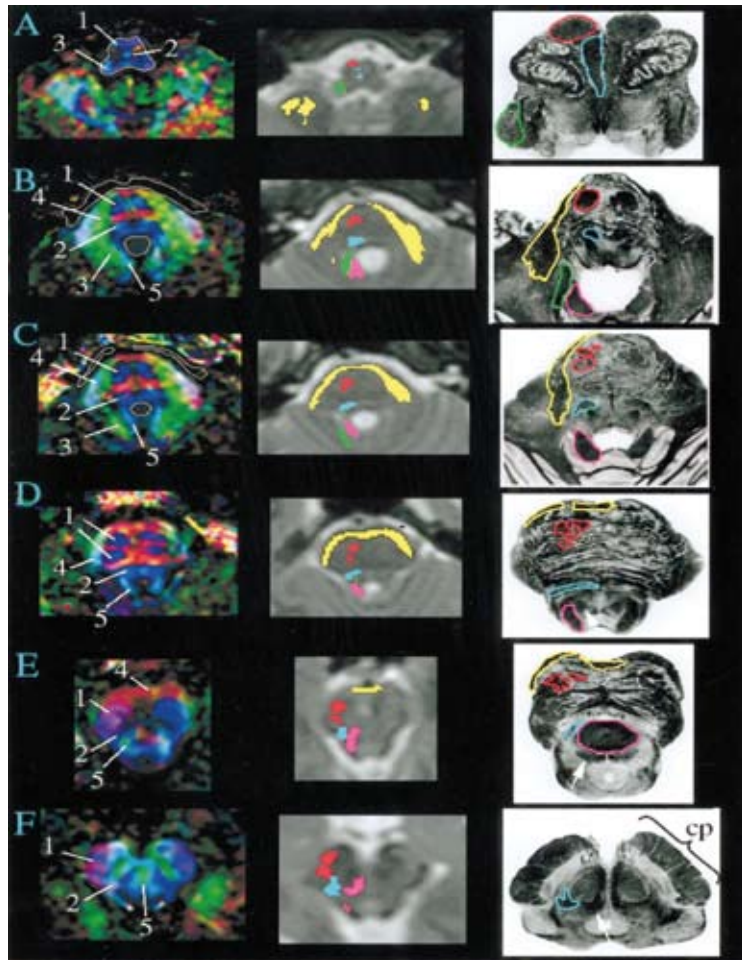
Figure 3 Comparison of DTI-based color maps, T2-weighted images, and histology for six slices in the medulla, pons, and midbrain. In the color maps (left column), red represents fibers running in the right – left direction, green ventral–dorsal (anterior – posterior), and blue rostral – caudal (superior – inferior). The intensity is scaled in proportion to the degree of diffusion anisotropy (fractional anisotropy). Numbers in the color maps represent the five major tracts reconstructed in this study. These are 1, corticospinal tract (CST); 2, medial lemniscus (ML); 3, inferior cerebellar peduncle (ICP); 4, medial cerebellar peduncle (MCP); and 5, superior cerebellar peduncle (SCP). Results of 3D tract tracking are superimposed on the T2-weighted images (second column) using color coding; red, CST; cyan, ML; green, ICP; yellow, MCP; and pink, SCP. Locations of the tracts were also specified on the histology (third column (Williams et al. 1997)) using the same color coding. White arrows in D – F indicate the locations of central tagmental tract/medial longitudinal fasciculus. cp, cerebral peduncle.
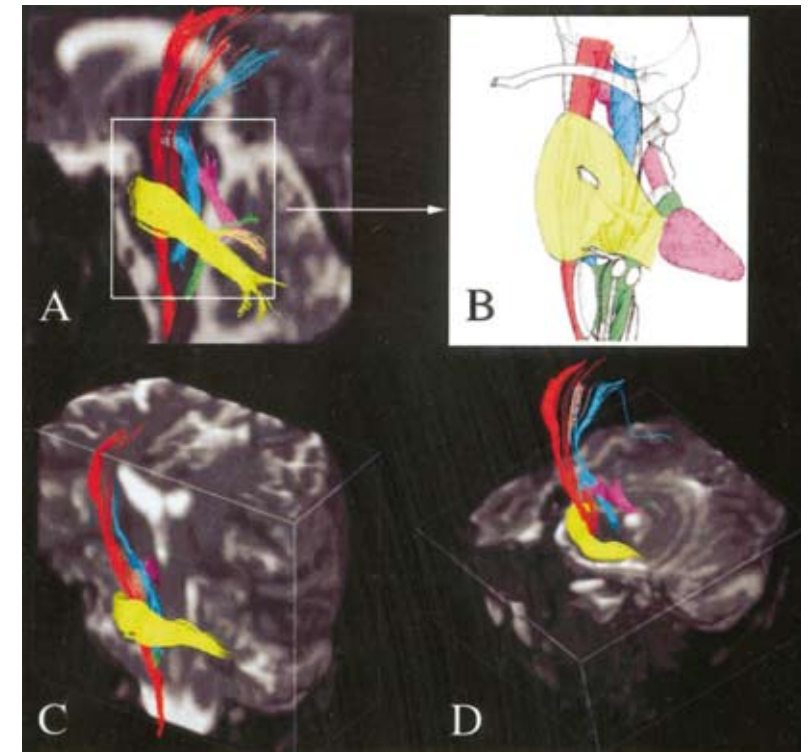
Figure 4 A three-dimensional view of reconstructed tracts (A) and comparison with *postmortem* human data (B) (modified from Nieuwenhuys et al., 1983). In (A), tracking results for the white matter bundles are superimposed on a midsagittal T2-weighted image to match the viewing angle of the postmortem data (B). Color coding is the same as fig. 3. In (C) and (D), reconstructed tracts are visualized from different view angles.

Color Maps, 3D Fiber Bundle Tracking, and Comparison with Histology

Figure 3 shows six representative slices of color maps compared to T_2-weighted images and brainstem anatomical preparations. It can first be seen that the DTI-based color maps can delineate a more complex substructure within the white matter than the T_2- weighted images. The brightness of the color maps, which reflects the magnitude of anisotropy, provides high contrast between white matter and gray matter, while the color, which

indicates orientation of tracts, differentiates various tracts within the white matter. Comparison with histological preparations (right column, adapted from Williams et al. (1997)) demonstrates that some tracts can be discretely identified in the color maps. For example, the corticospinal tract (tract 1) can be clearly delineated in the color maps at the slice levels of figures 3b–3d.

The anatomical information on color maps can be further augmented by 3D-trajectory information provided by the reconstructed fibers. Figure 4a shows the results of the automated tracking for the following major brainstem fibers: corticospinal tract (CST, red), medial lemniscus (ML, cyan blue), inferior cerebellar peduncle/spinocerebellar tract (ICP, green), middle cerebellar peduncle (MCP, yellow), and superior cerebellar peduncle (SCP, pink).

The tracking results are in high qualitative agreement with standard anatomical postmortem data (figure 4b, adapted from Nieuwenhuys et al. (1983)). Figure 3 illustrates two-dimensionally, slice-by-slice, the similarity between tracking overlaid on T$_2$-weighted images and anatomical data.

Parcellation of Homogeneously Appearing White Matter

Parcellation of the cerebral peduncle, which is known to contain three major fiber systems, the frontopontine (FPT), corticospinal, and temporo parietooccipitopontine (TPOPT) tracts, was also attempted (figure 5). For this analysis, the first reference ROI was placed to include the entire cerebral peduncle (a yellow box in the left panel of figure 5a). Differentiation among these three cerebral peduncle components was then accomplished using ROIs at the lower pons level, which only includes the CST (see the second yellow box in the right panel of figure 5). A comparison between DTI and other imaging and anatomical modalities is depicted in figure 5c. Figure 5c-4 shows the resulting tracking result superimposed on a T$_2$-weighted image at the level of the cerebral peduncle. In contrast with the homogeneous appearance on DTI anisotropy maps (figures 5c-1), white matter staining (figures 5c-2), DTI-based color maps (figures 5 c-3), and T$_2$-weighted images (figures 5c-4), 3D tracking can dissect the cerebral peduncle into three regions (figures 5c-4).
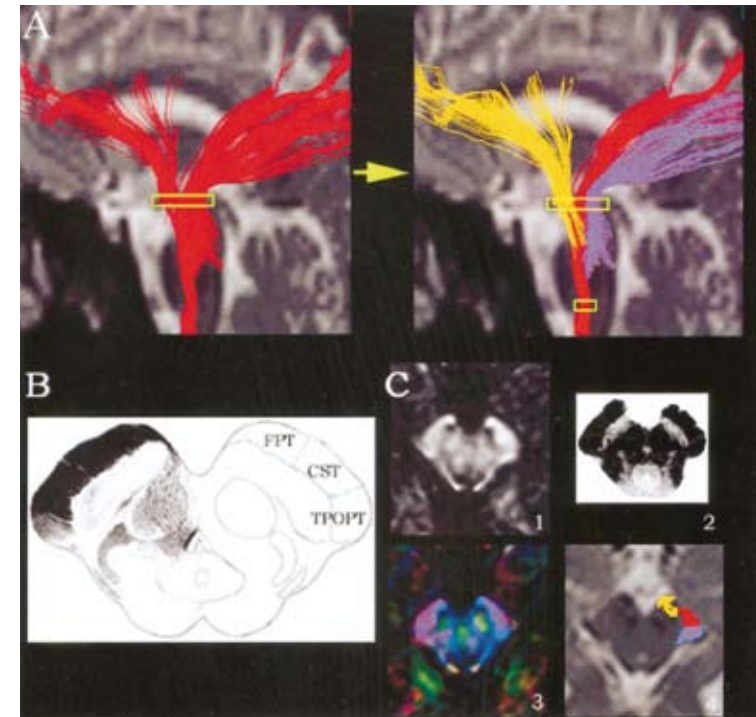
Figure 5 Parcellation of the cerebral peduncle. If one reference ROI is defined at the cerebral peduncle (indicated by a yellow box in the left panel of (A)), multiple tracts penetrating the cerebral peduncle are reconstructed. By adding the second ROI at the lower pons level (smaller yellow box in the right panel of (A)), only the CST is selected based on the knowledge that the CST penetrates both ROIs. The fibers anterior and posterior to the CST are the frontopontine (FPT, indicated by orange) and temporo /parieto-/occipitopontine (TPOPT, purple) tracts, respectively. (B) A cross-section of the pons (modified from Carpenter, 1976) shows the proposed separation of the cerebral peduncle (black wing on the left side) as based on acquired lesions and tracer studies in primates. The three regions are separated by dotted lines. (C) Images of the cerebral peduncle using various methods: (1) anisotropy map, (2) white matter staining, (3) DTI-based color map, and (4) 3D tracking superimposed on a T2-weighted image.

Intersubject Comparison

The tracking protocols discussed above were applied to five additional subjects. The results are shown in figure 6 for cross-sections through the medulla, pons, and midbrain levels. The CST (red), ML (cyan blue), SCP (pink), and ICP (green) were reproducibly
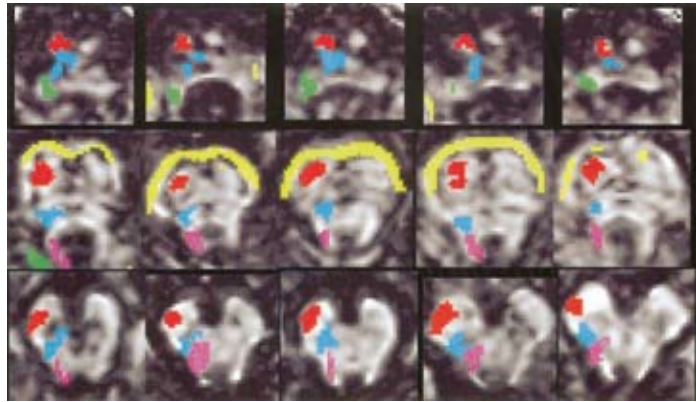
Figure 6 Tracking results of the five major tracts in the five other volunteers at three different slice levels (the medulla, pons, and midbrain). Tracking was performed using the FA threshold of 0.35 and IP threshold of 0.75 except for the MCP for which a FA threshold of 0.25 was used. Color coding is as in figure 3.

reconstructed. At the midbrain level, trajectories of the SCP (pink) had small variations and failed to reach the decussation level of SCP for one subject. This medial tegmental region of the rostral brainstem contains several small tracts, such as central tegmental tract and medial longitudinal fasciculus (figure 3, white arrows), which, with the current imaging resolution, could not be resolved from the SCP. The MCP forms a thin sheetlike structure at the ventral pontine level that could be well reproduced in five out of six subjects, but only partially reproduced in one subject.

Tract-Specific Quantitative MRI

As seen in figures 1–5, DTI analysis provides detailed information on the anatomy of white matter tracts with respect to their locations and trajectories. This capability of delineating individual white matter tracts enabled us to specifically define intrinsic fiber bundle properties using several MRI modalities. To achieve this, we used coregistered MRI data that reflected diffusion properties (FA maps) and water relaxation (T_2 maps). Profiles of FA and T_2 for different tracts along the rostrocaudal (CST, ML, SCP, and ICP)
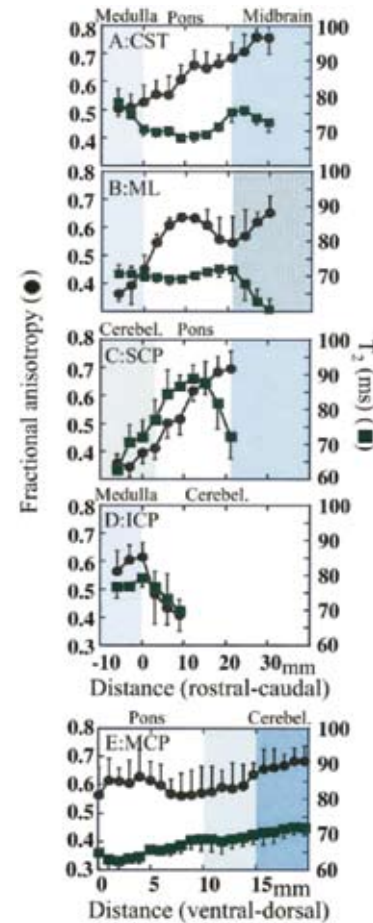
Figure 7 Tract-specific determination of water diffusion anisotropy (FA) and T2 for the CST (A), ML (B), SCP (C), ICP (D), and MCP (E), obtained using a FA threshold of 0.25 and an IP threshold of 0.75. FA and T2 values are plotted along the rostral–caudal axis (0 represents the beginning of the pons) except for MCP, which is plotted along the ventral–dorsal axis (0 represents the ventral end of the pons). Data show the average of six subjects 6 +/- SD.
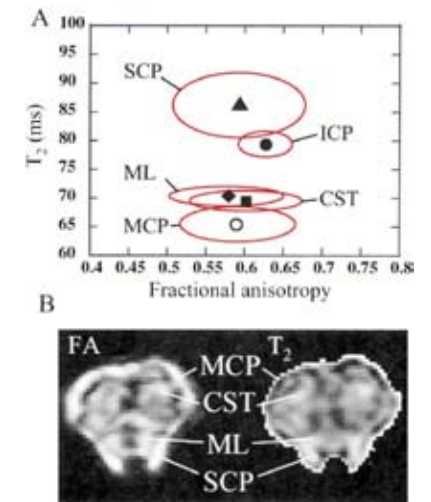
Figure 8 Correlation between FA and T2 of each tract at the pons level (A) and images of FA (left) and T2 (right) maps at a slice of the pons level (B). Abbreviations are as in figure 1.
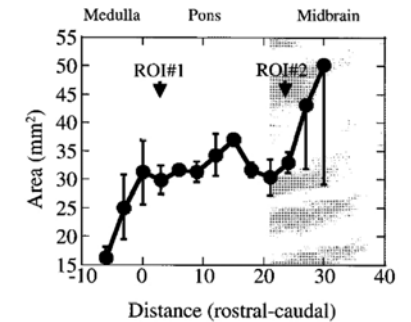
Figure 9 Cross-sectional areas of the CST along the rostral–caudal axis determined from the number of pixels labeled by the automatic tracking technique. Results are the averages and standard deviations of two separate measurements on the same subject.

or ventral– dorsal (MCP) axis are illustrated in figures 7. These results, averaged over six healthy volunteers, were obtained by normalizing brainstem length based on two anatomical landmarks (upper most rostral and caudal pontine slices). The data indicate that fibers in the brainstem have distinctive anisotropy and T_2 variations over their trajectories. For example, the CST has progressively increasing anisotropy from the rostral medulla to the caudal midbrain, while its T_2 is reduced at the pons level compared to the medulla and midbrain. Although the SCP has a FA profile that is somewhat similar to that of the CST, it has much longer T_2 in most levels of the pons. The MCP, on the other hand, is featured by short T_2. Figure 8a shows the relationship between T_2 and FA values for different tracts at the pons level. These characteristic T_2 properties of each tract can be also clearly appreciated from the FA and T_2 maps shown in figure 8b. Regression analysis between the two parameters for each tract within the brainstem results in R_2 = 0.210 (CST), 0.056 (ML), 0.092 (SCP), 0.148 (MCP), and 0.152 (ICP) indicating little to no correlation. Delineation of fiber bundles also allowed estimates of their size. For example, the slice-by-slice cross-sectional area of the CST for two separate scan sessions on the same subjects is shown in figure 9. It can be seen that the CST decreases in size along the rostral–caudal axis. Relatively large deviations outside the two ROIs were observed, which are due to less constraint in the tracking and the fact that the CST changes rapidly in size in these regions.

Discussion

The DTI results for the human brainstem in figures 1-9 and Table 1 show the high sensitivity and validity of a combined DTI color map–fiber tracking for delineating and characterizing major fiber bundles. The fiber tracking results show that the CST, ML, SCP, MCP, and ICP can be reliably mapped using DTI based on the thresholds defined in the previous section (FA = 0.25-0.35 and IP = 0.75). Qualitative comparison with postmortem human data shows excellent agreement between the *in vivo* DTI and anatomical data, thereby validating the fiber-tracking DTI approach. Individual

tracts were shown to have specific signatures in terms of T_2 relaxation and fiber anisotropy variation over the brainstem. In view of these results it is important to discuss the relative advantages of using 2D color map and 3D tracking approaches and the effect of appropriate choice of image plane, spatial resolution, reference ROIs, and tracking thresholds. In addition, the finding of negligible correlation between the tract-specific relaxation and anisotropy needs to be assessed.

Characterization of Fiber Bundles by 2D Color Maps and 3D Fiber Tract Reconstruction

Among anatomic components of the CNS, the brainstem is characterized by its relatively simple white matter architecture. Moreover, the trajectories of most major brainstem fiber bundles have been well defined by conventional postmortem anatomical techniques. For these reasons, in addition to its clinical importance we consider the brainstem a particularly suitable region for evaluating the feasibility and validity of novel DTI analyses. Two-dimensional color maps could be used to delineate several of the major brainstem tracts at levels in which conventional imaging techniques, and even standard neuroanatomical preparations, are largely unrevealing. The usefulness of color maps has been previously demonstrated for the brainstem and other CNS regions by Makris et al. (1997) and Pajevic and Pierpaoli (1999). Slice-by-slice identification of a particular tract in color maps is, however, not always straightforward due to the existence of adjacent fibers with a similar color (orientation) or due to changes in color as the tract changes direction within or through slices. Therefore, to identify the trajectories of tracts of interest unambiguously, computer-aided tracking was highly beneficial. This point was demonstrated in figure 5, in which the locations of the CST, FPT, and FPOPT were identified within the homogeneous-looking cerebral peduncle. Another example is the medial cerebellar peduncle (MCP, figures 3b-3d), for which the color transition (green–red–green) in the color maps may potentially suggest that it has a U-shape

trajectory around the pons within the axial plane. However, our 3D tracking results and post-mortem studies (figure 4) show that the actual trajectory of the MCP is significantly tilted in the dorsal–ventral axis especially at the superior part of the pons, which is very difficult to appreciate from color maps.

Methodological Limitations for Tracking

Data acquisition

For 3D fiber tracking using the FACT approach, several factors influence the results. The most notable are the choice of image plane and the in-plane spatial resolution. These choices influence the magnitude of the partial volume effect between image pixels, which is the result of limitations in resolution (voxel 2 x 2 x 3 mm, resolution-enhanced or zero-filled to 1 x 1 x 3 mm). One practical and effective way to reduce this problem is to use an imaging plane perpendicular to the orientation of tracts of interest, which is especially practical in the brainstem, where partial volume effects caused by the thick slice (3 mm) are not detrimental. Choice of in-plane resolution is determined by practical considerations such as available signal-to-noise ratio (SNR) and sensitivity to bulk motion. These two highly related issues (resolution and SNR) really depend on the sizes of tracts of interest, because white matter tracts that are smaller than the pixel size cannot be reliably reconstructed. This means that the appropriate tracking protocol (locations of ROIs and choice of thresholds) may differ for each white matter tract and specific resolution and SNR.

Data processing

In view of these limitations in data acquisition, we focused first on only the well documented large white matter tracts and employed a multiple-ROI approach that is based on existing anatomical knowledge. If only one ROI were used, the result would be highly susceptible to the partial volume and noise effects or contamination by merging or closely located parallel tracts. However, by using multiple ROIs, tracking results that
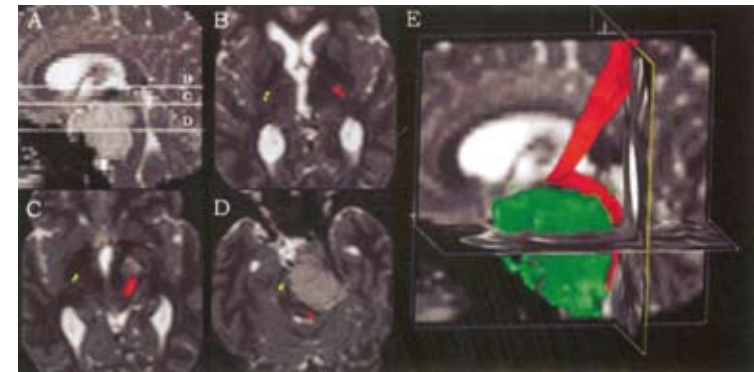
Figure 10 Deformation of the corticospinal tract in a patient with a meningioma. (A) Midsagittal T2-weighted image showing the extent of the tumor. (B-D) T2-weighted axial images with superimposed the left (yellow) and right (red) corticospinal tract. The section level is indicated on (A). (E) Triplanar view of the tumor rendered in green and the right CST in red.

deviate from the real trajectory are not likely to penetrate other ROIs by chance, thus, increasing the accuracy of the resulting fiber location. The comparison between tracking results and anatomical data indicate that this is indeed the case. One disadvantage of this approach is that branching patterns of tracts of interest between the two reference ROIs cannot be studied. While this approach may sometimes preclude the study of anatomically not well-described trajectories (i.e., for cases where two anatomical landmarks can not be specified), this approach can still be applied to brains with deformed anatomy as long as an appropriate set of reference ROIs can be chosen.

An example of such a situation is given in figure 10, for a patient with a brainstem meningioma, where the tracts have been pushed outside the normal area in the brainstem region. The two anatomical landmarks for the CST described in figure 2 could not be discretely identified in this patient. However, it was still possible to track the CST by choosing two new appropriate ROIs, one at the medulla and the other at the posterior limb of the internal capsule, which were both outside the deformed areas and thus could be easily identified.

It should be clear from figure 2 that, in addition to the choice of reference ROIs, the tracking results depend on two other

subjective parameters chosen by raters, namely, the FA and IP thresholds that determine the termination of fiber tracking. Examination of the effects of these thresholds (figure 2) showed that a FA threshold equivalent or lower than the upper gray matter FA limit (0.15) induced significant levels of contamination in three of the five tracts when using the IP threshold of 0.75 (CST, SCP, and ML). On the other hand a FA threshold higher than 0.45 was too stringent for the three cerebellar peduncles. When using a FA threshold of between 0.25 and 0.35, the effect of the IP threshold was minimal over the 0.5–0.86 range. Based on these analyses, we recommend the use of FA between 0.25–0.35 and an IP of 0.75 for our present resolution and SNR. With the ROI placement protocol and suggested FA/IP thresholds described above, intra- and interrater reliability and tract configuration agreement among the six studies subjects for the five major tracts were excellent (see table 1, figure 6).

In addition to the five fibers that could be reproducibly tracked in this study, we could identify portion of other smaller tracts at some limited slice levels. These were the MLF and CTT (see figures 1 and 3). However, these tracts were not large enough to be reliably reconstructed at the imaging resolution used in this study. The computational time for the exhaustive search of tracts that penetrate the two ROIs was about 5–10 min with FA > 0.35 and 10–15 min with FA > 0.25 using an 866 MHz Pentium III processor.

Tract-Specific MRI Studies

The information of the 3D tract trajectories was superimposed on coregistered MR images, allowing the measurement of tract-specific MRI parameters along afiber bundle (Xue et al., 1999; Virta et al., 1999). It should be noted that measured FA values depend on FA threshold used for the fiber tracking. If a lower FA threshold is used for tracking, more marginal regions of the tract are included in the tracking results, leading to lower average FA values for the tract. In figure 7, FA and IP thresholds of 0.25 and 0.75, respectively, were used for the tracking. When FA > 0.35 was used, average FA values of each tract increased by approximately 0.05. On the other hand, the characteristic profiles of the FA and T_2 of each tract as a

function of position were preserved regardless of the FA threshold (0.25-0.35). When correlating the FA and T_2 data for the individual tracts, no correlation was found. This is an important result in terms of understanding fiber properties and the origin of anisotropy. Anisotropy has been postulated to be related to the degree of fiber organization, which could reflect both axonal and myelin influences, although recent work by Beaulieu and Allen suggests a predominantly axonal origin (Beaulieu and Allen, 1994). T_2, on the other hand, has been related to myelin water content (MacKay et al., 1994; Stanisz et al., 1999). As a consequence, the profiles in figure 7 may thus reflect the unique architecture of each fiber in terms of axon-to-myelin ratio. The data indicate that these MRI parameters can vary along the fiber pathway trajectory as well. However, at the present resolution care has to be taken in directly interpreting the data in terms of axon and myelin contributions because of tracts that may be bending, crossing, merging, and fanning. Nonetheless, this tract-specific approach has the potential to increase the sensitivity and specificity of analyses of white matter lesions.

Continued Tracking of Brain Stem Fibers into the Cerebrum

Tracking of the CST showed its trajectories not only in the brainstem but also in the cerebral hemispheres (figures 1, 4, and 5). Portions of two other tracts, SCP and ML reached the thalamus, after which some fibers continued to project from the thalamus to the corona radiata and to cortical areas. While these axonal projections into the cerebrum are of great interest, care must be taken to interpret these tracking results because they lie outside of the region selected by the two reference ROIs. As a consequence, these results are more susceptible to noise and partial volume effects, and, as such, have high sensitivity to threshold choice, as can be appreciated from figure 2. Further complications arise due to the lack of precise anatomical knowledge on the trajectories of these fibers in the cerebral hemisphere (Crick and Jones, 1993). Because of these factors, we did not analyze these cerebral regions here. On the other hand, this study developed principles for applying the same approach to the cerebral hemispheres. By using the two-ROI approach, the

FA threshold of 0.25-0.35, and the IP threshold of higher than 0.75, identified trajectories by the FACT technique are likely to be valid. In addition, promising techniques were proposed recently that can reduce the resolution and SNR are under development and should further reduce the variability of tracking results.

In summary, using a combination of high-resolution *in vivo* DTI methods and analyses, we were able to delineate and reconstruct several major brainstem tracts in agreement with standard neuroanatomical knowledge. These 3D data provided greater information about white matter composition than conventional MRI sequences. Specifically, we delineated white matter tracts in 2D and 3D spaces (figures 1-4) and parcellated homogeneous white matter into different components using the information of 3D trajectories (figure 5). Analyses using coregistered images demonstrated the feasibility of combining DTI with other MRI modalities, providing information on tract-specific properties such as anisotropy, T_2, and cross-sectional area (figures 7–9).

Because the brainstem has relatively simple and well-defined white matter architecture, which has been documented by anatomical data, our study could demonstrate the feasibility and validity of applying DTI color maps and automated fiber tracking-based analyses. As such, these results provide a basis for applying this technology to other brain areas, where this information is not available.

Acknowledgements

References

- **Basser, P. J.**, Mattiello, J., et al. 1994a. MR diffusion tensor spectroscopy and imaging. Biophys. J. 66: 259–267.
- **Basser, P. J.**, Mattiello, J., et al. 1994b. Estimation of the effective self-diffusion tensor from the NMR spin echo. J. Magn. Reson. 103: 247–254.
- **Basser, P. J.**, Pajevic, S., et al. 2000. In vitro fiber tractography using DT-MRI data. Magn. Reson. Med. 44: 625–632.
- **Beaulieu, C.**, and Allen, P. S. 1994. Determinants of anisotropic water diffusion in nerves. Magn. Reson. Med. 31: 394–400.
- **Carpenter, M.** 1976. Human Neuroanatomy. Williams & Wilkins, Baltimore.
- **Conturo, T. E.**, Lori, N. F., et al. 1999. Tracking neuronal fiber pathways in the living human brain. Proc. Natl. Acad. Sci. USA 96: 10422–10427.
- **Coremans, J.**, Luypaert, R., et al. 1994. A method for myelin fiber orientation maping using diffusion-weighted MR images. Magn. Reson. Imag. 12: 443–454.
- **Crick, F.**, and Jones, E. 1993. Backwardness of human neuroanatomy. Nature 361: 109–110.
- **Douek, P.**, et al. 1991. MR color mapping of myelin fiber orientation. J. Comput. Assist. Tomogr. 15: 923–929.
- **Henkelman, R.**, Stanisz, G., et al. 1994. Anisotropy of NMR properties of tissues. Magn. Reson. Med. 32: 592–601.
- **Landis, J. R.**, and Koch, G. G. 1977. The measurement of observer agreement for categorical data. Biometrics 33: 159–174.
- **MacKay, A.**, Whittall, K., et al. 1994. *In vivo* visualization of myelin water in brain by magnetic resonance. Magn. Reson. Med. 31: 673–677.
- **Makris, N.**, Worth, A. J., et al. 1997. Morphometry of *in vivo* human white matter association pathways with diffusion weighted magnetic resonance imaging. Ann. Neurol. 42: 951–962.
- **Mori, S.**, Crain, B. J., et al. 1999. Three dimensional tracking of axonal projections in the brain by magnetic resonance imaging. Ann. Neurol. 45: 265–269.
- **Mori, S.**, Kaufmann, W. K., et al. 2000. *In vivo* visualization of human neural pathways by MRI. Ann. Neurol. 47: 412–414.
- **Mori, S.**, and van Zijl, P. C. M. 1995. Diffusion weighting by the trace of the diffusion tensor within a single scan. Magn. Reson. Med. 33: 41–52.
- **Moseley, M. E.**, Cohen, Y., et al. 1990. Diffusion-weighted MR imaging of anisotropic water diffusion in cat central nervous system. Radiology 176: 439–445.
- **Nakada, T.**, and Matsuzawa, H. 1995. Three-dimensional anisotropy contrast magnetic resonance imaging of the rat nervous system: MR axonography.

Neurosci. Res. 22: 389–398.

- **Nieuwenhuys, R.**, Voogd, J., et al. 1983. The Human Central Nervous System. Springer-Verlag, Berlin.
- **Ordidge, R. J.**, Helpern, J. A., et al. 1994. Correction of motional artifacts in diffusion-weighted NMR images using navigator echoes. Magn. Reson. Imag. 12: 455–460.
- **Orioli, P.**, and Strick, P. 1989. Cerebellar connections with the motor cortex and the arcuate premoter area: An analysis employing retrograde transneuronal transport of WGA-HRP. J. Comp. Neurol. 22: 612–626.
- **Pajevic, S.**, and Pierpaoli, C. 1999. Color schemes to represent the orientation of anisotropic tissues from diffusion tensor data: Application to white matter fiber tract mapping in the human brain. Magn. Reson. Med. 42: 526–540.
- **Pierpaoli, C.**, and Basser, P. J. 1996. Toward a quantitative assessment of diffusion anisotropy. Magn. Reson. Med. 36: 893–906.
- **Pierpaoli, C.**, Jezzard, P., et al. 1996. Diffusion tensor MR imaging of human brain. Radiology 201: 637–648.
- **Poupon, C.**, Clark, C. A., et al. 2000. Regularization of diffusion based direction maps for the tracking of brain white matter fascicules. NeuroImage 12: 184–195.
- **Stanisz, G.**, Kecojevic, A., et al. 1999. Characterizing white matter with magnetization transfer and T2. Magn. Reson. Med. 42: 1128–1136.
- **van Gelderen, P.**, de Vleeschouwer, M. H., et al. 1994. Water diffusion and acute stroke. Magn. Reson. Med. 31: 154–163.
- **Virta, A.**, Barnett, A., et al. 1999. Visualizing and characterizing white matter fiber structure and architecture in the human pyramidal tract using diffusion tensor MRI. Magn. Reson. Imag. 17: 1121–1133.
- **Williams, T. H.**, Gluhbegovic, N., et al. 1997. The Human Brain: Dissections of the Real Brain. Virtual Hospital, University of Iowa, http://www.vh.org/Providers/Textbooks/BrainAnatomy.
- **Woods, R. P.**, Cherry, S. R., et al. 1992. Rapid automated algorithm for aligning and reslicing PET images. J. Comput. Assist. Tomogr.16: 620–633.
- **Xue, R.**, van Zijl, P. C. M., et al. 1999. *In vivo* three-dimensional reconstruction of rat brain axonal projections by diffusion tensor imaging. Magn. Reson. Med. 42: 1123–1127.
- **Yaginuma, H.**, and Matsushita, M. 1989. Spinocerebellar projections from the upper lumbar segments in the cat, as studied by anterograde transport of wheat germ agglutinin-horseradish peroxidase. J. Comp. Neurol. 281: 298–319.

40

— 3 —

Imaging cortical association tracts in the human brain using diffusion-tensor-based axonal tracking

S. Mori, W. E. Kaufmann, C. Davatzikos, B. Stieltjes, L. Amodei, K. Fredericksen, G.D. Pearlson, E.R. Melhem, M. Solaiyappan, G.V. Raymond, H.W. Moser, P.C.M. van Zijl

Diffusion-tensor fiber tracking was used to identify the cores of several long-association fibers, including the anterior (ATR) and posterior (PTR) thalamic radiations, and the uncinate (UNC), superior longitudinal (SLF), inferior longitudinal (ILF), and inferior fronto-occipital (IFO) fasciculi. Tracking results were compared to existing anatomical knowledge, and showed good qualitative agreement. Guidelines were developed to reproducibly track these fibers *in vivo*. The interindividual variability of these reconstructions was assessed in a common spatial reference frame (Talairach space) using probabilistic mapping. As a first illustration of this technical capability, a reduction in brain connectivity in a patient with a childhood neurodegenerative disease (X-linked adrenoleukodystrophy) was demonstrated.

Introduction

Complex cognitive and behavioral processes that involve different functional areas of the brain are mediated by neural networks. The ability to identify and characterize the axonal fiber bundles comprising these networks is important for understanding normal as well as pathological processes affecting higher cerebral functions. Most studies of axonal fiber tracts to date have relied on invasive *in vivo* techniques in animals or ex vivo postmortem human tissue analyses[1,2]. In addition, noninvasive radiological techniques, such as conventional MRI, have been able to parcellate only small portions of the white matter into specific tracts in restricted brain regions[3,4]. Consequently, knowledge concerning these pathways *in vivo* is based mainly on primate–human extrapolations.[2] In the last decade, diffusion imaging has been shown to be directionally dependent in the white matter (anisotropic diffusion)[5-7], which has been attributed to the organization of axonal fibers and their myelin sheaths. The magnitude and orientation of this anisotropy can be assessed using diffusion-tensor imaging (DTI)[8-11], which has shown that brain regions with a high density of axonal fibers (e.g., deep white matter) have a high anisotropy. Using DTI and newly developed data processing (tract-tracing) techniques, we have recently shown the capability to perform delineation and 3D reconstruction of the cores of some axonal fiber bundles in animals[12,13], resulting in MR images that agree with standard anatomical data. Further application of this methodology to the study of healthy volunteers has confirmed the feasibility of this emerging technique for human studies.[14-19] However, several crucial steps are still necessary to allow a comprehensive use of this technique for the assessment of the anatomy of human connectivity. These steps include the establishment of procedures to reconstruct reproducibly the fiber trajectories in different individuals, and the validation of their origin through comparison with existing neuroanatomical knowledge. Although the latter validation can only be qualitative for human studies, it remains essential. This work describes our first efforts towards this goal, in which we illustrate the capability of the 3D tracking technique to identify the cores of several long-association fibers.

The interindividual variability of these reconstructions is subsequently assessed in a common spatial cerebral reference frame (Talairach space) using probabilistic mapping. Fiber assignment in such a generalized reference frame is a prerequisite for developing tracking protocols as well as for establishing normative databases that can assist in the interpretation of pathological changes.

Methods and Materials

MRI Data Acquisition

All studies were performed using a 1.5 T Philips Gyroscan NT system. Diffusion-weighted imaging was accomplished using multislice, segmented echo-planar imaging (EPI) with cardiac triggering and navigator echo phase correction (motion correction). A data matrix of 128 x 95 over a field of view (FOV) of 230 x 173 mm was obtained using an acquisition of 15 echoes per excitation. Slice thickness was 3 mm (40–60 slices), with a TE of 92 ms and TR of five heartbeats. Diffusion weighting was performed along six independent axes, using a b-value of 600 s/mm^2 at the maximum gradient strength of 21 mT/m. A reference image with low-diffusion weighting (b= 33 s/mm^2) was also recorded. A single set of these seven measurements took 5–8 min. These measurements were repeated six times to increase the signal-to-noise ratio (SNR). Double-echo T_2-weighted (TEs of 22 and 100 ms; image resolution equal to diffusion-tensor imaging (DTI)) and T_1-weighted imaging were also performed for anatomical guidance, and the entire exam was completed within 1 hr. Recent studies have shown biexponential behavior of the signal decay in the central nervous system (CNS) tissue, and the b-value of 600 s/mm^2 used in this study predominantly samples the fast-diffusing component.[20]

Data Processing

Images were first realigned using the Automated Image Registration (AIR) program to remove any potential small bulk motions that occurred during the scans. Subsequently, all individual images were visually inspected to discard slices with motion artifacts, after which the remaining images were added for each slice. The pixel intensities of the multiple diffusion-weighted images were then fitted to obtain the six elements of the symmetric diffusion tensor. The diffusion tensors at each pixel were diagonalized to obtain pixel eigenvalues and eigenvectors. An eigenvector (v1) associated with the largest eigenvalue (λ1) was assumed to represent the local fiber direction. For anisotropy mapping, the orientation-independent fractional anisotropy (FA)[21] was used.

Fiber Tracking

Tract tracking was performed using our previously-described fiber assignment by continuous tracking (FACT)[12] method. Briefly, tracing was initiated from a seed pixel from which a line was propagated in both retrograde and orthograde directions according to v1 at each pixel. The tracking was terminated when it reached a pixel with FA lower than a threshold of 0.25, or when the inner product between the two eigenvectors to be connected by the tracking was smaller than 0.75. In order to reconstruct branching patterns, the tracking was performed from every pixel inside the brain, but only fibers that penetrated regions of interest (ROIs) defined from anatomical landmarks were retained.[14] One or two ROIs were drawn for each tract of interest at anatomical landmarks where the tracts were discretely identified.

Statistical Maps

T_1 images were first resliced parallel to the anterior commissure-posterior commissure (AC-PC) plane, in accordance with the Talairach atlas. The same reslicing parameters were subsequently
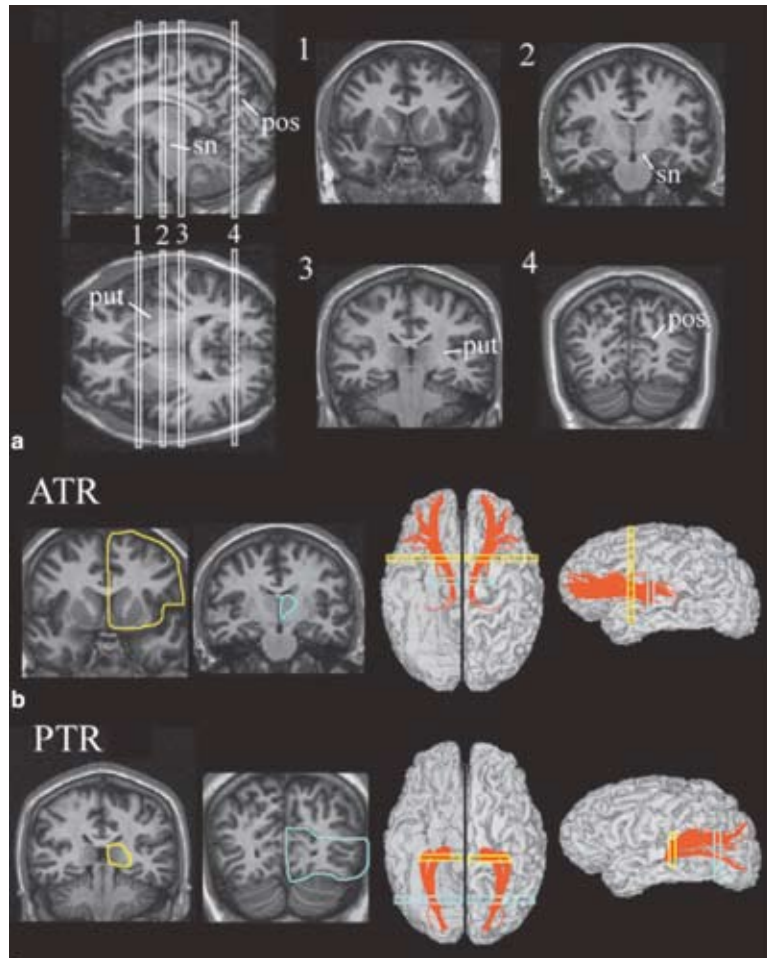
Figure 1 Guidelines for tracking the cortical association fibers. a: The locations of reference ROIs necessary to track particular fibers on four coronal slices (A1-A4). Location A1 is at the slice level where the frontal and temporal lobes are separated. Location A2 is where the anterior part of substantia nigra first appears. Location A3 is at the posterior tip of the putamen. Location A4 is at the parietooccipital sulcus, and is identified at the middle of the coronal slice along the superior-inferior axis. b–f: Locations of the reference ROIs for each tract are shown together with reconstruction results. The first and second columns show the coronal ROI locations. The third and fourth columns show the ROI locations and reconstruction results projected onto the 3D axial (both superior and inferior views) and sagittal planes, respectively. b: For anterior thalamic radiation (ATR), which connects the frontal lobe and thalamus, one ROI defines the frontal lobe (slice level A1) and the other the anterior part of thalamus at slice level A2. c: For the posterior thalamic radiation,
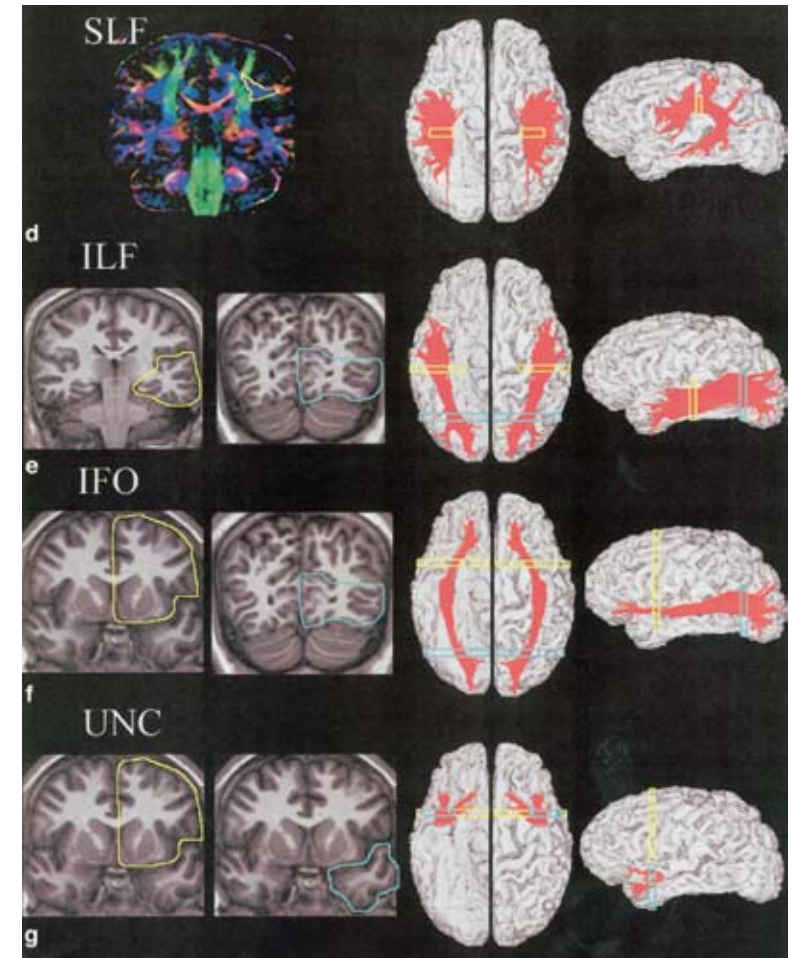
which connects the occipital lobe and thalamus (includes optic radiation), one ROI defines the occipital lobe (slice level A3) and the other the posterior part of thalamus at one slice posterior to slice level A3. d: To visualize the superior longitudinal fascicules (SLF), one reference ROI was used in slice level A3, which can be discretely identified using a DTI-based color map. e: For the inferior longitudinal fasciculus (ILF), which is known to connect the temporal lobe and occipital lobe, one ROI defines the occipital lobe (slice level A4) and the other the midtemporal lobe (slice level A3). This two-ROI combination tracks both ILF and inferior fronto-occipital fasciculi (IFO). The tracking results that fulfill criteria (ROIs) for the IFO are later removed. f: For the IFO, which is known to connect the frontal and occipital lobes, one ROI defines the frontal lobe (slice level A1) and the other the occipital lobe (slice level A4). g: To define the uncinate fascicules (UNC), which is known to connect the frontal lobe and temporal pole, two ROIs are necessary in slice level A1.

applied to all the coregistered fiber images. The T_1 volumetric image of each subject was then elastically transformed according to the method described by Davatzikos[22], and was brought into registration with the Talairach atlas. The elastic warping method is based on mapping the outer (cortical) and inner (ventricular) brain boundaries of a subject to their counterparts in the atlas, and then interpolating the transformation everywhere else by solving the elastic equations. The same elastic transformation was then applied to the coregistered fiber images, placing them into the Talairach space. We determined this transformation from the T_1 images, since the fiber images do not have the appropriate anatomical detail. Images were obtained from 10 healthy volunteers (five males and five females, 20–30 years old). Informed consent from all subjects was obtained in accordance with institutional guidelines.

Results and discussion

White Matter Tract Reconstruction and Comparison with Neuroanatomy

Existing neuroanatomical knowledge[1,2,23] of the approximate location of the association pathways was used to define reference ROIs through which the tracts must pass. The protocols we developed for reconstructing the cortical association fibers are summarized in figure 1. Because these tracts do not always have clear anatomical landmarks to discretely identify them, the success and general applicability of the approach was optimized by choosing reference ROIs that include large discernable anatomical units, such as the frontal, temporal, and occipital lobes. These anatomical landmarks and ROIs were located using T_1-weighted images, except for the superior longitudinal fasciculus (SLF) (figure 1d), which could only be defined using a color-coded map. One drawback of this anatomy-based, double-ROIs reference approach is its inability to reconstruct branching between chosen pairs of ROIs; as a consequence, it is mainly suitable for tracts that connect two distant regions and do not branch out between the
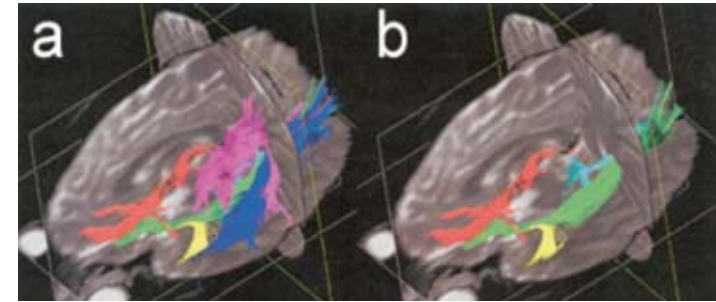
Figure 2 3D reconstruction of the major cortical association fibers. a: Six association fibers are simultaneously presented in a tri-planer view to illustrate spatial relationships between the tracts. b: SLF and ILF are removed to allow a more medial view of the tracts. Reconstructed tracts: anterior thalamic radiation (ATR, red); posterior thalamic radiation (including the optic radiation) (PTR, light blue); superior longitudinal fasciculus (SLF, pink); inferior longitudinal fasciculus (ILF, blue); inferior fronto-occipital fasciculus (IFO, green); and uncinate fasciculus (UNC, yellow).
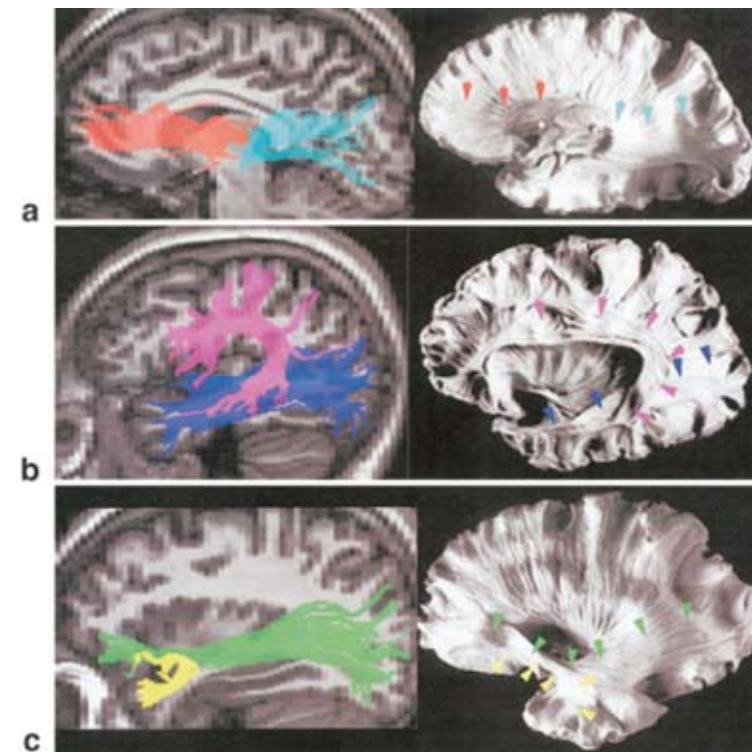
two target areas. Therefore, only one ROI was used for SLF, which is known to have extensive branching in the frontal, parietal, and temporal lobes. A 3D representation of the fibers that can be tracked is given in figure 2.

A qualitative comparison between the reconstruction results of several major fiber bundles and a "white matter" anatomical preparation in figure 3a-c shows good spatial agreement.

For more anatomical detail, slice-by-slice locations of the tracking results are shown in figure 3d. It can be seen that cores of the reconstructed tracts penetrate known anatomical landmarks. Both the reconstructed image and histological preparation shown in figure 3b reveal a comprehensive view of the superior longitudinal fasciculus (SLF (pink)), including extensive branching into the parietal lobes, C-shape projections around the Sylvian fissure, and projections into the temporal lobe. The 2D slices in figure 3d also show prominent projections to Broca's area in the frontal lobe. The inferior longitudinal fasciculus (ILF (blue)) behind the SLF can also be appreciated. Figure 3c shows that the reconstructed inferior fronto-occipital fasciculus (IFO) and uncinate fasciculus (UNC) are in agreement with the post-mortem picture. For the identification of the IFO, the two reference ROIs used included a large part of the entire frontal and occipital lobes. As can be seen in figure 1e and f, and also in figure 3d, the ILF and IFO share many picture elements (pixels) in the occipital lobe. In the mid-temporal lobe, the IFO occupies the medial part of the ILF. Because of this proximity of the two tracts, the two reference ROI sets used for the ILF lead to partial inclusion of the IFO, which could only be removed by rejecting tracking results that fulfil the criteria of the IFO. Based on neuroanatomical literature[1,23,24] we expected the identification of two major fasciculi, namely the inferior and superior fronto-occipital fasciculi (SFO), which connect the two large ROIs specified in figure 1f. However, the SFO could not be identified in any of the 10 volunteers. Thus, while some previous reports indicated that a SFO should be located at the lateral horn of the caudate nucleus, and despite the fact that a discrete tract can indeed be identified in slices in the 2D DTI color maps at the corresponding area (see figure 3d, indicated by an asterisk), the 3D connection analysis could not identify the fronto-occipital
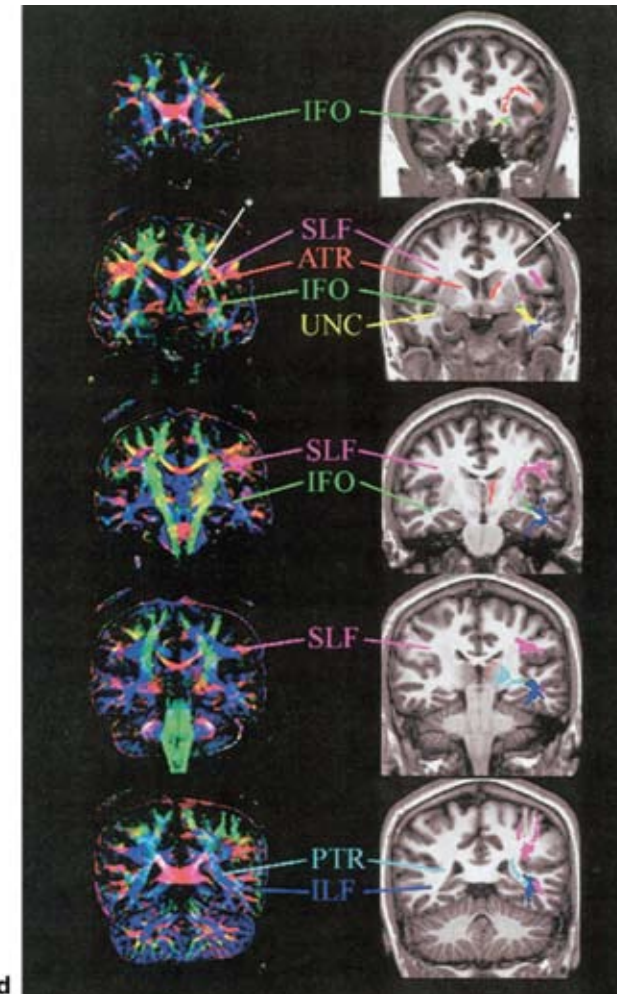
Figure 3 Qualitative neuroanatomical validation of fiber tracking using (a–c) postmortem data (35) and (d) comparison with white matter anatomical images. The anatomical preparation in a reveals the anterior and posterior thalamic radiations, and our tracking results of these tracts are superimposed on a sagittal image at the similar slice level. Similarly, b shows SLF and ILF and c shows IFO and UNC. Small arrowheads indicate approximate locations of tracts of interest in the anatomical preparations. d: DTI-based color map (left column) and results of 3D fiber tracking are shown in 2D representative slices (right column). For anatomical guidance, the tracking results are superimposed on the left cerebral hemisphere of anatomical images. In the right hemisphere, approximate locations of tracts of interest are indicated according to anatomical knowledge. Asterisks indicate the location of the superior fronto-occipital fasciculus postulated previously.

cortico-cortical connection in this region. These findings seem to support recent reports on the SFO, suggesting that it may not exist as a long-association tract.[23,25]

Reconstruction in a Common Reference Frame

An important prerequisite for the clinical application of tract-tracking is the ability to obtain anatomical maps of normal white matter fibers in a general reference frame, and to quantify their anatomical and functional properties. One approach to analyze the reliability of a tracking method, and to determine normal and pathological variations in patterns of these reconstructed axonal tracts and their association with different cortical areas, is the generation of statistical maps for each tract system. To achieve this, we standardized individual brains into the Talairach coordinate brain reference frame using elastic warping[22], and then calculated the probability of having a particular tract system delineated as explained above for each pixel for a population of 10 healthy volunteers (figure 4a). The results of this approach are shown for the SLF, ILF, and IFO in figure 4b. In these probabilistic maps, each pixel reflects the percentage of normal subjects that contained a particular tract. This point can be seen more clearly in figure 4c, in which representative 2D slices of the probabilistic map are shown. In this figure, the probability of having the SLF in a certain pixel, as based on the normative data, is presented using a color shading scale. It can be seen that the core as well as some of the branches of the SLF in the frontal, parietal, and temporal lobes are well defined, with high probability, indicating a high consistency of the tracking results in these regions among normal subjects.

Advances in warping techniques should improve the quality of the normalization process and may lead to probabilistic maps showing less variability for specific white matter tracts in normal controls.

As an example of how new insight into the neuropathology of patients with white matter diseases could be obtained using the probabilistic map approach described above, we compared
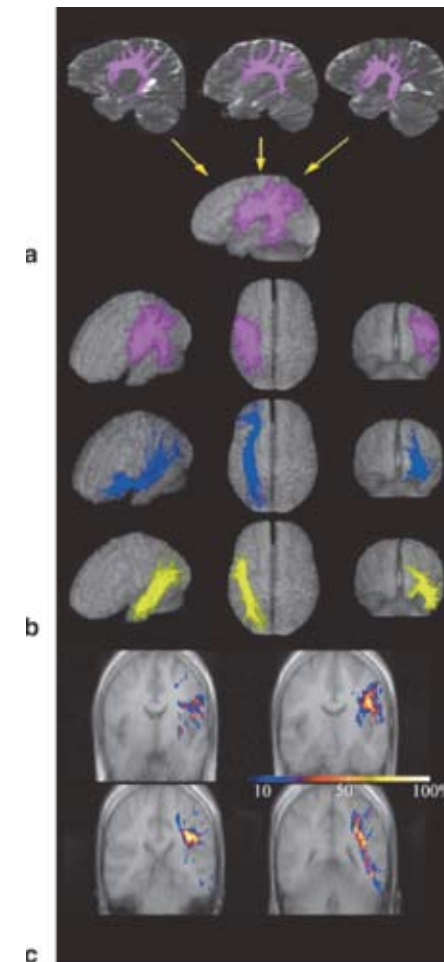
Figure 4 Probabilistic maps of the long-association fiber systems in Talairach coordinates. The 3D reconstruction results for the superior longitudinal fasciculus (SLF, pink) of 10 healthy volunteers (three representative cases are shown in a) were standardized using elastic warping [22], and probabilistic maps were created by superimposing the data onto the standard coordinate. Consequently, the intensity of each pixel contains the information on the intersubject agreement (probability) in the spatial configuration of a particular fiber bundle. Warping was also applied to the inferior fronto-occipital fasciculus (IFO, blue) and the inferior longitudinal fasciculus (ILF, yellow) as shown in b. Actual probability can be more easily appreciated in c, where representative slices of the statistical map of the SLF are shown, as obtained from 10 healthy volunteers using the same tracking criteria (ROI, anisotropy, and vector product, as indicated in fig. 1 and the Methods and Materials section). Intensity of the colored pixels represents the probability of the location of the tract (100 means 100% matching among the 10 subjects).
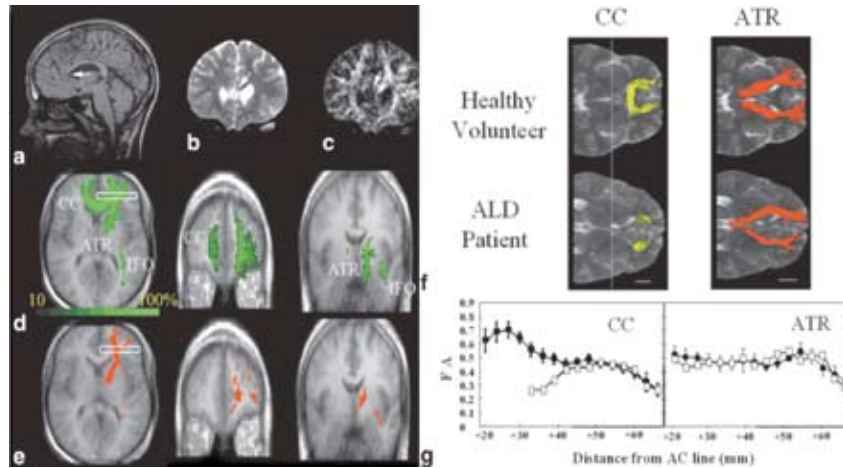
Figure 5 Example of the clinical application of fiber tracking to an x-ald patient. (a) t₁- and (b) t₂- weighted images, and (c) an FA map of an x-ald patient. The genu of the corpus callosum is severely affected in this patient (indicated by arrows). Probabilistic maps of tracts that are connected to the left frontal lobe in normal controls (N = 10) and the x-ald patient are shown in d and e, respectively. The intensity level of the green (normal) color represents the probability. White boxes indicate the location from which the reference ROI was drawn for the tracking. Abbreviations: cc = corpus callosum, ATR = anterior thalamic radiation, ILF = inferior longitudinal fasciculus. f: Comparison of tracking of the genu of the cc and the ATR in the frontal lobe of the x-ald patient and the healthy volunteers. g: FA of the reconstructed projections (circles = volunteers; squares = patient) plotted along the anterior-posterior axis as a function of its distance from the anterior commissure (AC). f: The location of the AC (dotted lines) and a scale (solid line indicating the length of 2 cm) are shown for anatomical orientations.

a control data set of 10 subjects to a patient (17- year-old male) with X-linked adrenoleukodystrophy.

This white matter disease is caused by a defect in peroxisomal degradation of very long-chain fatty acids, and is characterized neuropathologically by demyelination and variable inflammation and gliosis. Although white matter involvement in x-ald is rather diffuse, distinctive topographic patterns of demyelination are generally recognized. In this particular patient, as shown in figure 5, conventional (figures 5a and b) as well as diffusion anisotropy (figure 5c) images show that the genu of corpus callosum is severely damaged.

The results in figure 5 indicate that 3D fiber tracking can provide a new dimension into the interpretation of this neurological condition. Figure 5d shows the normal probabilistic map (10 volunteers) for all tracts that reach the left frontal lobe through the reference ROI (indicated by the white box). These normal-control results identify three major pathways into this lobe. One connects homologous regions of each hemisphere through the genu of the corpus callosum (cc), the second leads to the thalamus via the anterior thalamic radiation (ATR), and the third is the inferior frontoccipital fasciculus (IFO). The same tracking approach in the patient indicates that the frontal-frontal connections via the corpus callosum are selectively affected, while the other two pathways are relatively preserved (figure 5e). In agreement with these neuroanatomical findings, the neurological and neuropsychological examinations of this patient were indeed found to deviate from normal for tasks involving specific frontal lobe functions. The latter included deficits in semantic fluency (1.16 SD below mean for age), phonemic fluency (2.08 SD below normal), and verbal encoding strategies (3.00 SD below normal mean). Other brain functions were found to be within normal limits, as reflected by a high average full-scale IQ of 111.

Analysis of MRI Properties of Individual White Matter Tracts (Tract-Specific MRI)

Once a white matter tract of interest is reconstructed for an individual, it becomes possible to perform tract-specific studies of diffusion parameters, such as anisotropy. Other MR indices, such as relaxation times and magnetization transfer properties[26], can in principle also be obtained through coregistration with the diffusion images and superimposition of the tracking coordinates. As an example, we show an anisotropy comparison between healthy individuals and the x-ald patient for the corpus callosum and anterior thalamic radiation. In figure 5g, the anisotropy profiles for the normal group and the x-ald patient are plotted along the anterior-posterior axis, as a function of distance with respect to the anterior commissure. It can be seen that the

anisotropy of the short tracts of the patient is comparable to that of the callosal fibers in the healthy volunteers between coordinates +67 mm (near frontal pole) and +42 mm. However, the anisotropy decreases between +42 mm and +39 mm, and becomes virtually undetectable (< 0.3) near the genu (+21 to + 27 mm). No changes in anisotropy were apparent along the ATR. This result demonstrates the potential to obtain valuable information about the evolution of white matter pathology. In the case of X-ALD, the use of more sensitive and specific imaging techniques could be important for the early detection of abnormalities in at-risk populations.

Technical Limitations

Although the 3D fiber tracking technique provides us an exciting opportunity to visualize association pathways *in vivo*, its inherent limitations should also be realized. As with any other MRI technique, DTI can only provide anatomical information about the brain at a macroscopic level. Specifically, fiber orientation revealed by DTI reflects the average orientation of axonal fibers for each pixel, and is susceptible to tissue heterogeneity. Within a pixel, numerous fibers may be crossing, or there may be a small portion of fibers that have different orientations from dominant fibers[27]. Therefore, DTI fiber tracking is presently limited to visualization of *in vivo* gross anatomy of white matter tracts connecting functional brain regions. However, several new techniques to improve DTI data acquisition and tract tracking are now becoming available. These include high angular sampling of b-space[28-32], interpolation or regularization of the tensor field[14,17,18], and global energy minimization for tract tracking[33,34]. Many of these new developments are compatible with the concepts introduced in this work, including the knowledge-based multiple-ROI approach and the standardization technique for statistical analysis of tract coordinates.

Conclusions

Long-cortical-association fibers have been postulated to be critical for the functional integration of these neural networks, and may play a specific role in various cognitive and behavioral disorders such as Alzheimer's disease, conduction aphasia, dyslexia, and schizophrenia. Data were presented showing that these major cortical association fibers can be tracked noninvasively in humans using DTI, and that the tracking of the cores of these fibers is highly reproducible between individuals. This capability is potentially useful for diagnosing various white matter disorders, and improving understanding of brain function by allowing correlation of DTI findings and clinical symptoms. As a first illustration of this capability, a deficiency in the collosal fibers of a patient with X-ALD was detected which correlated with functional testing.

Future potential clinical applications include better characterization of brain malformations, identification of early changes in neurodegenerative disorders that selectively affect specific fibers, and evaluation of local and distant injury in patients with brain tumors, stroke, and trauma. The incorporation of axonal mapping into the presurgical diagnostic battery of patients with brain tumors or intractable epilepsy should also be feasible.

Acknowledgements

References

1 **Crosby E**, Humphrey T, Lauer E. Correlative anatomy of the nervous system. New York: MacMillan; 1962.

2 **Krieg W.** Connections of the cerebral cortex. Evanston, IL: Brain Books; 1963.

3 **Paus T**, Zijdenbos A, Worsley K, Collins LD, Blumenthal J, Giedd JN, Rapoport JL, Evans AC. Structural maturation of neural pathways in children and adolescents: *in vivo* study. Science 1999;283:1908–1911.

4 **Meyer JW**, Makris N, Bates JF, Caviness VS, Kennedy DN. MRI-based topographic parcellation of human cerebral white matter. Neuroimage 1999;9:1–17.

5 **Moseley ME**, Cohen Y, Kucharczyk J, Mintorovitch J, Asgari HS, Wendland MF, Tsuruda J, Norman D. Diffusion-weighted MR imaging of anisotropic water diffusion in cat central nervous system. Radiology 1990;176:439–445.

6 **Beaulieu C**, Allen PS. Determinants of anisotropic water diffusion in nerves. Magn Reson Med 1994;31:394–400.

7 **Henkelman R**, Stanisz G, Kim J, Bronskill M. Anisotropy of NMR properties of tissues. Magn Reson Med 1994;32:592–601.

8 **Basser PJ**, Mattiello J, Le Bihan D. MR diffusion tensor spectroscopy and imaging. Biophys J 1994;66:259–267.

9 **Pierpaoli C**, Jezzard P, Basser PJ, Barnett A, Di Chiro G. Diffusion tensor MR imaging of human brain. Radiology 1996;201:637–648.

10 **Makris N**, Worth AJ, Sorensen AG, Papadimitriou GM, Reese TG, Wedeen VJ, Davis TL, Stakes JW, Caviness VS, Kaplan E, Rosen BR, Pandya DN, Kennedy DN. Morphometry of *in vivo* human white matter association pathways with diffusion weighted magnetic resonance imaging. Ann Neurol 1997;42:951–962.

11 **Ulug A**, van Zijl PCM. Orientation-independent diffusion imaging without tensor diagonalization: anisotropy definitions based on physical attributes of the diffusion ellipsoid. J Magn Reson Imaging 1999;9:804–813.

12 **Mori S**, Crain BJ, Chacko VP, van Zijl PCM. Three dimensional tracking of axonal projections in the brain by magnetic resonance imaging. Ann Neurol 1999;45:265–269.

13 **Xue R**, van Zijl PCM, Crain BJ, Solaiyappan M, Mori S. *In vivo* threedimensional reconstruction of rat brain axonal projections by diffusion tensor imaging. Magn Reson Med 1999;42:1123–1127.

14 **Conturo TE**, Lori NF, Cull TS, Akbudak E, Snyder AZ, Shimony JS, McKinstry RC, Burton H, Raichle ME. Tracking neuronal fiber pathways in the living human brain. Proc Natl Acad Sci USA 1999;96:10422–10427.

15 **Mori S,** Kaufmann WK, Pearlson GD, Crain BJ, Stieltjes B, Solaiyappan M, van Zijl PCM. *In vivo* visualization of human neural pathways by MRI. Ann Neurol 2000;47:412–414.

16 **Jones DK**, Simmons A, Williams SC, Horsfield MA. Non-invasive assessment of axonal fiber connectivity in the human brain via diffusion tensor MRI. Magn Reson Med 1999;42:37–41.

17 **Poupon C**, Clark CA, Frouin V, Regis J, Bloch L, Le Bihan D, Mangin JF. Regularization of diffusion-based direction maps for the tracking of brain white matter fascicules. NeuroImage 2000;12:184–195.

18 **Basser PJ**, Pajevic S, Pierpaoli C, Duda J, Aldroubi A. In vitro fiber tractography using DT-MRI data. Magn Reson Med 2000;44:625–632.

19 **Stieltjes B**, Kaufmann WE, van Zijl PCM, Fredericksen K, Pearlson GD, Mori S. Diffusion tensor imaging and axonal tracking in the human brainstem. Neuroimage 2001;14:723–735.

20 **Mulkern RV**, Gudbjartsson H, Westin CF, Zengingonul HP, Gartner W, Guttmann CR, Robertson RL, Kyriakos W, Schwartz R, Holtzman D, Jolesz FA, Maier SE. Multi-component apparent diffusion coefficients in human brain. NMR Biomed 1999;12:51–62.

21 **Pierpaoli C**, Basser PJ. Toward a quantitative assessment of diffusion anisotropy. Magn Reson Med 1996;36:893–906.

22 **Davatzikos C.** Mapping of image data to stereotaxic spaces: applications to brain mapping. Hum Brain Mapp 1998;6:334–338.

23 **Mettler F.** Neuroanatomy. St. Louis, MO: C.V. Mosby Co.; 1948.

24 **Tusa R**, Ungerleider L. The inferior longitudinal fasciculus: a reexamination in humans and monkeys. Ann Neurol 1985;18:583–591.

25 **Ture U**, Yasargil M, Pait T. Is there a superior occipitofrontal fasciculus? A microsurgical anatomic study. Neurosurgery 1997;40:1226–1232.

26 **Henkelman R**, Huang X, Xiang Q-S, Stanisz GJ, Swanson SD, Bronskill MJ. Quantitative interpretation of magnetization transfer. Magn Reson Med 1993;29:759–766.

27 **Wiegell M**, Larsson H, Wedeen V. Fiber crossing in human brain depicted with diffusion tensor MR imaging. Radiology 2000;217:897–903.

28 **Jones DK**, Horsfield MA, Simmons A. Optimal strategies for measuring diffusion in anisotropic systems by magnetic resonance imaging. MagnReson Med 1999;42:515–525.

29 **Skare S**, Hedehus M, Moseley ME, Li TQ. Condition number as a measure of noise performance of diffusion tensor data acquisition schemes with MRI. J Magn Reson 2000;147:340–352.

30 **Wedeen V**, Reese TG, Tuch DS, Weigel MR, Dou JG, Weiskoff RM, Chessler D.

Mapping fiber orientation spectra in cerebral white matter with Fourier-transform diffusion MRI. In: Proceedings of the 8th Annual Meeting of ISMRM, Denver, 2000. p 82.

31 **Elshafiey I**, Narayana PA. Exploration of b-space for diffusion tensor imaging of human brain. In: Proceedings of the 9th Annual Meeting of ISMRM, Glasgow, Scotland, 2001. p 1537.

32 **Lazar M**, Alexander AL. Error analysis of white matter tracking algorithms (streamlines and tensorlines) for DT-MRI. In: Proceedings of the 9th Annual Meeting of ISMRM, Glasgow, Scotland, 2001. p 506.

33 **Tuch DS**, Belliveau JW, Wedeen V. A path integral approach to white matter tractography. In: Proceedings of the 8th Annual Meeting of ISMRM, Denver, 2000. p 791.

34 **Parker GJ.** Tracing fiber tracts using fast marching. In: Proceedings of the 8th Annual Meeting of ISMRM, Denver, 2000. p 85.

35 **Williams TH**, Gluhbegovic N, Jew JY. The human brain: dissections of the real brain. Virtual Hospital, University of Iowa, 1997. http://www.vh.org/Providers/Textbooks/BrainAnatomy, and http://www.brain-university.com.

60

— 4 —
Brain white matter anatomy of tumor patients evaluated with diffusion tensor imaging

S. Mori, K. Fredericksen, P.C.M. van Zijl, B. Stieltjes, M.A. Kraut, M. Solaiyappan, M.G. Pomper

We applied multislice, whole-brain diffusion tensor imaging DTI to two patients with anaplastic astrocytoma. Data were analyzed using DTI-based, color-coded images and a 3-D tract reconstruction technique for the study of altered white matter anatomy. Each tumor was near two major white matter tracts, namely, the superior longitudinal fasciculus and the corona radiata. Those tracts were identified using the color-coded maps, and spatial relationships with the tumors were characterized. In one patient the tumor displaced adjacent white matter tracts, whereas in the other it infiltrated the superior longitudinal fasciclus without displacement of white matter. DTI provides new information regarding the detailed relationship between tumor growth and nearby white matter tracts, which may be useful for preoperative planning.

Introduction

Approximately 18,000 brain tumors are diagnosed annually in the United States.[1] Advancing faster than effective new brain tumor therapies are new magnetic resonance–based techniques for characterizing these malignancies. A significant problem in brain tumor imaging and therapy is the accurate depiction of white matter involvement. Are there effects of tumor on white matter pathways that are not seen on conventional T_2-weighted images? That question has important implications for the accurate localization of radiation ports and for determining whether and how extensive surgery should proceed. Diffusion tensor imaging (DTI) is a technique that can characterize the properties of water diffusion in the brain by providing three types of information, namely, the extent (apparent diffusion constant, or ADC) and directionality (anisotropy) of diffusion and its predominant orientation.[2] The ADC and anisotropy are believed to be related predominantly to the integrity of axonal tracts[3,4] and depict contrast that is different from conventional T_1- and T_2-weighted images. Abnormalities on diffusion-weighted images due to brain tumors have been reported,[5] including an increase in ADC within malignant tissue,[6-11] detection of changes in white matter fiber angles,[12] and ADC and anisotropy changes seen with therapy.[12,13] In contrast to the aforementioned studies, in which DTI provided a method of characterizing the tumor itself, we focused on the capability of DTI to reveal the effect of tumor on white matter pathways. We found that DTI is an effective tool for delineating the effect of tumor on nearby white matter tracts, information that may facilitate preoperative planning.

Patients and Methods

MRI Data Acquisition

Studies were performed using a 1.5T Philips GyroscanNT (Best, The Netherlands) system. DTI was accomplished using multislice, segmented echo-planar imaging (EPI) with cardiac triggering (repetition time [TR] = 5 heartbeats; echo time [TE] = 92ms) and

63

navigator echo phase correction. A data matrix of 128 x 95 over a field of view of 230 x 173 mm was obtained, acquiring 17 echoes per excitation. Slice thickness was 3 mm (coronal, 40–60 slices) without gaps. Diffusion weighting was performed along 6 axes, using a b-value of 600 s/mm^2. A reference image with low diffusion weighting (b= 33 s/mm^2) was recorded. Measurements were repeated 6 times to increase signal/noise. Double-echo T_2- weighted imaging (TES of 22 and 100ms; image resolution equal to DTI) was performed for anatomic guidance. Total examination time was 1 hour. Diffusion tensors at each pixel were calculated using multivariatelinear least square fitting[2] and diagonalized. The eigenvector (V1) associated with the largest eigenvalue (λ1) was assumed to represent the local fiber direction. Anisotropy maps were obtained using the orientation-independent fractional anisotropy (FA).[14] DTI-based color maps were created from FA values (image intensity) and the three vector elements of v1;[15,16] red indicated fibers running along the right to left direction, green represented anterior to posterior, and blue was superior to inferior. The average diffusion constant, ADCav, was calculated from the trace of the diffusion tensor. Axial and sagittal images were obtained by reslicing the 3-D volume data. For 3-D reconstruction of tracts of interest, the Fiber Assignment by Continuous Tracking method was employed.[17–19] Tract reconstruction required 20 minutes using an 833MHz Pentium III Workstation (Dell, Austin, TX).

Patients

Patient 1 was a male age 36 years with a right frontal anaplastic astrocytoma. Originally he presented with two partial seizures in 1 week due to a left-sided, low-grade glioma that eventually dedifferentiated to an anaplastic astrocytoma, necessitating resection. Contralateral extension of the left frontal mass was found in follow-up imaging. Patient 2 was a male age 45 years with a posterior left frontal anaplastic astrocytoma. He presented with aphasia, hemiparesis, and simple partial seizures involving the right face. DTI data on healthy volunteers were obtained from our normative DTI database (19 subjects, ages 19–43 years; 10 male).
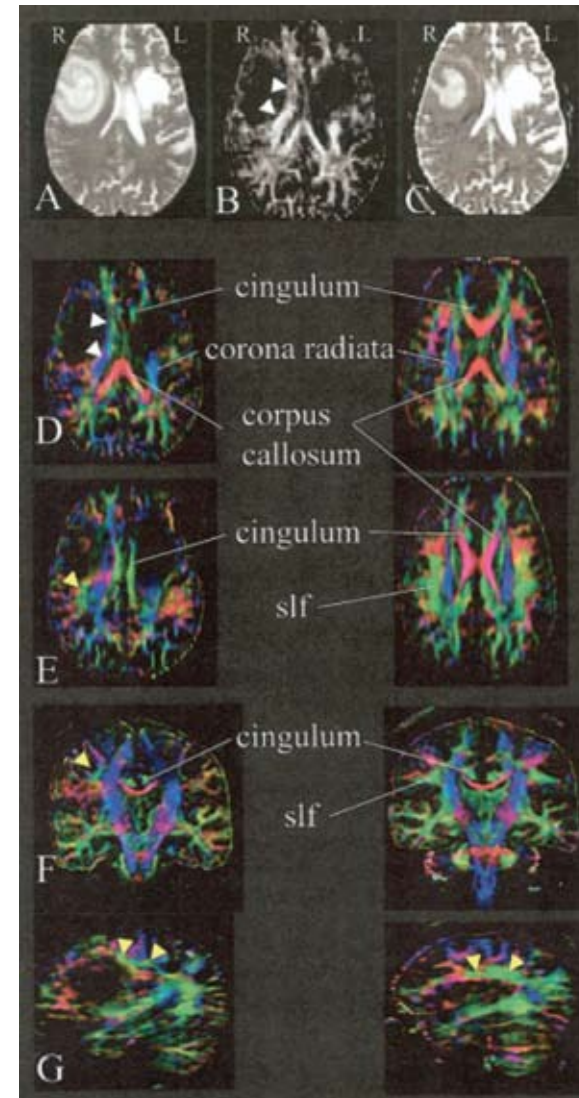
Figure 1 T_2-weighted images (A), fractional an isotropy map(B), and average diffusion constant map (C) of Patient 1. Images in (D-E) show detailed anatomical information with DTI-based color maps at two different axial slices (D and E), a coronal plane (F), and a sagittal plane (G). The color maps in the left column are from Patient 1 and the right column from a healthy volunteer (a male age 20 years) to serve as an anatomical guide. On the color maps, red indicates fibers running along the right to left orientation, green indicates anterior to posterior, and blue indicates inferior to superior. White arrowheads indicate deformed corona radiata and yellow arrowheads the superior longitudinal fasciculus (slf).

Results

Figures 1a-c show the T_2-weighted image, FA map, and ADCav map for Patient 1. The T_2-bright lesion in the left hemisphere was due to a surgical cavity. High ADCav values (see figure 1c) were found within the tumor, in keeping with previous reports.[6–11,13] The T_2-abnormal portion of the tumor (see figure 1a) had low FA (0.05 to 0.15; see figure 1b). The boundary of the tumor identified in the FA maps was not as clear as that on the T_2-weighted images, because the anisotropy of the tumor was similar to that of gray matter. To clarify white matter anatomy, the DTI-based color map was compared with that of a healthy volunteer (figures 1d-g). When the 2 subjects were compared, several major anatomical changes become evident. First, the corona radiata of the right hemisphere of the patient was dislocated medially (white arrowheads). Second, the corpus callosum genu was severely affected in the patient. This was in contrast to the cingulum, which was adjacent to the corpus callosum but structurally preserved. The superior longitudinal fasciculus (slf) is a prominent white matter tract that projects through regions occupied by the tumor. In figure 1e, only the posterior slf can be appreciated (yellow arrowheads) in the patient brain. Figures 1f and G depict the right slf of the patient dislocated superiorly as it courses anteriorly. Figure 2 shows color maps (figures 2a-d) and T_2-weighted images (figure 2e) of Patient 2. Tumor could identified by T_2 hyperintensity and low anisotropy. Although this tumor displayed similar histology to that of Patient 1, the color maps indicate that the low anisotropy regions were not accompanied by deformation of adjacent white matter structures. As with Patient 1, the slf of Patient 2 lay within the path of the tumor. The slf can be appreciated in the contralateral hemisphere (yellow arrowheads) but not near the tumor. The slf was apparently within the area of lowest anisotropy. To confirm that, we reconstructed the trajectory of the slf in the contralateral hemisphere. For the reconstruction, the slf was identified at the slice level shown in figure 2c, and tracking results that penetrated the identified slf were searched. The result is shown in figure 2e (red), superimposed on T_2-weighted images. The T_2- hyperintense regions correlated spatially with the brain regions occupied by the slf.
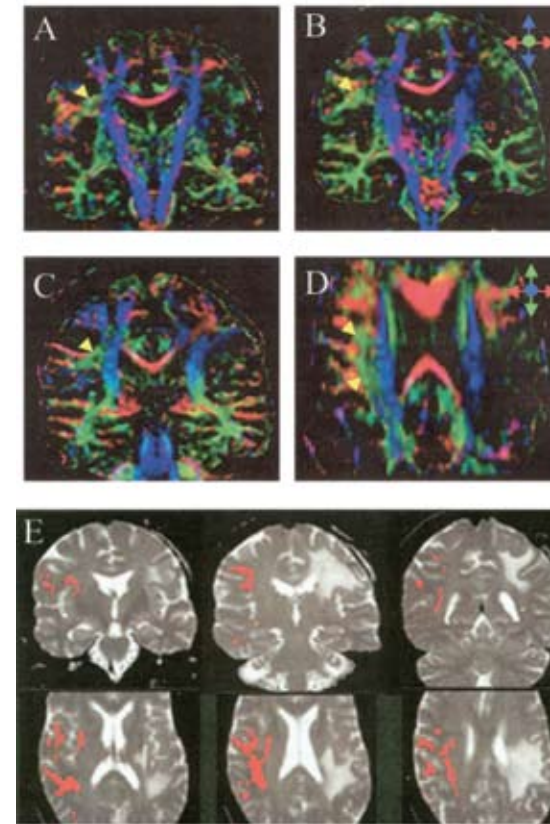
Figure 2 Color maps at three coronal levels (A-C) and a axial level (D) of Patient 2. In all color maps, blue represents fibers running in a superior to inferior direction, red left to right, and green anterior to posterior. Arrowheads indicate locations of the superior longitudinal fasciculus (slf). In (E), coordinates of the slf in the contralateral hemisphere determined from the 3-D reconstruction technique Fiber Assignment by Continuous Tracking are superimposed on T_2-weighted images.

A 3-D reconstruction of the corona radiata was performed for both patients and is shown in figure 3. The 3-D relationship of the corona radiata with the tumor can be clearly appreciated. The corona radiata of Patient 1 surrounds the surface of the tumor because of mechanical compression. On the other hand, the tumor in Patient 2 did not change the trajectory of the corona radiata, and it projected into the core of the T_2-hyperintense regions, where the tracking terminated due to the low anisotropy.
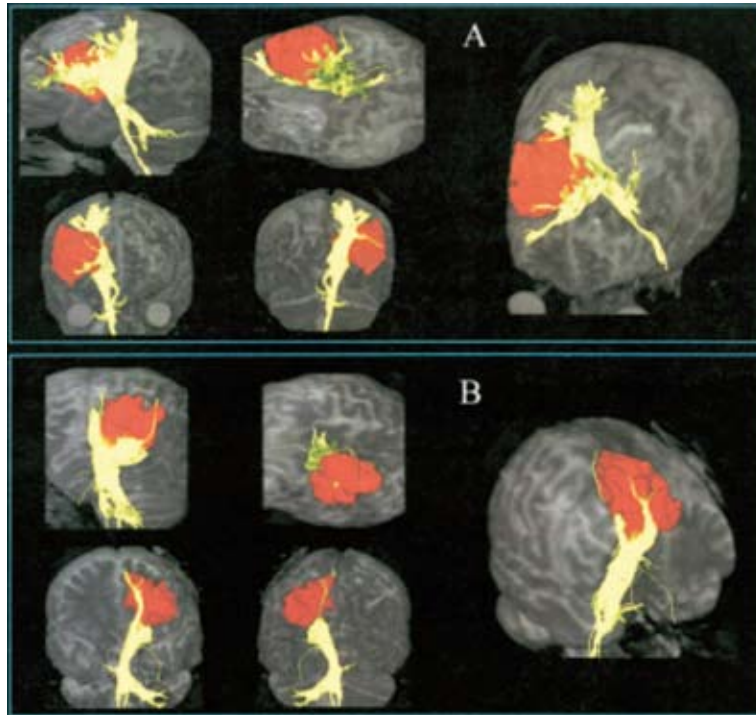
Figure 3 A 3-D tract reconstruction of the corona radiata in Patients 1 (A) and 2 (B). The corona radiata (yellow) was reconstructed using the FACT method. Regions of interest for the tracking were identified at the posterior limb of the internal capsule. For clarity, only a part of the corona radiata that was adjacent to the tumors (red) is shown.

Discussion

We report the application of 3-D DTI-based white matter anatomic studies for 2 patients with brain tumors. We found that FA alone might not provide contrast superior to that of conventional T_2-weighted images to define tumors. However, the DTI-based color-coded maps could provide unique information about white matter architecture and its alteration due to the tumors. This finding is in line with previous reports on altered fiber angles due to tumor mass.[12] In this study, we also employed 3-D tract reconstruction techniques, which greatly aided the slice-by-slice interpretation of the color maps, especially in cases of deformed anatomy.

Both patients had anaplastic astrocytomas. However, the effects of their tumors on the 3-D white matter disposition were different. In Patient 1, the tumor grew discretely, compressing the corona radiata and slf, which were dislocated medially and superiorly, respectively (see figure 1). The corpus callosum genu was severely affected, likely due to Wallerian degeneration after surgery in the left hemisphere. Although the T_2-weighted image of Patient 1 (see figure 1a) also showed that the tumor compressed adjacent white matter, information regarding the specific white matter tracts dislocated, and in which directions, could be obtained only by 3-D DTI. Unlike the tumor of Patient 1, the tumor of Patient 2 did not induce significant anatomic deformation. That difference is best illustrated by examining the corona radiata (see figures 2 and 3). Patient 2 (see figure 2) illustrates the fact that significant decreases in anisotropy may be evident even without marked anatomic deformity. Figure 2e shows that the high T_2 signal and low FA regions spread and follow regions occupied by the slf, consistent with the proposed theory that tumors might spread along white matter tracts.[20] However, we could not conclude whether the T_2 hyperintensity along the slf indicates infiltrating tumor or Wallerian degeneration. Comprehensive, longitudinal studies with histological correlation are needed. While 3-D tract reconstruction provides a new way to evaluate white matter architecture, its limitations should also be recognized. DTI is of limited resolution (2 x 2 x 3 mm interpolated to 1 x 1 x 3 mm in the presented work), leading to substantial partial volume effects, including multiple populations of fibers with different orientations within a pixel. Consequently, it cannot provide information about connectivity of the brain at the cellular level. The reconstructed tract trajectories reflect only the macroscopic configuration of prominent fiber bundles. Another problem is the motion susceptibility of the high-resolution segmented EPI approach, which presently limits its utility for pediatric or uncooperative patients.

In conclusion, we have demonstrated the application of 3-D DTI to the study of white matter trajectory using data from patients with anaplastic astrocytomas. The DTI-based color maps and 3-D tract reconstructions provided detailed anatomic information on

relationships between tumors and nearby white matter tracts, which may be important in therapeutic planning.

Acknowledgements

70

References

1 **Huncharek M,** Muscat J. Treatment of recurrent high grade astrocytoma; results of a systematic review of 1,415 patients. Anticancer Res 1998;18:1303–1311.

2 **Basser PJ,** Mattiello J, LeBihan D. Estimation of the effective self-diffusion tensor from the NMR spin echo. J Magn Reson B 1994;103:247–254.

3 **Beaulieu C,** Allen PS. Determinants of anisotropic water diffusion in nerves. Magn Reson Med 1994;31:394–400.

4 **Henkelman R,** Stanisz G, Kim J, Bronskill M. Anisotropy of NMR properties of tissues. Magn Reson Med 1994;32: 592–601.

5 **Le Bihan D,** Douek P, Argyropoulou M, et al. Diffusion and perfusion magnetic resonance imaging in brain tumors. Top Magn Reson Imaging 1993;5:25–31.

6 **Tien RD,** Felsberg GJ, Friedman H, et al. MR imaging of high-grade cerebral gliomas: value of diffusion-weighted echoplanar pulse sequences. AJR Am J Roentgenol 1994;162: 671–677.

7 **Els T,** Eis M, Hoehn-Berlage M, Hossmann KA. Diffusionweighted MR imaging of experimental brain tumors in rats. Magma 1995;3:13–20.

8 **Brunberg JA,** Chenevert TL, McKeever PE, et al. *In vivo* MR determination of water diffusion coefficients and diffusion anisotropy: correlation with structural alteration in gliomas of the cerebral hemispheres. AJNR Am J Neuroradiol 1995;16: 361–371.

9 **Desprechins B,** Stadnik T, Koerts G, et al. Use of diffusion weighted MR imaging in differential diagnosis between intracerebral necrotic tumors and cerebral abscesses. AJNR Am J Neuroradiol 1999;20:1252–1257.

10 **Sugahara T,** Korogi Y, Kochi M, et al. Usefulness of diffusion weighted MRI with echoplanar technique in the evaluation of cellularity in gliomas. J Magn Reson Imaging 1999;9:53–60.

11 **Kim YJ,** Chang KH, Song IC, et al. Brain abscess and necrotic or cystic brain tumor: discrimination with signal intensity on diffusion-weighted MR imaging. AJR Am J Roentgenol 1998; 171:1487–1490.

12 **Wieshmann UC,** Symms MR, Parker GJ, et al. Diffusion tensor imaging demonstrates deviation of fibres in normal appearing white matter adjacent to a brain tumour. J Neurol Neurosurg Psychiatry 2000;68:501–503.

13 **Chenevert TL,** Stegman LD, Taylor JM, et al. Diffusion magnetic resonance imaging: an early surrogate marker of therapeutic efficacy in brain tumors. J Natl Cancer Inst 2000;92: 2029–2036.

14 **Pierpaoli C,** Basser PJ. Toward a quantitative assessment of diffusion anisotropy. Magn Reson Med 1996;36:893–906.

71

15 **Makris N,** Worth AJ, Sorensen AG, et al. Morphometry of *in vivo* human white matter association pathways with diffusion weighted magnetic resonance imaging. Ann Neurol 1997;42: 951–962.

16 **Pajevic S,** Pierpaoli C. Color schemes to represent the orientation of anisotropic tissues from diffusion tensor data: application to white matter fiber tract mapping in the human brain. Magn Reson Med 1999;42:526–540.

17 **Mori S,** Crain BJ, Chacko VP, van Zijl PCM. Three dimensional tracking of axonal projections in the brain by magnetic resonance imaging. Ann Neurol 1999;45:265–269.

18 **Xue R,** van Zijl PCM, Crain BJ, et al. *In vivo* threedimensional reconstruction of rat brain axonal projections by diffusion tensor imaging. Magn Reson Med 1999;42: 1123–1127.

19 **Stieltjes B,** Kaufmann WE, van Zijl PCM, et al. Diffusion tensor imaging and axonal tracking in the human brainstem. NeuroImage 2001;14:723–735.

20 **Geer CP,** Grossman SA. Interstitial fluid flow along white matter tracts: a potentially important mechanism for the dissemination of primary brain tumors. J Neurooncol 1997;32:193–201.

72

— 5 —

Detection of tumour infiltration in axonal fibre bundles using diffusion tensor imaging

M. Schlüter, B. Stieltjes, H.K. Hahn, J. Rexilius, O. Konrad-Verse, H.O. Peitgen

We present a method for the revelation and quantification of white matter infiltration from human brain tumors based on Diffusion Tensor Imaging (DTI). Since white matter destruction alters the local diffusion properties, DTI has the potential to sensitively detect tumor infiltration and to quantify the degree thereof. Here, we consider three tumor patients with gliomas, two with and one without contralateral tumor progress. We use DTI to identify specific fiber systems, where infiltration has to be assessed. On this basis, the problem of arbitrary region of interest definition is solved such that tumor infiltration can be reliably quantified in particular fiber bundles. It is demonstrated at the Corpus Callosum (CC) and the Pyramidal Tract (PT) that fiber bundle infiltration can be well detected by specific visualization techniques of diffusion tensor data. Infiltration of the CC is quantified by using a reliable method for the determination of diffusion properties inside particular fiber bundles. For an age normalized quantification of white matter infiltration we introduce the Integrity Index, which measures the diffusion anisotropy inside an infiltrated fiber bundle normalized by the diffusion anisotropy in a specific region of healthy fiber tissue. It turns out that the quantification of CC infiltration correlates with contralateral tumor progress and has the potential to serve as a surrogate marker for this process, which is crucial for surgical therapy decisions and intervention planning.

Tumor cells from infiltrating tumors like gliomas mainly invade along white matter tracts[1]. This infiltration process makes it difficult to distinguish gliomas from healthy tissue. Furthermore, glioma cells spread beyond the areas detected as tumorous in anatomical MRI modalities[2]. Due to this diffuse infiltration, these tumors have a poor prognosis and the detection and reliable quantification of white matter tumor infiltration is still a challenging problem.

Since the process of tumor infiltration destroys white matter tissue, the properties of water diffusion should have been changed in affected white matter tracts. Free water of temperature 37°C (98.6°F) has an Apparent Diffusion Coefficient (ADC) of about $3*10^3$ mm²/sec. Variations of the ADC resulting from temperature variations in the human brain are small in comparison to ADC variations resulting from tissue structure. On this basis, ADC maps of the brain can be obtained by Diffusion Weighted Imaging (DWI) - a special modality of Magnetic Resonance Imaging (MRI). However, white matter tissue is highly structured and water diffusion is anisotropic in white matter tracts. Thus, water diffusion in white matter tissue is described not only by the ADC but also by the amount and orientation of diffusion anisotropy and has to be described more generally by a Diffusion Tensor (DT). Consequently, the DT can be determined by Diffusion Tensor Imaging[3,4] (DTI) - a generalization of DWI. Since the DT carries local information about the orientation of fiber bundles, processing of the DT data allows for the extraction of fiber tract directions and the visualization of fiber bundles[5,6,7,8,9]. Furthermore, diffusion properties such as the Fractional Anisotropy (FA) and the ADC are indicators for the integrity of white matter tissue and the change of white matter integrity resulting from tumor infiltration is expected to be detected and assessed more sensitive in DTI data than in anatomcal MRI data[10,11,12,13].

However, all approaches to detect infiltration from DTI known to the authors are based on the measurement of some diffusion anisotropy like the FA or the ADC inside an arbitrary user defined region of interest (ROI) in the periphery of the tumor.

The arbitrary region of interest definition makes reproducible quantification and inter-subject comparison of white matter infiltration difficult. As a consequence, recent work states that a reliable differentiation between infiltration and vasogenic edema is not yet possible on the basis of DTI[13], which is in contradiction to previous work[10, 11, 12].

Here, we visualize the DT field by ellipsoids[8] and a recently introduced color coding of the main diffusion orientation (MDO)[9]. This additional information allows for the identification of particular fiber bundles leading to the periphery of the tumor. Inside those fiber bundles infiltration can be assessed more reliably and sensitively. This is demonstrated at the Corpus Callosum (CC) and the Pyramidal Tract (PT) of patients with and without contralateral progress of gliomas. Simultaneous visualization of an infiltrated CC and the above Cingulum (CG), which is oriented perpendicular to the CC, demonstrates that the FA is strongly reduced inside the CC, while it remains unchanged inside the CG, supporting histological observations that gliomas mainly infiltrate along fibers but not in perpendicular directions[1, 2].

Infiltration of the CC is quantified by using a probabilistic mixture model for diffusion properties inside the fiber bundle and surrounding background tissue[9]. Thus, the problem of the definition of an arbitrary user defined ROI can be solved and reproducible quantification and intra-subject comparison of white matter infiltration becomes possible. For an age normalized quantification of infiltration we introduce the Integrity Index, which measures the diffusion anisotropy inside an infiltrated fiber bundle normalized by the diffusion anisotropy in a specific region of healthy fiber tissue. It turns out that the Integrity Index of the CC for the patients with contralateral tumor progress is significantly lower than for the patients without contralateral tumor progress. Thus, the method has the potential to serve as a surrogate marker for CC infiltration, which helps to improve surgical therapy decisions and to minimize interventional risk.

Material

Three tumor patients with a right hemispheric glioma are considered. Two (F, 65 y, F 81 y) with and one (M, 47 y) without contralateral tumor progress. A healthy volunteer (M, 29 y) serves as a reference. For the tumor patients 10 DTI (6 gradient directions each) datasets are acquired on a 1.5T Magneton SymphonyVision (Siemens Medical Solutions). For the healthy volunteer 10 DTI datasets (12 gradient directions each) are acquired on a 3T Allegra (Siemens Medical Solutions). The 10 independent DTI datasets are resampled, spatially matched, and averaged in order to increase the signal-to-noise ratio as compared to a single dataset. The DT is reconstructed by standard least square methods. In addition to the DTI data, T_2 weighted MRI data is acquired for the 81 y female and FLAIR- MRI data is acquired for the 65 y female and the 47 y male, respectively. Data processing and visualization is performed on the basis of the research and development platform MeVisLab[14].

Results

Revelation of white matter infiltration

For the visualization of the MDO we use a unique planar color coding[9] defined with respect to an arbitrary projection plane in the following way: The orientation and the length of the projection of the MDO onto the projection plane defines the hue and the saturation of the color code, respectively, and the FA or some other diffusion anisotropy measure defines the lightness of the color code. This color coding leads to a better anatomical differentiation of neighboring fiber bundles than the conventional absolute color coding[9]. Throughout the paper, we use the sagittal projection plane for the unique planar color coding.

The complete DT is visualized as an ellipsoid, which is defined by the normalized eigenvectors of the DT scaled by the corresponding eigenvalues. The ellipsoids are colored by the unique planar color coding described above. In order to enhance anisotropic fiber bundles, the size of the ellipsoids is scaled by the
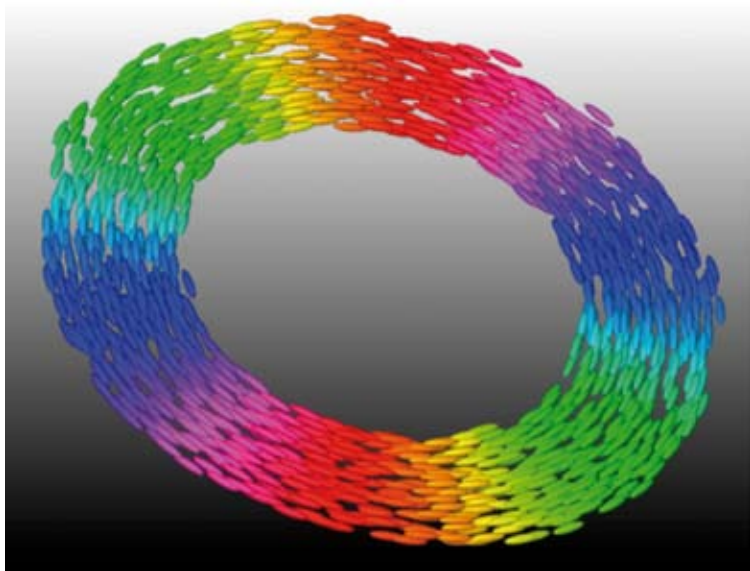
Figure 1 Illustration of the visualization of DT data. The synthetic diffusion tensors are orientated along a torus and are visualized as ellipsoids. The orientation of the main axis of the DT is colored according to the plane unique color coding.

FA. Furthermore, the position of the ellipsoids is jittered randomly, which removes lattice artifacts and helps the observer to identify coherent fiber bundles. For illustration purposes, figure 1 shows synthetic diffusion tensors orientated along a torus.

Figure 2 gives an overview of the anatomical data for the (M, 47 y) patient without (left) and the (F, 81 y) patient with (right) contralateral tumor progress, respectively. While the gliomas can be well recognized as hyperintense areas (arrows), it is difficult to identify particular potentially infiltrated fiber bundles. In figure 3, the color maps resulting from the color coding of the MDO are added to the anatomical data. Now, in the sagittal view the CC with left-right fiber orientations (unsaturated color) can be well differentiated from the above CG with posterior-anterior fiber orientations (saturated color). In the coronal view, the PT with roughly top-bottom fiber orientations (saturated green and blue color) can be well differentiated from the fiber systems in the temporal lobes with posterior-anterior fiber orientations
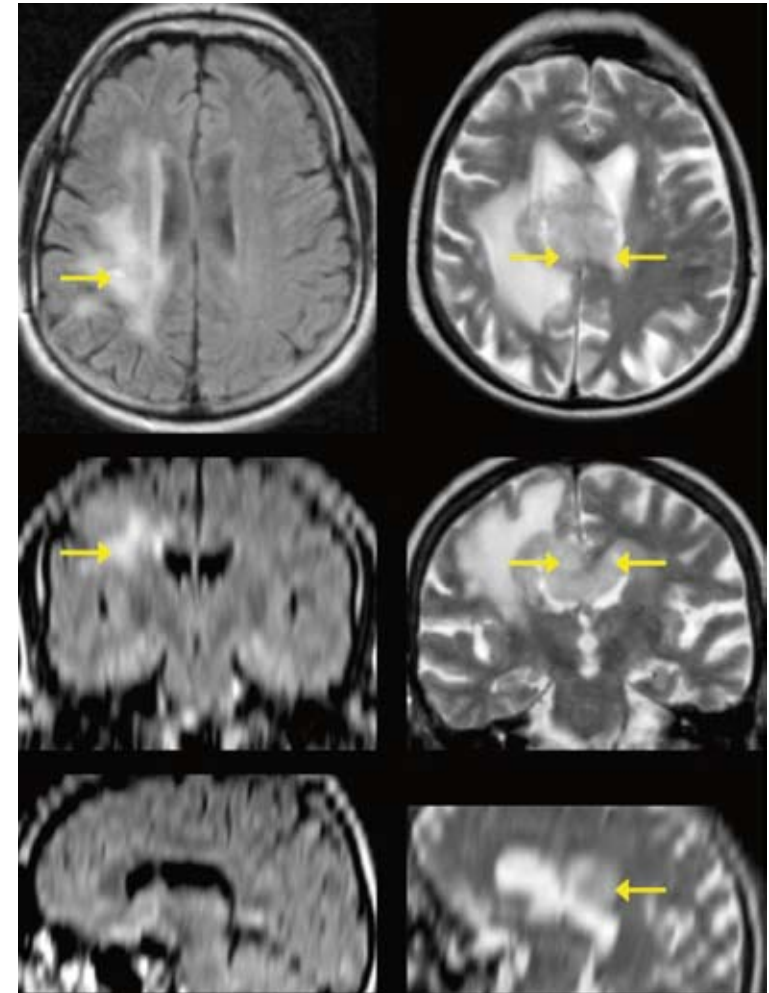
Figure 2 Axial, coronal and sagittal view of the anatomical MRI data. Left: FLAIR data for the (M, 47 y) patient without contralateral tumor progress. Right: T$_2$ weighted data for the (F, 81 y) patient with contralateral tumor progress. Gliomas can be recognized as hyperintense areas (arrows).

(saturated red color). In the sagittal view, for the patient with contralateral tumor progress, the partially reduced FA in the CC (arrows) indicates infiltration, while for the patient without contralateral tumor progress no significantly reduced FA can
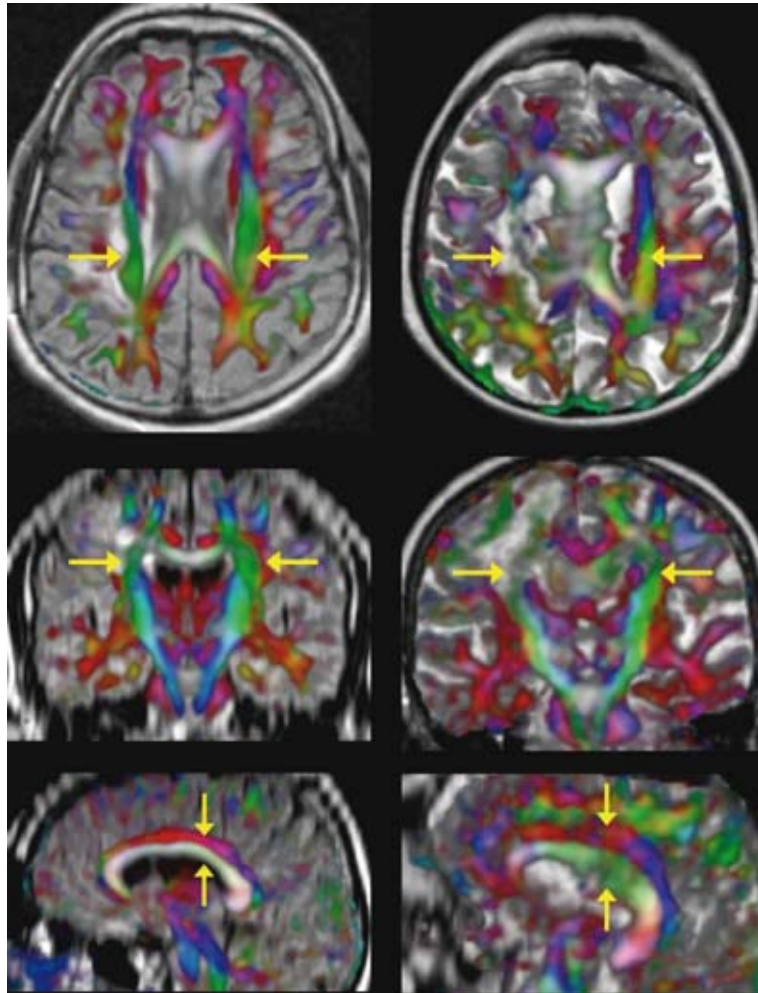
Figure 3 Axial, coronal and sagittal view of the anatomical MRI data with added DTI based color maps. Left: The (M, 47 y) patient without contralateral tumor progress. Right: The (F, 81 y) patient with contralateral tumor progress. In the sagittal view, for the patient with contralateral tumor progress, the partially reduced FA in the CC (arrows) indicates infiltration, while for the patient without contralateral tumor progress no significantly reduced FA can be observed (arrows). The FA inside the CG located directly above the CC is not significantly reduced for both patients (arrows). In the coronal and axial view, infiltration of the right PT can be observed for both patients by a, related to the left PT, reduced FA at the internal capsule (arrows).

be observed (arrows). Remarkably, the FA inside the CG located directly above the CC is not significantly reduced for both patients (arrows), supporting histological observations that gliomas preferably infiltrated along fibers but not in perpendicular directions[1,2]. In the coronal and axial view, infiltration of the right PT can be revealed by a, related to the left PT, reduced FA at the internal capsule (arrows). The DTI data suggests that infiltration of the right PT is more advanced for the patient with than for the patient without contralateral tumor progress.

In figure 4, the CC and the CG are visualized by diffusion ellipsoids. For the patient with contralateral tumor progress (bottom), the diffusion ellipsoids in the center of the CC are significantly smaller and more isotropic than in the anterior and posterior part of the CC (arrows). For the patient without contralateral tumor progress (top), no significant change of the diffusion ellipsoids can be observed. As observed in figure 3, the shape of the ellipsoids does not change significantly along the CG for both patients (arrows). In figure 5 the left and right pyramidal tracts at the internal capsule are visualized by diffusion ellipsoids. As in figure 3, infiltration of the right PT in both patients is indicated by smaller and more isotropic ellipsoids compared to the left PT.

Quantification of white matter infiltration

Potential tumor infiltration is quantified by the FA along cross sections of particular fiber bundles. In order to get robust and reproducible quantification results, we use a probabilistic mixture model for the three eigenvalues of the DT inside the fiber bundle and surrounding background tissue. Furthermore, an explicit model for partial volume effects is used, based on a uniformly distributed mixture of the two pure tissue classes.

The classification into fiber, background and mixture tissue is performed automatically by a maximum likelihood mixture model clustering algorithm[9]. Thus, the problem of the definition of an arbitrary user defined ROI can be solved and reproducible quantification and intra-subject comparison of white matter infiltration becomes possible.
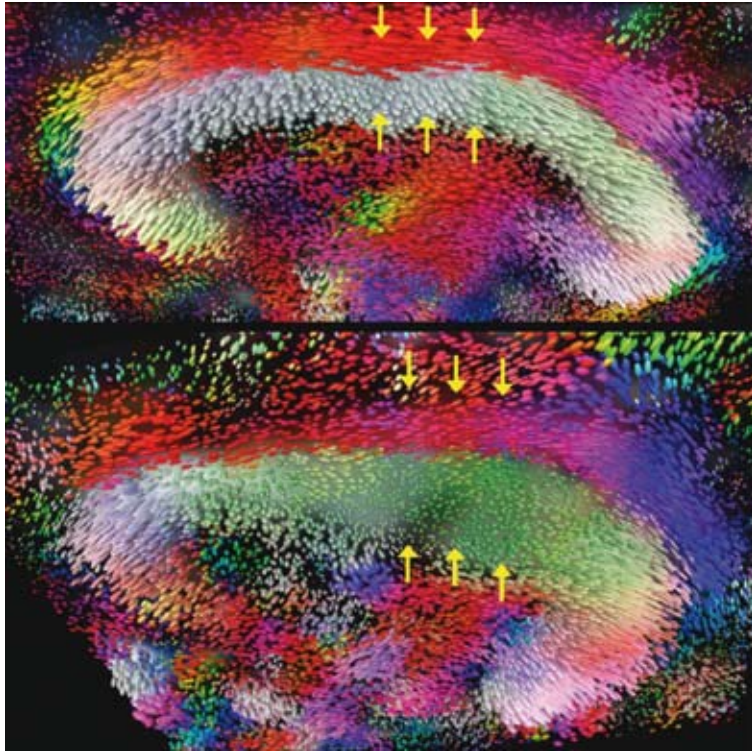
Figure 4 Diffusion ellipsoids for the CC and the CG. For the patient with contralateral tumor progress (bottom), the diffusion ellipsoids in the center of the CC are significantly smaller and more isotropic than in the anterior and posterior part of the CC (arrows). For the patient without contralateral tumor progress (top), no significant change of the diffusion ellipsoids can be observed. As observed in fig. 3, the shape of the ellipsoids does not change significantly along the CG for both patients (arrows).

For the quantification of CC integrity, the FA inside the left (contralateral) part of the CC is determined along cross sections perpendicular to the neighboring CG. The resulting FA profiles for all considered tumor patients and the healthy volunteer are given in figure 6 (left) as a function of the frontal-occipital distance from the middle of the CC. The FA values for the volunteer (M, 29 y) and the patient without contralateral tumor progress (M, 47 y) decrease not significantly along the CC. In contrast to that, the FA values for the patients with contralateral tumor progress decrease
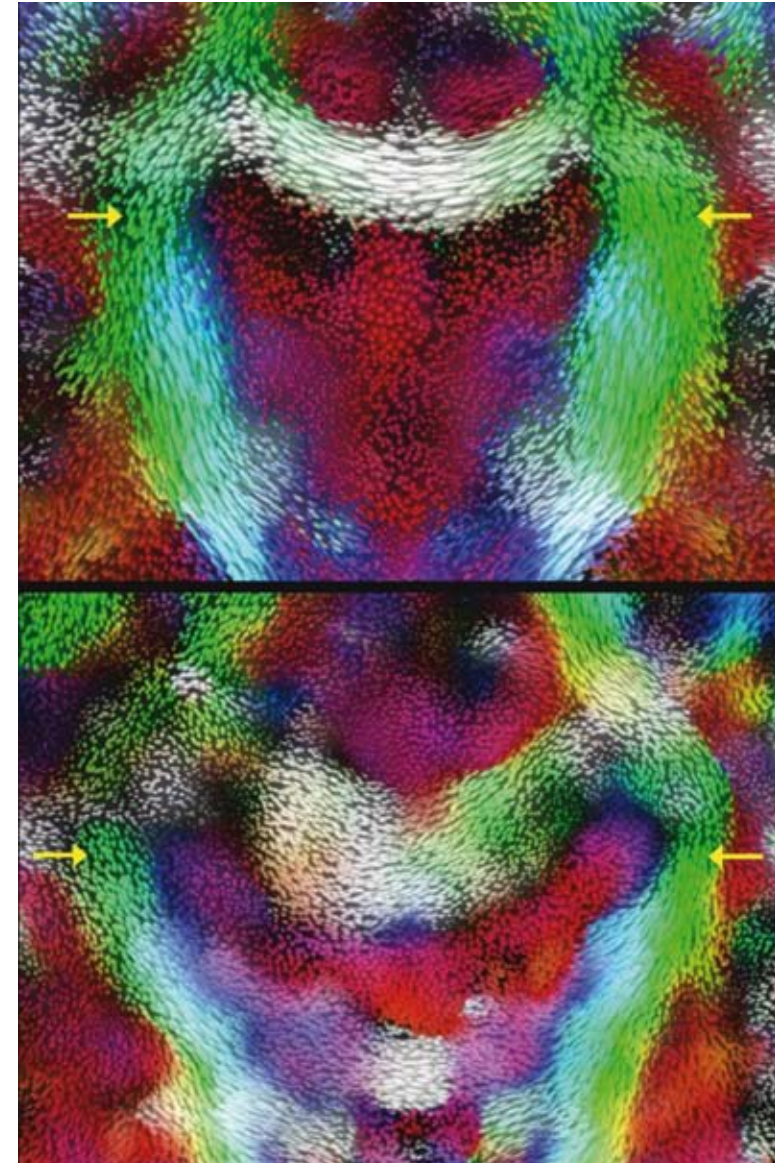
Figure 5 Diffusion ellipsoids for the left and right pyramidal tracts at the internal capsule. As in figure 3, infiltration of the right PT for the patient without (top) and with (bottom) contralateral progress is indicated by smaller and more isotropic ellipsoids compared to the left PT(arrows).
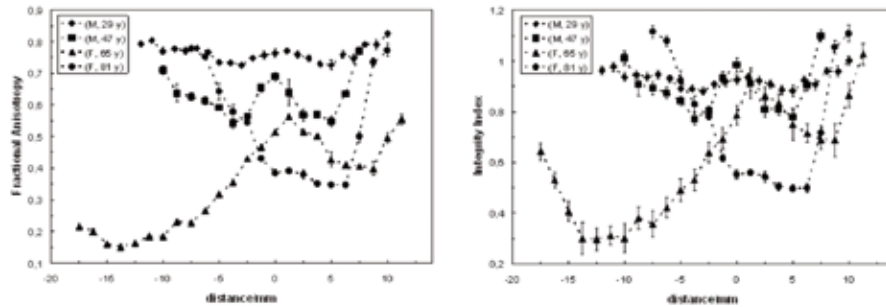
Figure 6 Left: Profiles of the FA inside the CC as a function of the frontal-occipital distance from the center (distance = 0) of the CC. The FA values for the volunteer (M, 29 y) and the patient without contralateral tumor progress (M, 47 y) decrease not significantly along the CC. The FA values for the patients with contralateral tumor progress decrease significantly in the middle-posterior part of the CC for the (F, 81 y) patient and in the anterior part of the CC for the (F 65, y) patient, respectively. Right: Profiles of the Integrity Index. The profiles for the volunteer (M, 29 y) and the tumor patient without contralateral progress (M, 47 y) are comparable, while for the patients with contralateral progress (F, 65 y; F 81 y), the Integrity Index decreases significantly at locations of CC-infiltration.

significantly in the middle-posterior part of the CC for the (F, 81 y) patient and in the anterior part of the CC for the (F 65, y) patient, respectively. The positions of the reduced FA are in correspondence with the infiltration locations revealed in the visualization of the DTI data.

In order to quantify white matter infiltration in an age normalized way, we define the Integrity Index, which is the diffusion anisotropy inside the infiltrated fiber bundle normalized by the diffusion anisotropy in some healthy fiber tissue. We use the FA inside the left cerebral peduncle for the normalization of the FA values inside the CC. The resulting profiles of the Integrity Index for the CC are given in figure 6 (right). The profiles for the volunteer (M, 29 y) and the tumor patient without contralateral progress (M, 47 y) are comparable, while for the patients with contralateral progress (F, 65 y; F 81 y), the Integrity Index decreases significantly at locations of CC infiltration.

Conclusion

In comparison to anatomical MR imaging, the introduced DTI-based visualization of fiber tissue by color maps and diffusion ellipsoids permits an accurate identification of particular fiber bundles leading to the periphery of infiltrating brain tumors. Inside those fiber bundles, infiltration can be detected in the color maps as well as in the diffusion ellipsoids by a reduced FA. This is demonstrated in the present work for the CC and the PT. Furthermore, the DTI data of the CC and CG suggests that brain tumors preferably infiltrate along fibers and but not in perpendicular directions, which is in accordance to pathological findings.

Infiltration of the CC is quantified by a robust and reproducible method for the determination of diffusion properties. The quantification method uses a probabilistic mixture model for the three eigenvalues of the DT inside the fiber bundle and surrounding background tissue. Thus, quantification results become independent of an arbitrary user defined ROI, which makes reproducible quantification and intra-subject comparison of white matter infiltration possible. For the comparison of subjects of different age, we introduce the Integrity Index, which measures the diffusion anisotropy inside an infiltrated fiber bundle normalized by the diffusion anisotropy in a specific region of healthy fiber tissue. It turns out, that the Integrity Index is significantly reduced inside the CC for the patients with contralateral tumor progress.

Visualization and quantification results suggest that the introduced DTI-based methods allow for an early, direct, and sensitive detection of white matter infiltration in particular fiber bundles. Thus, DTI based assessment of white matter infiltration has the potential to improve therapeutic decisions and to minimize interventional risk.

References

1   **Scherer HJ.** Structural Development in Gliomas. AM J Cancer 1938, 34; 333-351

2   **Johnson PC,** Hunt SJ, Drayer BP. Human cerebral gliomas: correlation of postmortem MR imaging and neuropathologic findings. Radiology 1989 Jan; 170:211-217

3   **Basser PJ,** Mattiello J, LeBihan D. Estimation of the effective self-diffusion tensor from the NMR spin echo. J Magn Reson B. 1994 Mar; 103(3): 247-254.

4   **Basser PJ,** Mattiello J, LeBihan D, MR diffusion tensor spectroscopy and imaging. Biophys J. 1994 Jan; 66(1): 259-267.

5   **Mori S,** van Zijl PC. Fiber tracking: principles and strategies - a technical review. NMR in Biomedicine. 2002 Nov; 1 (7-8): 468-480.

6   **Schlüter M,** Konrad-Verse O, Hahn HK, Stieltjes B, Rexilius J, Peitgen H-O. White matter lesion phantom for diffusion tensor data and its application to the assessment of fiber tracking. SPIE Conference on Medical Imaging; 2005 Feb; San Diego, CA.

7   **Stieltjes B,** Kaufmann WE, van Zijl PC, Fredericksen K, Pearlson GD, Solaiyappan M, Mori S. Diffusion tensor imaging and axonal tracking in the human brainstem. Neuroimage. 2001 Sep; 14(3): 723-735.

8   **Kindlmann G.** Superquadric Tensor Glyphs. IEEE International Symposium on Visualization; 2004.

9   **Schlüter M,** Stieltjes B, Rexilius J, Hahn HK, Peitgen H-O. Unique planar color coding of fiber bundles and its application to fiber integrity quantification. IEEE International Symposium on Biomedical Imaging; 2004 Apr 15-18; Arlington,VA. IEEE Catalog Number: 04EX821C, ISBN: 0-7803-8389-3: 900 – 903

10 **Price SJ,** Burnet NG, Donovan T, Green HA, Pena A, Antoun NM, Pickard JD, Carpenter TA, Gillard JH. Diffusion tensor imaging of brain tumours at 3T: a potential tool for assessing white matter tract invasion? Clin Radiol. 2003 Jun; 58(6): 455-462.

11 **Price SJ,** Pena A, Burnet NG, Jena R, Green HA, Carpenter TA, Pickard JD, Gillard JH. Tissue signature characterisation of diffusion tensor abnormalities in cerebral gliomas. Eur Radiol. 2004 Oct; 14(10):1909-17.

12 **Provenzale JM,** McGraw P, Mhatre P, Guo AC, Delong D. Peritumoral brain regions in gliomas and meningiomas: investigation with isotropic diffusion-weighted MR imaging and diffusion-tensor MR imaging. Radiology. 2004 Aug; 232(2): 451-60.

13 **Tropine A,** Vucurevic G, Delani P, Boor S, Hopf N, Bohl J, Stoeter P. Contribution of diffusion tensor imaging to delineation of gliomas and glioblastomas. J Magn Reson Imaging. 2004 Dec; 20(6): 905-12.

14 **MeVisLab.de** [homepage on the internet]. Bremen: MeVis gGmbH [updated 2005 Jan 18]. Available from: http://www.mevislab.de/.

— 6 —

Diffusion tensor imaging in primary brain tumors: reproducible quantitative analysis of corpus callosum infiltration and contralateral involvement using a probabilistic mixture model

B. Stieltjes, M. Schlüter, B. Didinger, M.A. Weber, H.K. Hahn, P. Parzer, J. Rexilius, O. Konrad-Verse, H.O. Peitgen, M. Essig

Diffusion Tensor Imaging (DTI) has been advocated as a promising tool for delineation of the extent of tumor infiltration by primary brain tumors. First reports show conflicting results mainly due to difficulties in reproducible determination of DTI-derived parameters. A novel method based on probabilistic voxel classification for a user independent analysis of DTI-derived parameters is presented and tested in healthy controls and patients with primary brain tumors. The proposed quantification method proved to be highly reproducible both in healthy controls and patients. Fiber integrity in the Corpus Callosum (CC) was measured using this quantification method and the profiles of Fractional Anisotropy (FA) provided additional information of the possible extent of infiltration of primary brain tumors when compared to conventional imaging. This yielded additional information on the nature of ambiguous contralateral lesions in patients with primary brain tumors. The results show that DTI derived parameters can be determined reproducibly and may have a strong impact on evaluation of contralateral extent of primary brain tumors.

Introduction

Gliomas are intra-axial brain tumors without discrete boundaries on histology. The WHO classification divides this group of tumors in those with and without stable histology (WHO grade I and II-IV respectively). However, in the majority of cases, low grade tumors tend to transform to higher grade tumors that infiltrate the surrounding tissue. They account for 26% of childhood cancer deaths (Duffner et al., 1986) and 2% of adult cancer death in the USA (Legler et al., 1999). One of the main limiting factors of current treatment planning is the inability to fully assess tumor infiltration and hence, better tumor delineation could improve treatment results considerably. In clinical practice, the tumor border is estimated by the FLAIR- hyperintensity though it is well recognized that tumoral infiltration may well extend beyond this boundary showing the limits of this method (Johnson et al., 1989). Moreover, other cerebral pathologies like stroke, edema or gliosis also appear hyperintense on T_2-weighted imaging. Thus, evaluation of the nature of contralateral lesions can be challenging. Moreover, evaluation of contralateral extent is of critical importance in therapeutic decision making since in patients with contralateral tumor growth chances of local control are minimal (Mitchel et al., 2005).

Diffusion Tensor Imaging (DTI) is a technique that can characterize the spatial properties of molecular water diffusion (Stejskal et al., 1965). The application of this technique to the brain revealed that these spatial properties are anisotropic in white matter (WM). This directionality has been attributed to highly directionally ordered structures like axons and myelin sheets (Beaulieu et al., 1994, Basser et al., 1996). Using DTI, both the magnitude of anisotropy and the preferential direction of water diffusion can be quantified. Several measures for the determination of the magnitude of anisotropy were introduced. In this study, we used the Fractional Anisotropy (FA) as a measure of fiber integrity (Basser et al., 1996). Using this and other measures, previous studies have tried to analyze peritumoral WM infiltration by primary brain tumors especially with regard to peritumoral hyperintense regions (Price et al., 2003, Price

et al., 2004, Provenzale et al., 2004, Tropine et al., 2004). So far, these studies have shown conflicting results regarding the ability of DTI for defining tumor extent through differences in FA in surrounding normal-appearing WM in gliomas. Conflicting evidence from these studies is primary discussed in the perspective of different methods of data analysis. This is truly one of the main challenges of quantitative DTI at present. There is no standard for analysis of DTI data and currently most studies use region of interest (ROI) based analysis for FA quantification. ROI analysis is known to be both user dependent and time consuming. Furthermore, these ROIs are frequently

drawn on anatomical images and then overlaid on FA maps with considerable mismatch problems.

   In this paper we describe a novel, user-independent ROI analysis that allows for rapid, clinically feasible and robust analysis of DTI data. Quantification is performed directly on the DTI dataset preventing mismatch problems. We applied this method to quantification of fiber integrity of the Corpus Callosum (CC) and used it as an indicator for contralateral involvement and evaluation of ambiguous contralateral lesions in patients with primary brain tumors. As mentioned before, high grade primary brain tumors tend to infiltrate WM and grow continuously. It is thought that contralateral lesions are in contact with the primary tumors in analogy to growth seen in mushrooms connected by a mycelium (Zlatescu et al., 2001). Thus, if a contralateral lesion is seen and this lesion is malignant, we hypothesized a decrease in FA either due to a reduced CC fiber integrity caused by tumor infiltration or reduction in overall FA due to a reduction of the white matter amount caused by partial tumor occupation of each voxel. In this study we showed that our proposed method for DTI-based quantification of fiber integrity is largely user independent and provides a means of rapid and robust analysis of CC fiber integrity and infiltration. Our initial results indicate that quantitative DTI predicted contralateral growth and was able to depict infiltration not visualized using conventional imaging.

Materials and methods

Patients and Control Subjects

Informed consent was obtained from all subjects in accordance with the Declaration of Helsinki and ethical approval was granted by the ethics committee of the Heidelberg University. Fifteen patients with supratentorial gliomas (WHO grades II-IV, age range 29-47 years, mean age 40 years, SD +/- five years) were included in the study. To evaluate potential CC infiltration (CCI), these 15 patients were divided in three groups of five patients each: patients without contralateral lesions (CLL) and no midline CC infiltration (CLL-/CCI-), patients with contralateral lesions but no infiltration of the CC (CLL+/CCI-) and patients with contralateral lesions and CC infiltration (CLL+/CCI+), based on conventional imaging Furthermore, we included a control group of five age-matched healthy controls.

MRI Data Acquisition

Imaging was performed on a 1.5 T whole-body clinical scanner and a quadrature head coil (Magnetom Symphony, Siemens Medical Solutions, Erlangen, Germany) with a gradient strength of 40 mT/m. A single shot echoplanar imaging technique with a dual bipolar diffusion gradient and a double spin echo was utilized for reduction of eddy currents using the following parameters: TR/TE 4700/78, field of view 240 mm, data matrix of 96x96 yielding an in plane resolution of 2.5 mm. We acquired 50 axial slices with a thickness of 2.5 mm and no gap, 6 gradient directions and two b-values (0 and 1000 s/mm^2). In order to increase the signal to noise ratio, 10 subsequent DTI datasets were acquired. For initial evaluation of contralateral involvement we used a FLAIR-sequence with the following parameters: TR/TE/TI 9000/114/2500, field of view 240 mm, data matrix 256x256 yielding an inplane resolution of 0.9 mm. We acquired 23 slices with a thickness of 5 mm and a 1.5 mm gap.

ON CONNECTIVITY IN THE CENTRAL NERVOUS SYSTEM — A MAGNETIC RESONANCE IMAGING STUDY

DIFFUSION TENSOR IMAGING IN PRIMARY BRAIN TUMORS: REPRODUCIBLE QUANTITATIVE ANALYSIS OF CORPUS CALLOSUM INFILTRATION AND CONTRALATERAL INVOLVEMENT USING A PROBABILISTIC MIXTURE MODEL

Data Preprocessing

In order to increase the SNR, the 10 independent DTI datasets were spatially matched and averaged. For registration, a rigid transformation model was assumed and the model parameters were determined by a rigid registration with normalized cross correlation as similarity measure. Since spatial motion of the subject has a magnitude of fractional voxel size, the matching becomes more accurate, if the data is resampled to a finer grid. For this purpose, we resampled the data to isotropic voxels of size 1.25 mm using a Cubic B-Spline for the data interpolation. After resampling, the independent datasets are automatically matched and averaged.

Quantification of Fiber Integrity

For the quantification of WM integrity, we assume that WM brain tissue is organized into fiber bundles consisting of dense and parallel axons. Then, reduction of axonal arrangement inside a specific fiber bundle should increase the amount of water diffusion perpendicular to the orientation of the fiber bundle. Another mechanism for reduction of FA in the presence of tumor growth could be a relative increase in isotropic components due to tumor presence. In both cases, the FA inside a pathological WM fiber bundle should be decreased compared to healthy fiber bundles. Thus, the FA inside a specific fiber bundle can serve as an indicator for fiber integrity (Price et al., 2003, Price et al., 2004, Provenzale et al., 2004, Tropine et al., 2004) and fiber integrity can be quantified by FA profiles along cross sections of this fiber bundle. In figure 1a cross section through a fiber bundle is schematically illustrated. However, in order to obtain the FA inside a specific fiber bundle we have to define which voxels in the cross section plane belong to that fiber bundle. This could be done by manually delineating a ROI around the fiber bundle, but obviously, this leads to strongly user dependent quantification results. Furthermore, due to partial volume effects, even an automatic and reproducible ROI delineation would result in variations of measured fiber integrity that are dependent on the resolution of the data.
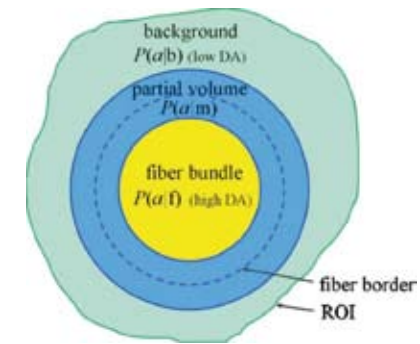
Figure 1 Probabilistic mixture model for a cross-section through a fiber bundle (yellow) with high amount of DA embedded in isotropic background (pastel green) with low amount of DA. The blue ring around the fiber bundle indicates partial volume voxels, with a mixture of the DTs of the fiber and background class. The conditional PDFs of the mixture model are denoted by P(a| f), P(a|b) and P(a|m) for the fiber, background and partial volume class, respectively.

Probabilistic Mixture Model for a Fiber Bundle in Isotropic Background

For the definition of our quantification model we suppose a ROI surrounding a cross section of a specific fiber bundle. Inside this, we propose a probabilistic mixture model including the two classes fiber (f) and background (b) (Schlüter et al., 2004, Schlüter et al., 2005). In addition to the two pure classes (f) and (b), a partial volume class (m), which is a mixture of (f) and (b), is added to the model. This is intended to make results independent of the resolution of the data. We use the Diffusion Tensor (DT) in each voxel inside the ROI for the classification of the data. After classification, the fiber integrity is quantified using the FA for the fiber class (f) only. Figure 1 illustrates the situation for one fiber bundle embedded in an isotropic background.

In order to make the classification robust to variations of initial conditions and numerical inaccuracies, and since the total number of data points within the ROI is limited, it is sensible to reduce parameters and to simplify the DT information considered for classification. Therefore, we assume that the diffusion tensors

ON CONNECTIVITY IN THE CENTRAL NERVOUS SYSTEM — A MAGNETIC RESONANCE IMAGING STUDY

DIFFUSION TENSOR IMAGING IN PRIMARY BRAIN TUMORS: REPRODUCIBLE QUANTITATIVE ANALYSIS OF CORPUS CALLOSUM INFILTRATION AND CONTRALATERAL INVOLVEMENT USING A PROBABILISTIC MIXTURE MODEL

of the two classes (f) and (b) inside the ROI have equal first principle axes e1f = e1b = e1 and the same amount of diffusion along this axis. The amounts of diffusion along the principle axes are described by the eigenvalues (λ1, λ2, and λ3) of the DT. Thus, we have λ1f = λ1b = λ1. The assumption implies that apart from the specific fiber bundle of interest no other fiber bundle should be inside the ROI. Note that the assumption is satisfied if the fiber bundle is embedded in isotropic background. The assumption of equal first principle axes of fiber and background tissue is not fulfilled for each fiber bundle in the brain. But for the CC considered here, it can be ensured since it is mainly embedded in isotropic CSF with arbitrary first principle axis. The cingulum located above the CC has an orientation approximately perpendicular to the CC and can be well separated from the CC by using DT based color maps.

For a fiber bundle consisting of mainly parallel axons the true DT can be well approximated by a DT that is invariant under rotation around its first principle axis. This implies that the two lower eigenvalues are similar (λ2 $\approx$ λ3). Note that the above assumption and this approximation imply that the diffusion tensors of the two classes (f) and (b) have the same eigensystem (e1, e2, e3). Now, the DT for the fiber and background (Df and Db) simplifies to (Schlüter et al. 2005)

$$D_{f,b} = \lambda_1 e_1\, e_1{}^T + \lambda_2{}^{f,b}\, e_2\, e_2{}^T + \lambda_3{}^{f,b}\, e_3\, e_3{}^T = \lambda_1\,[(a^{f,b} e_1\, e_1{}^T + (1 - a^{f,b})].$$

The quantity

$$a = 1 - (\lambda 2 + \lambda 3) / (2\,\lambda 1) \gg 1 - \lambda 2 / \lambda 1 \in [0,1], \text{ for } \lambda 1 \geq \lambda 2 \geq \lambda 3$$

is the only parameter differentiating between the two classes (f) and (b). Thus, it characterizes the two classes (f) and (b) completely and can be used as the single feature for the classification between fiber and background. We name this quantity Diffusion Anisotropy (DA), since it is zero for complete isotropic and one for complete anisotropic diffusion. It will be high inside the fiber class compared to the background (figure 1). Although it is similar to the FA, which is commonly used in

fiber integrity assessment, we use the DA as the classification feature for our probabilistic mixture model, because it follows directly from the above simplification of the DT. In the section 'Automatic Probabilistic Voxel Classification' we will see how to obtain arbitrary diffusion properties, especially the FA, from the classification result. The probabilistic mixture model is given by

$$P(a) = \pi f\, P(a|f) + \pi b\, P(a|b) + \pi m\, P(a|m), \quad \pi f + \pi b + \pi m = 1,$$

where P(a) is the Probability Density Function (PDF) for the DA. The prior probability for fiber, background and partial volume is denoted by πf, πb, and πm, respectively. The conditional PDFs of the DA, given the pure tissue classes fiber and background are denoted by P(a|f) and P(a|b), respectively. Both are modeled by Gaussian distributions with mean values mf and mb and variances σf and σb. Since the voxel extension is not negligible compared to the extension of the quantified fiber bundle, partial volume effects have to be considered. Therefore, we added the conditional PDF of the DA given the mixture class between fiber and background P(a|m) to the mixture model. In the following it is shown how this conditional PDF for the mixture class can be traced back to the Gaussian parameters of the pure classes.

Partial Volume Modeling of Diffusion Anisotropy

The diffusion weighted signal inside partial volume voxels sm(b) is a mixture of the pure class signals Sf and Sb (Alexander et al., 2001):

$$Sm(b) = (1-r)\, Sf(0)\, \exp(-\,b\, gT\, Df\, g) + r\, Sb(0)\, \exp(-\,b\, gT\, Db\, g).$$

Here, $\rho \in [0,1]$ describes the mixture parameter, g the diffusion weighting gradient and b the diffusion weighting strength also called the b-value. The fiber and background signal without diffusion weighting is given by Sf (0) and Sb (0), respectively. The DT for the fiber bundle and the background is denoted by Df and Db, respectively. The mixture of the diffusion weighted

ON CONNECTIVITY IN THE CENTRAL NERVOUS SYSTEM — A MAGNETIC RESONANCE IMAGING STUDY

DIFFUSION TENSOR IMAGING IN PRIMARY BRAIN TUMORS: REPRODUCIBLE QUANTITATIVE ANALYSIS OF CORPUS
CALLOSUM INFILTRATION AND CONTRALATERAL INVOLVEMENT USING A PROBABILISTIC MIXTURE MODEL

signals leads to a two tensor model which can no longer be described by a single DT (Alexander et al., 2001). However, if the difference between Df and Db is small compared to the inverse of the b-value (|Df - Db| ≪ 1/b) the mixture of the diffusion weighted signals can be approximated by the diffusion weighted signal for the mixture of Df and Db:

$$P(a\,|\,m) = S_m(0)\exp(-bg^T D_m g)\left[1 - bg^T \Delta Dg(1-\rho)\rho\frac{\Delta S(0)}{S_m(0)} + O(|b\Delta D|^2)\right], \text{ with}$$

$$
\begin{aligned}
S_m(0) &= (1-\rho)S_f(0) + \rho S_b(0)\\
D_m &= (1-\rho)D_f + \rho D_b\\
\Delta S(0) &= S_b(0) - S_f(0)\\
\Delta D &= D_b - D_f
\end{aligned}
$$

If we neglect terms of order |b ΔD| and higher, we can deal with a one tensor model described by the mixture tensor Dm. The assumptions made for the probabilistic mixture model imply that the mixture of Df and Db can be described by the mixture of their DAS:

P(a|m) = (1-ρ) af + ρ ab .

If we assume that the mixture parameter r is uniformly distributed the conditional PDF of the DA given the mixture class between fiber and background P(a|m) can be calculated from the means and variances of the Gaussian distributions for the two pure classes (f) and (b) [Noe]:

$$P(a\,|\,m) = (1/\sqrt{2\pi})\int_0^1 \frac{d\rho}{\sqrt{\rho^2\sigma_b^2 + (1-\rho)^2\sigma_f^2}}\exp\left(-\frac{[(1-\rho)m_f + \rho m_b - a]^2}{2[(1-\rho)^2\sigma_f^2 + \rho^2\sigma_b^2]}\right)$$

Automatic Probabilistic Voxel Classification

The parameters πf , mf, σf, and πb, mb, σb of the probabilistic mixture model are automatically adapted to the DA data inside the ROI by a probabilistic clustering algorithm (Laidlaw et al., 1998, Noe et al., 2001). This algorithm generalizes the EM Algorithm (McLachlan et al., 1997) to Gaussian mixture models with additional partial volume classes. The probabilistic clustering algorithm is applied to the normalized histogram of the discretized DA data inside the ROI:

$$h(a) = \frac{1}{|\text{ROI}|}\sum_{x\in\text{ROI}}\delta[a - a_x], \text{ with } \delta[0] = 1 \text{ and } 0 \text{ otherwise}.$$

For initialization of the clustering algorithm, the values for the Gaussian parameters mf, σf and mb, σb are estimated from voxels with DA values above and below some upper and lower threshold, respectively. The prior class probabilities are set to πf = πb = πm = 1/3. The final parameter estimation obtained from the clustering algorithm is very robust to variation of these initial values. Only for extremely high or low DA thresholds leading to a very small set of voxels for the initial estimation of the Gaussian parameters, the algorithm can be trapped in a further attractor. However, in cases with more than one attractor, the log-likelihood

$$L = \frac{1}{|\text{ROI}|}\sum_{x\in\text{ROI}}\log[P(a_x)] = \sum_a h(a)\log[P(a)]$$

is used as a quality measure of the parameter estimation and the estimation with highest log-likelihood is accepted as the final result. For a given set of model parameters, the class probability of each voxel x∈ROI can be calculated from its DA by Bayes' rule:

P(c|ax) = πc P(ax|c) / P(ax), with c = f, b, m .

In figure 2 a typical class probability map is shown for a coronal cross section at the center of the CC. Yellow, pastel green and blue indicates high probability for fiber (f), background (b), and

ON CONNECTIVITY IN THE CENTRAL NERVOUS SYSTEM — A MAGNETIC RESONANCE IMAGING STUDY

DIFFUSION TENSOR IMAGING IN PRIMARY BRAIN TUMORS: REPRODUCIBLE QUANTITATIVE ANALYSIS OF CORPUS CALLOSUM INFILTRATION AND CONTRALATERAL INVOLVEMENT USING A PROBABILISTIC MIXTURE MODEL
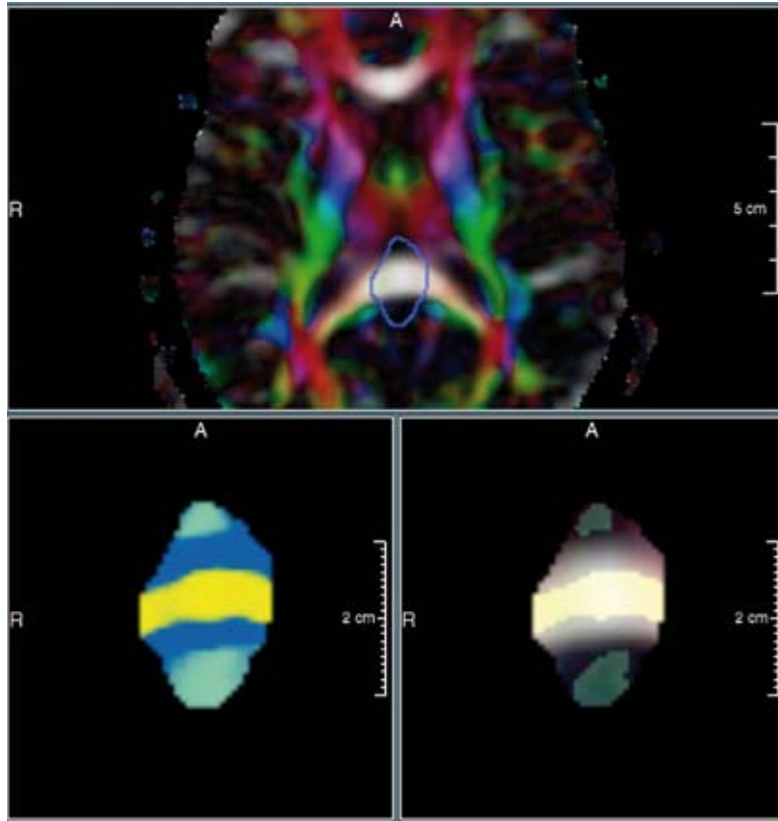
Figure 2 Quantification of the fiber integrity in an axial cross-section at the posterior part of the CC. First, on the DTI color map, the user defines an ROI including the middle part of the CC (top). Then, inside the ROI (bottom, right), the probabilistic mixture model is applied and the model parameters are automatically adapted by the probabilistic clustering algorithm leading to a classification into fiber (yellow), background (pastel green) and partial volume (blue) tissue (bottom, left). After clustering, diffusion properties, e.g., FA, inside the fiber of interest (yellow region) can be calculated from the adapted model parameters.

partial volume (m), respectively. From the class probability maps mean values inside a given class can be calculated for arbitrary quantities Q:

$$\langle Q \rangle_c := \frac{1}{|ROI|\,\pi_c} \sum_{x \in ROI} P(c\,|\,a_x)\,Q_x, \text{ with } c = f,b,m.$$

Of course, Q can be chosen equal to every combination of the eigenvalues of the DT. Thus, for Q equal to FA and c = f, the mean FA inside the fiber can be calculated. Furthermore, by calculating second moments, statistical errors for the mean values caused by image noise can be estimated by

$$\Delta^2 \langle Q \rangle_c = \frac{1}{|ROI|\,\pi_c} \left(\langle Q^2 \rangle_c - \langle Q \rangle_c^{\,2} \right).$$

As argued above the FA inside a particular fiber bundle can serve as an indicator for its integrity. With the probabilistic mixture model described here, we are now able to determine fiber integrity by $\langle FA \rangle f$, which is independent of the user-defined ROI. This will be demonstrated below.

Patient Measurements and Evaluation

Using the aforementioned method for fiber quantification, we measured the FA at five different positions of the CC as indicated in figure 3 to sample the fiber integrity along the CC. To further reduce measurement variance it was agreed to include the part of the CC medial to the cingulum on either sides. All measurements were performed by two independent readers blinded to the patient group as well as to results of the other reader. Intra- and intrerreader variability was evaluated by Intra Class Correlations (ICC) between these measurements using Stata 9.0 (Stata Statistical Software: Release 9. College Station, TX: StataCorp LP.). Mean FA Values of the five positions of the different groups were compared to age-matched controls with analysis of variance. For the pairwise post hoc group comparisons Sidak adjusted p-values were used to correct for multiple testing. A p-value of <0.05 was chosen as significance level.

ON CONNECTIVITY IN THE CENTRAL NERVOUS SYSTEM — A MAGNETIC RESONANCE IMAGING STUDY

DIFFUSION TENSOR IMAGING IN PRIMARY BRAIN TUMORS: REPRODUCIBLE QUANTITATIVE ANALYSIS OF CORPUS CALLOSUM INFILTRATION AND CONTRALATERAL INVOLVEMENT USING A PROBABILISTIC MIXTURE MODEL
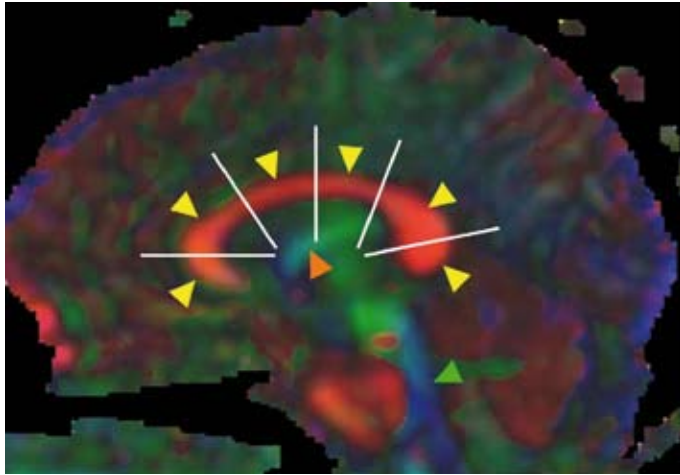
Figure 3 DTI-based color map at a mid-sagittal cross-section of the CC. Yellow, orange and green arrows indicate the CC, the fornix and the corticospinal tract respectively. The fiber integrity is determined at 5 different positions of the CC as indicated by the solid white bars. Planes for quantification are chosen perpendicular to the center line of the CC.

Results

Fiber integrity measurements in five positions of the CC in each of the 15 glioma patients and five controls were performed using the above described novel probabilistic ROI-clustering approach. The aim of our study was twofold. First, to prove that this approach is reproducible and largely independent of the ROI surrounding cross sections of the CC. Secondly, to evaluate if and how the quantified fiber integrity of the CC differs in primary brain tumor patients with and without contralateral lesions. In particular, we wanted to evaluate if this method could yield additional information on the nature of ambiguous contralateral lesions in such patients.

Robustness of Quantification Results to Variation of the ROI

In order to demonstrate the robustness of the probabilistic ROI clustering approach, we determined the FA and its statistical error
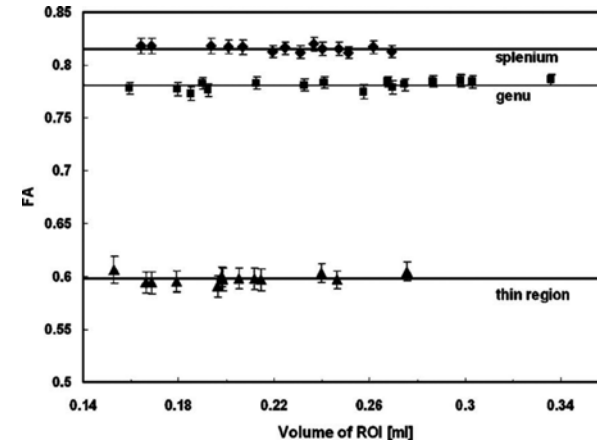
Figure 4 The FA determined by our quantification method at the splenium, genu and a thin region of the body of the CC plotted against the volume of the corresponding initial ROIs. The straight lines indicate the average over all delineations of the ROI at the splenium, genu and the thin region, respectively.

at the splenium, genu and a thin region of the CC for different initial ROI sizes. In figure 4 the resulting FAs at the splenium, genu and the chosen thin region of the CC are plotted against the volume of the delineated ROIs. The straight lines indicate the average over all delineations of the ROI at the splenium, genu and the thin region, respectively. We could verify that the variation of the FA resulting from different delineations of the ROI is below the statistical variation and small compared to FA differences in different regions of the CC. In other words, the probabilistic ROI-clustering approach proves to be highly robust to ROI-variations both in thicker and thinner parts of the CC.

Intra- and Interreader Reliability

The previous results suggest that using our probabilistic ROI-clustering method, intra- and interreader variability due to different ROI definition should be minimal. To evaluate this further we performed an intra- and interreader reliability test. For all subjects, all five measurement points were compared within and between readers. Comparison of the first and second

ON CONNECTIVITY IN THE CENTRAL NERVOUS SYSTEM — A MAGNETIC RESONANCE IMAGING STUDY

DIFFUSION TENSOR IMAGING IN PRIMARY BRAIN TUMORS: REPRODUCIBLE QUANTITATIVE ANALYSIS OF CORPUS CALLOSUM INFILTRATION AND CONTRALATERAL INVOLVEMENT USING A PROBABILISTIC MIXTURE MODEL

measurement of reader 1 and 2 yielded an ICC-value of 0.998 and 0.995 respectively indicating good intra-reader agreement (A measurement error of 4% and 7% respectively). Comparison of all four measurements (two measurements of reader 1 and two measurements of reader 2) yielded four ICC-values ranging between 0.996 and 0.999, indicating good inter-reader agreement (A measurement error between 4% and 6%). In accordance with the ROI-dependence test, these results show that within the CC the variance in measured FA induced by different readers or repeated measurement is minimal. Thus, our method reduces the time needed to evaluate the fiber integrity of the CC since no multireader studies need to be performed and results from different institutions can be compared reliably. Moreover, since the results are highly ROI-independent time for careful delineation could be saved. The total time for evaluation of the CC infiltration as described is less than two minutes. This is of great importance because reliability and quick availability of the results are the main factors for incorporation into clinical routine.

Visualization and Quantification of CC Fiber Integrity in Patients with and without Contralateral Lesions

After showing that the obtained results using this method are highly reproducible we evaluated the FA in the CC of different groups of patients and compared them to the healthy controls. Figure 5a shows a typical example of a patient without contralateral lesions on conventional imaging (CLL-/CCI). Both on conventional images (top), DTI derived color maps (center) and ellipsoid representation of the DT (bottom) the body of the CC is intact. Figure 5b shows a patient with contralateral lesions and infiltration of the CC on conventional imaging (CLL+/CCI+). In all imaging modalities a severe disruption of the CC can be seen. Figure 5c shows an example of a patient with contralateral lesions but no CC infiltration on conventional imaging (CLL+/CCI-). The CC shows a slight thinning in the DTI data especially at the body but no clear infiltration can be identified.
So based on visual inspection of conventional imaging, CLL-/CCI-
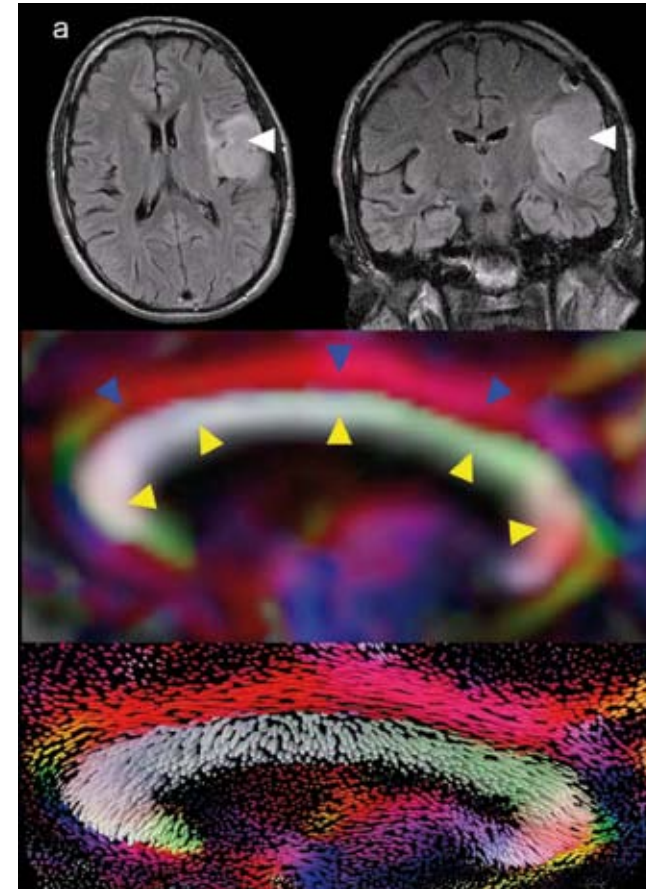
Figure 5a Visualization of tumor extent in patients from all three groups. (a) Grade II astrocytoma patient with a lesion in the left parietal lobe with no contralateral lesions and no CC infiltration on conventional imaging (CLL_/CCL_). (b) Grade II astrocytoma patient with a right-sided frontoparietal primary lesion with clear infiltration of the body of the CC and contralateral growth (CLL+/CCI+). (c) Grade II astrocytoma patient with a left parieto-occipital lesion and a contralateral hyperintensity in the occipital lobe but without infiltration of the CC on conventional imaging (CLL+/CCL_). Depiction of using FLAIR (top), DTI-based color maps (middle) and ellipsoid DT representation (bottom). In the FLAIR images, white arrows indicate the primary and red arrows the contralateral lesion. The color maps and the ellipsoid representation use a sagittal projection plane for color coding. White fibers of the CC are perpendicular to the chosen plane. Blue arrows indicate the cingulum, and based on quantification, yellow and red arrows indicate the intact and affected part of the CC respectively. Red arrows indicate regions with FA of two standard deviations below the average of the healthy controls. Elongated and isotropic ellipsoids show voxels with high and low FA, respectively.

ON CONNECTIVITY IN THE CENTRAL NERVOUS SYSTEM — A MAGNETIC RESONANCE IMAGING STUDY

DIFFUSION TENSOR IMAGING IN PRIMARY BRAIN TUMORS: REPRODUCIBLE QUANTITATIVE ANALYSIS OF CORPUS CALLOSUM INFILTRATION AND CONTRALATERAL INVOLVEMENT USING A PROBABILISTIC MIXTURE MODEL
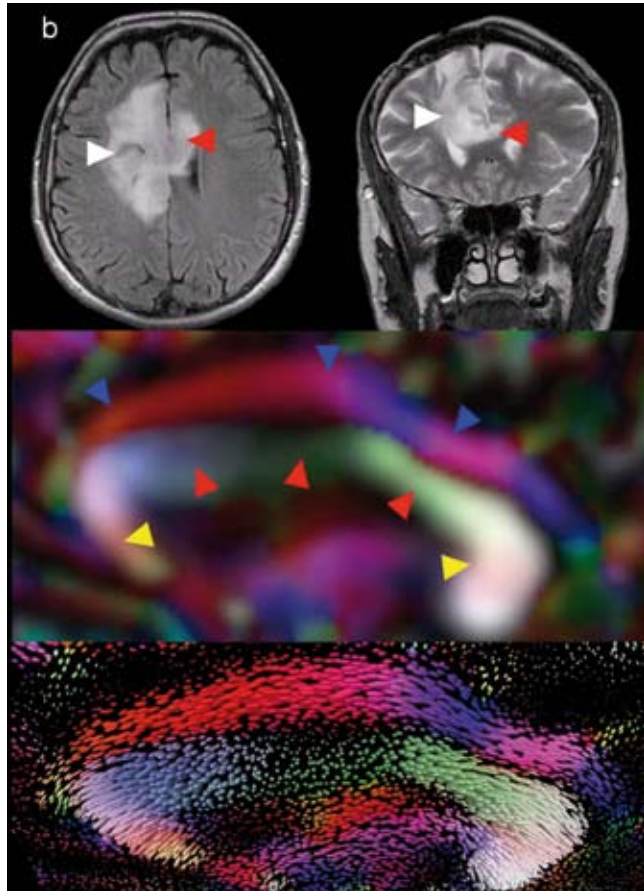
Figure 5b

Figure 5c

patients and CLL+/CCI- patients are hard to separate in terms of CC integrity. To see if our DTI-based quantification method may aid the separation of these two groups, we compared the profiles of FA along the CC of the patients to healthy controls. In Figure 6 the profiles of FA along the distance are shown (left=anterior, right=posterior). The profiles shown here correspond to the patients shown in figure 5. Patients without contralateral lesions show profiles that are comparable with healthy controls, i.e. with highest FA in the splenium and the genu of the CC and lower
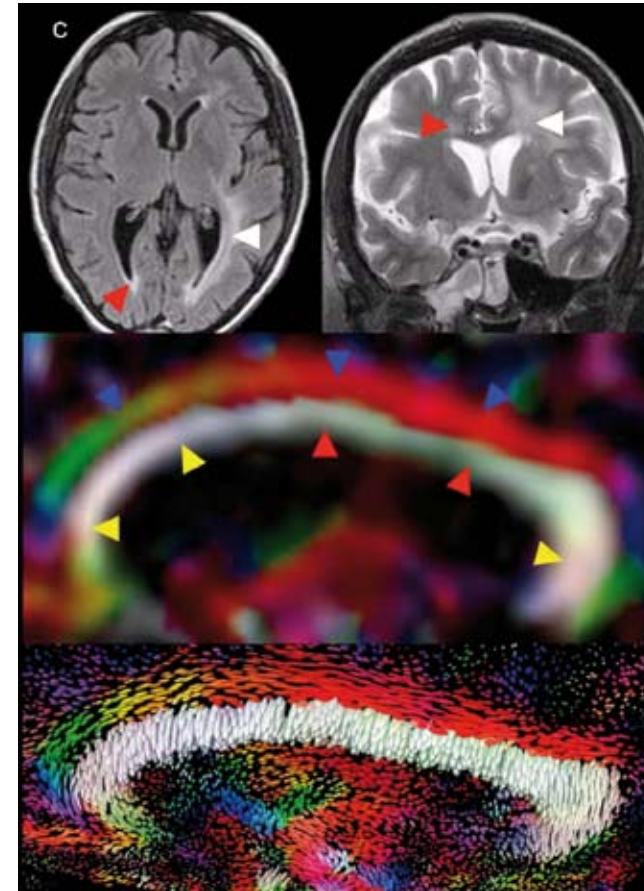
values in the body, as described before (Thomas et al., 2005, Hasan et al., 2005). Patients with CC infiltration on conventional imaging show clear deviations from the normal controls with values over two standard deviations below the average found in the control group at points of infiltration. This shows that infiltration of the CC leads to a strong decrease of FA. In some cases, the infiltration of the CC seen in quantification extends further than expected from visual inspection of conventional imaging. Also, regions without measurable changes in FA can be seen indicating that
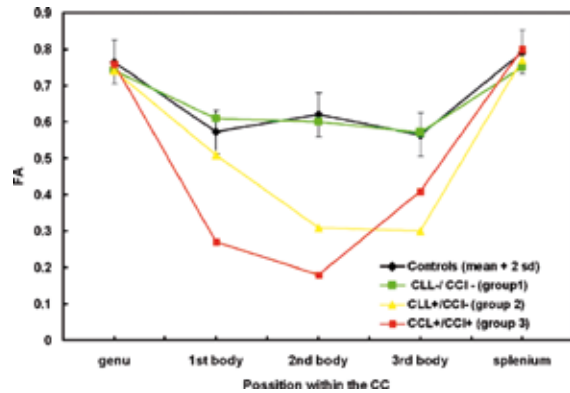
Figure 6 Comparison of profiles of FA in the CC of representative patients of each group and controls. Mean and two times the standard deviation of measured values at the five different positions of the controls are represented by the black curve. The curves of the FA for the patient without contralateral lesion and without CC infiltration (CLL_/CCL_) (with contralateral lesion and without CC infiltration (CLL+/CCL_) and with contralateral lesion and CC infiltration (CLL+/CCI+) are colored green, yellow and red respectively. The graphs presented here correspond to the patients shown in figure 5.

some parts of the CC may not yet be affected. In all patients without infiltration on conventional imaging but contralateral lesions (CLL+/CCI-) we saw a clear drop in FA with again values over two standard deviations below healthy controls. This indicates that the quantification method may depict infiltration of the CC that was not suspected on conventional imaging. Also, the position of reduced FA corresponds with the likely path of growth across the CC. For instance, in frontal contralateral lesions, the genu of the CC is affected and in central lesions the body shows reduced FA. Figure 7 shows a group comparison of mean FA over all 5 positions in all patient groups and healthy controls. There is no significant difference between group 1 (CLL-/CCI-) and healthy controls ($F_{(1,16)} < .001$, p>.999). Furthermore, there is a significantly lower FA in group 3 (CLL+/CCI+) when compared to healthy controls ($F_{(1,16)} = 25.22$, p=.0004). Moreover, group 2 (CLL+/CCI-) has a significantly lower FA than controls and was not significantly different from patients with visible infiltration ($F_{(1,16)} = 17.85$, p=.0019). This indicates, that in our sample, in all patients with a CLL an infiltration of the CC is likely, but this cannot always be
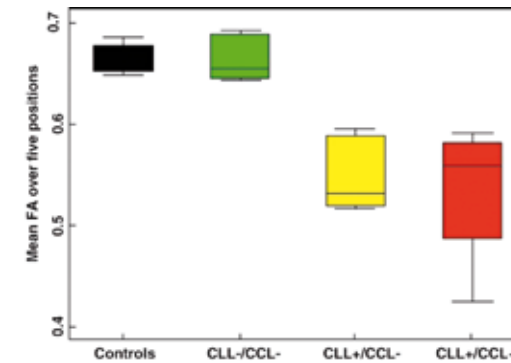
Figure 7 Comparison of mean FA between healthy controls and patient groups. Box plot indicating mean FA and standard deviation within the controls and three patient groups. As in Figure 6, black represents the controls, green, yellow and red represent the three patient groups, CLL-/CCI-, CLL+/CCI- and CLL+/CCI+, respectively. Abbreviations as in figure 6.

visualized using conventional imaging. Moreover, even DTI-based imaging modalities like color maps or ellipsoid representation of the DT can not reliably depict infiltration in these cases. Therefore, quantification of the FA inside the CC seems to be highly sensitive measure of changes in fiber integrity in the CCW due to tumor growth.

Evaluation of Ambiguous Contralateral Lesions Using the FA in the CC

As mentioned before it is thought that lesions in primary brain tumor patients are connected by small projections of tumor cells growing along the axonal tracts. In patients with CLL and CCI, some contralateral lesions are clearly tumorous. In these cases our results indicate that the lesions are indeed connected by such thin axonal proceedings of the tumor that cause an interruption of fiber integrity within the CC leading to a decrease in FA. In other patients within this group, however, at the time of inclusion, the nature of the contralateral lesion was uncertain. Our results indicate that if this lesion is tumorous the CC is

likely to be affected and shows a drop in FA. One patient came in for early follow up after symptoms worsened. His images are shown in figure 8. The initial anatomical image shows a left sided primary tumor and a line shaped T_2 hyperintensity on the lateral margin of the right lateral ventricle contralateral to the primary tumor. Conventional imaging showed no CC infiltration and the contralateral lesion was judged to represent physiological subependymal gliosis. The FA profile however shows a clear drop of FA in the central part of the CC. Again, the site of the infiltration fitted the likely path of contralateral growth. On follow-up, the contralateral lesion had grown considerably indicating its malignant nature. This case indicates that an early drop in FA may correlate with CC infiltration and moreover, that this information can aid the assessment of the nature of contralateral lesions.

Discussion

There are several reasons that have so far prevented DTI from becoming a widespread clinical application. The most important ones are reproducibility and processing time. Here we present a solution for these two major hurdles. We have shown that using our proposed probabilistic ROI-analysis fiber integrity in the CC can be evaluated rapidly and reproducibly. Using our method, the need for intra- and interreader reliability measurements becomes obsolete. Furthermore, time consuming precise ROI-delineation is not needed since the measured FA is very robust to changes in ROI size. Also, we have found indications that this readily available information on CC fiber integrity may be of great aid in deciding the nature of ambiguous CLL in patients with primary brain tumors. We found that in patients with tumorous CLL but no CCI on conventional imaging, the FA in the CC was significantly lower than in healthy controls and patients without CLL. Moreover, in patients with ambiguous CLL we found a similar drop in FA in the CC and after follow up, the CLL proved to be malignant.

In our study we found a clear distinction in growth pattern between the patients with and without CLL. Patients without CLL
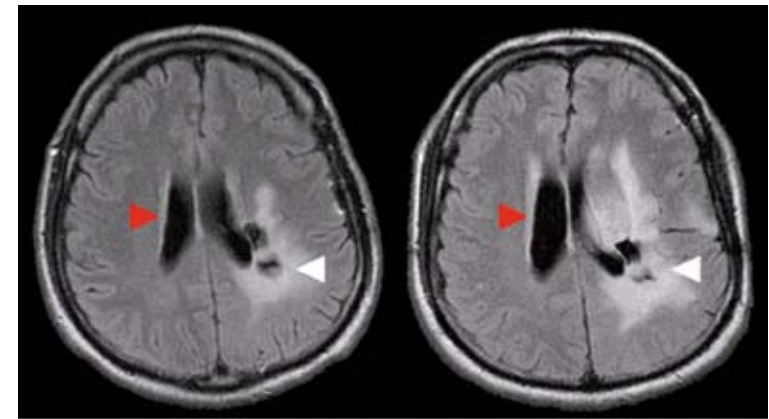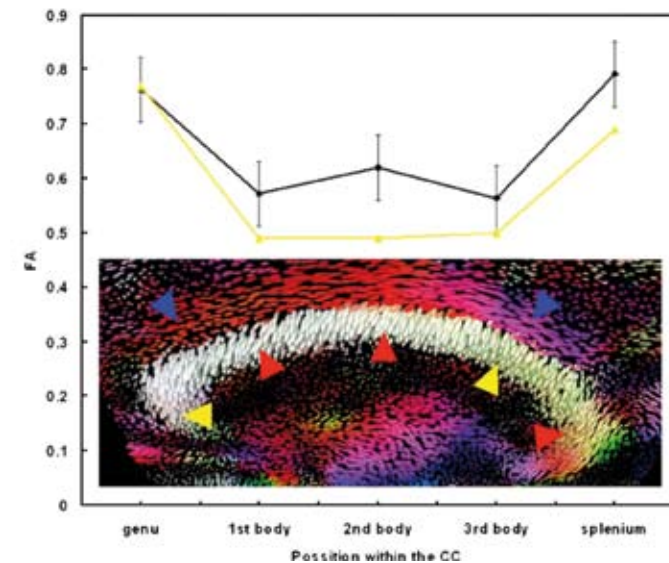
Figure 8 FA profile in a patient with progression at follow-up. Initial FLAIR imaging (top left) showed a primary lesion frontoparietal left (white arrow) with a contralateral periventricular hyperintensity (red arrow) without CC infiltration on conventional imaging. At follow-up (top right), both the primary (whitearrow) and the contralateral lesion (red arrow) show marked progress. Plot of the FA profile of this patient (below) at time of initial imaging (yellow curve) and healthy controls (black curve). Ellipsoid DT representation as described before. Blue arrows indicate the cingulum, and based on quantification, yellow and red arrows the intact and affected part of the CC respectively.

ON CONNECTIVITY IN THE CENTRAL NERVOUS SYSTEM — A MAGNETIC RESONANCE IMAGING STUDY

DIFFUSION TENSOR IMAGING IN PRIMARY BRAIN TUMORS: REPRODUCIBLE QUANTITATIVE ANALYSIS OF CORPUS CALLOSUM INFILTRATION AND CONTRALATERAL INVOLVEMENT USING A PROBABILISTIC MIXTURE MODEL

did not show an involvement of the cc whereas patients with CLL showed marked infiltration of the cc, even if not yet visible on conventional imaging. These findings may correlate with evidence from neuropathological research that has shown that the migration of tumor projections in primary brain tumors is dictated by specific genetic changes leading to infiltrative growth and contralateral involvement (Zlatescu et al., 2001). It seems that in patients without CLL, these genetic alterations did not take place preventing the tumor from contralateral extension whereas in patients with CLL, this change has occurred. This clear grouping of patients might reflect their underlying genetic differences.

If so, our method might help, not only to evaluate contralateral involvement but also to yield in situ information about the possible malignancy of the tumor. Another finding of our study is the marked reduction of FA in the cc in patients where conventional imaging showed no signs of CCI. Our data suggests that DTI is more sensitive to infiltration than conventional FLAIR imaging. As mentioned before, DTI is principally sensitive to changes at the microscopic level of fiber architecture whereas the exact reasons for FLAIR-hyperintensity of primary brain tumors are partly unclear, although it is supposed to correlate to cellular density, tumor neovascularity and edema. These processes are prominent in areas of large tumor masses but are less important in smaller tumor projections. This may well explain the discrepancy we found between conventional imaging and DTI, where small alterations in fiber architecture can lead to changes in FA. The fact that these initial changes are small, stresses the importance of our reproducible quantification method since user-induced variance would obscure these initial changes from detection.

Corpus Callosum fiber integrity in healthy controls has been evaluated in several studies. In controls we found a mean FA in the genu, the body and splenium of the cc of 0.77, 0.62 and 0.80 respectively. In comparison to these studies our results are 0.15 to 0.20 points higher than found in these studies (Thomas et al., 2005, Hasan et al., 2005). This could be attributed to slight differences in ROI placement and subject age but then, we would have expected a more mixed result, i.e. our results would sometimes be higher and sometimes lower than found in other studies.

In these aforementioned studies, ROIs were either inserted directly in the DTI or normalized and overlaid on a T_1-weighted dataset. Both methods do not model for partial volume effects, increasing the amount of CSF signal inside the voxels of the ROIs and thus reducing the measured FA. Note in figure 2 that it is hard to define the border between CSF and cc and that the clustering algorithm shows a relatively large area of partial volume. Our method provides a more stable and reproducible measure of the fiber integrity within the fiber core leading to higher FA values when compared to studies using conventional ROI-placement.

We expect that, using our method, the sensitivity of DTI to relatively small changes in fiber architecture is enhanced compared to conventional FA measurements. If these initial findings are strengthened in a larger, more heterogeneous patient population, we believe that DTI can play an important role in the clinical evaluation of intra axial brain tumors. If we can generalize our model, we might be able to depict the overall tumor extension in a more reliable fashion than now possible. This might help to aid therapy decisions and planning and could be a key to improvement of therapy.

This also touches on one of the limitations of our current approach. Since we assume fibers inside the ROI to have a similar direction, the technique performs well in isolated fiber bundles but not in ROIs with more than one fiber system inside. To overcome this problem, we have developed a novel color-coding scheme that visualizes small differences in fiber direction (Schlüter et al., 2004). This helps to exclude other fiber systems from the ROI in areas like the internal capsule, where different bundles lie directly adjacent to another. Still, our technique does not yet represent a general approach where we can show on a slice by slice basis where infiltration is likely to have occurred. In our study we found a clear separation of patients with and without CLL based on FA in the cc regardless of the fact if these changes could bee seen using conventional imaging. Since we only sampled the mid sagittal plane of the cc, it can be assumed that eventually one will find patients with initial normal cc FA where on follow up, an infiltration will be present due to the fact that the tumor at the initial time point had not

reached the sampled part of the CC. This is another reason why a generalization of the method towards a slice by slice method would improve the overall sensitivity to infiltration.

Another limitation of this study is the patient groups. In the CLL+/CCI- group all patients had CCI on DTI. This makes it impossible to judge what the CC would look like in patients with an ambiguous CLL that turns out to be benign. Currently, we are undertaking a longitudinal study including DTI, PWI and spectroscopic imaging to clarify this question.

Also, in our study we tested our method on one fixed measurement protocol. Using this protocol our results were highly reproducible. However, we did not systematically evaluate the possible influence of different acquisition schemes resulting in changes in SNR, resolution, different b-values and number of measured diffusion directions on our quantification method. Though it was not the main scope of our research, we did test the effect of reduction of the number of independent DTI measurements on the quantified FA and found that a reduction from 10 to 3 measurements did not significantly alter the found FA indicating that the algorithm is quite noise-insensitive. Furthermore, recently acquired datasets on a 3 Tesla scanner and datasets acquired using 12 or 30 diffusion directions indicate that differences in these imaging parameters do not strongly affect the quantification method but further more systematic evaluation is warranted to evaluate these influences in their full extend.

In conclusion, we present a novel method for DTI-based ROI-analysis of fiber integrity in the CC. We have shown that the method is fast and reproducible and that the values derived from this method have clinical relevance in the evaluation of CLL in patients with intraaxial primary brain tumors. In all patients with CLL and no CCI on conventional imaging we found marked drops in FA indicating disturbed fiber integrity. This shows that quantitative DTI may be suitable for reliable depiction of WM infiltration by primary brain tumors.

References

1 **Alexander, A.L.,** Hasan, K.M., Lazar, M., Tsuruda, J.S., Parker, D.L., 2001Analysis of Partial Volume Effects in Diffusion-Tensor MRI. Magn Reson Med. May; 45(5): 770-780.

2 **Basser, P.J.,** Pierpaoli, C., 1996. Microstructural and physiological features of tissue elucidated by quantitative-diffusion-tensor-MRI. J Magn. Reson. B. 111(3), 209-219.

3 **Beaulieu, C.,** Allen, P.S., 1994. Determinants of anisotropic water diffusion in nerves. Magn. Res. Med. 31, 394-400.

4 **Duffner, P.K.,** Cohen, M.E., Myers, M.H., Heise, H.W., 1986. Survival of children with brain tumors: SEER Program, 1973-1980. Neurology 36, 597-601.

5 **Hasan, K.M.,** Gupta, R.K., Santos, R.M., Wolinsky, J.S., Narayana, P.A., 2005. Diffusion tensor fractional anisotropy of the normal-appearing seven segments of the corpus callosum in healthy adults and relapsing-remitting multiple sclerosis patients. J Magn Reson Imaging. Jun 21(6), 735-43.

6 **Johnson, P.C.,** Hunt, S.J., Drayer, B.P., 1989. Human cerebral gliomas: correlation of postmortem MR imaging and neuropathologic findings. Radiology Jan 170, 211-217.

7 **Laidlaw, D.H.,** Fleischer, K.W., Barr, A.H., 1998. Partial-Volume Baysian Classification of Material Mixtures in MR Volume Data Using Voxel Histograms. IEEE Transactions on Medical Imaging. Feb 17(1), 74-86.

8 **McLachlan, G.J.,** Krishnan, T., 1997. The EM Algorithm and Extensions. Wiley Series in Probability and Statistics; John Wiley Sons, London.

9 **Mitchel, P.,** Ellison, D.W., Mendelow, A.D., 2005. Sugery for malignant gliomas: mechanistic reasoning and slippery statistics. Lancet Neurol. Jul 4(7), 413-422.

10 **Noe, A.,** Gee, J.C., 2001. Partial Volume Segmentation of Cerebral MRI Scan with Mixture Model Clustering. Information Processing in Medical Imaging: 17th International Conference. LNCS 2082, Springer-Verlag Heidelberg, 423-430.

11 **Price, S.J.,** Burnet, N.G., Donovan, T., Green, H.A., Pena, A., Antoun, N.M., Pickard, J.D., Carpenter, T.A., Gillard, J.H., 2003. Diffusion tensor imaging of brain tumours at 3T: a potential tool for assessing white matter tract invasion? Clin Radiol. Jun 58(6), 455-462.

12 **Price, S.J.,** Pena, A., Burnet, N.G., Jena, R., Green, H.A., Carpenter, T.A., Pickard, J.D., Gillard, J.H., 2004. Tissue signature characterisation of diffusion tensor abnormalities in cerebral gliomas. Eur Radiol. Oct 14(10), 1909-1917.

13 **Provenzale, J.M.,** McGraw, P., Mhatre, P., Guo, A.C., Delong, D., 2004. Peritumoral brain regions in gliomas and meningiomas: investigation with isotropic diffusion-

ON CONNECTIVITY IN THE CENTRAL NERVOUS SYSTEM — A MAGNETIC RESONANCE IMAGING STUDY

DIFFUSION TENSOR IMAGING IN PRIMARY BRAIN TUMORS: REPRODUCIBLE QUANTITATIVE ANALYSIS OF CORPUS CALLOSUM INFILTRATION AND CONTRALATERAL INVOLVEMENT USING A PROBABILISTIC MIXTURE MODEL

weighted MR imaging and diffusion-tensor MR imaging. Radiology Aug 232(2), 451-460.

14 **Schlüter, M.,** Stieltjes, B., Rexilius, J., Hahn, H.K., Peitgen, H.-O., 2004. Unique planar color coding of fiber bundles and its application to fiber integrity quantification. IEEE International Symposium on Biomedical Imaging. Catalog Number: 04EX821C, ISBN: 0-7803-8389-3: 900-903.

15 **Schlüter, M.,** Konrad-Verse, O., Hahn, H.K., Stieltjes, B., Rexilius, J., Peitgen, H.-O., 2005. White matter lesion phantom for diffusion tensor data and its application to the assessment of fiber tracking. SPIE Conference on Medical Imaging. San Diego, CA

16 **Schlüter, M.,** Stieltjes, B., Hahn, H.K., Rexilius, J., Konrad-Verse, O., Peitgen, H.-O., 2005. Detection of Tumor Infiltration in Axonal Fiber Bundles Using Diffusion Tensor Imaging. Int J Medical Robotics and Computer Assisted Surgery 2005; 1(3): 80-86.

17 **Stejskal, E. O.,** Tanner, J. E., 1965. Spin diffusion measurements: spin-echoes in the presence of time-dependent field gradient. J. Chem. Phys. 42, 288–292.

18 **Thomas, B.,** Eyssen, M., Peeters, R., Molenaers, G., Van Hecke, P., De Cock, P., Sunaert, S., 2005. Quantitative diffusion tensor imaging in cerebral palsy due to periventricular white matter injury. Brain Jul 27; (Epub ahead of print)

19 **Tropine, A.,** Vucurevic, G., Delani, P., Boor, S., Hopf, N., Bohl, J., Stoeter, P., 2004. Contribution of diffusion tensor imaging to delineation of gliomas and glioblastomas. J Magn Reson Imaging. 20(6), 905-912.

20 **Zlatescu, M.C.,** TehraniYazdi, A., Sasaki, H., Megyesi, J.F., Betensky, R.A., Louis, D.N., Cairncross, J.G., 2001. Tumor location and growth pattern correlate with genetic signature in oligodendroglial neoplasms. Cancer Res. 61(18), 6713-5.

114

— 7 —

Diffusion tensor imaging-based fractional anisotropy quantification in the corticospinal tract of patients with amyotrophic lateral sclerosis using a probabilistic mixture model

S.K. Schimrigk, B. Bellenberg, M. Schlüter, B. Stieltjes, R. Drescher, J. Rexilius, C. Lukas, H.K. Hahn, H. Przuntek, O. Köster

In amyotrophic lateral sclerosis (ALS), fiber degeneration within the corticospinal tract (CST) can be quantified by diffusion tensor imaging (DTI) as an indirect marker of upper motor neuron involvement. A new method of measuring quantitative DTI parameters using a probabilistic mixture model for fiber tissue and background in the corticospinal tract of patients with ALS is evaluated. Axial echo-planar imaging (EPI) DTI datasets (6 gradient directions, 10 repetitions) were acquired for 10 patients and 20 healthy control subjects. The diffusion tensor was visualized in a multiplanar viewer using a unique color coding method. Pure fiber tissue inside a region is separated from background and mixture voxels using a probabilistic mixture model. This allows for a reduction of errors as a result of partial volume effects and measurement variability. Fractional anisotropy (FA) was measured within the CST at levels ranging from internal capsule to pons. Mean coefficients of variation of intrarater, scan-rescan, and inter-rater reproducibility were 2.4%, 3.0%, and 5.7%, respectively. Optimal measurement positions along the CST with respect to minimum variability and maximum difference between patients and healthy subjects were identified in the caudal half of the internal capsule. Moreover, a negative correlation between the age-corrected FA and the disease duration but not the ALS Severity scale score was found. The new software for fiber integrity quantification is suited to assess FA in the corticospinal tract with high reproducibility. Thus, this tool can be useful in future studies for monitoring disease status and potential treatment efficiency.

Introduction

Amyotrophic lateral sclerosis (ALS) is a devastating and in many cases rapidly progressive neurodegenerative disease for which there is currently no effective treatment. In the classic type of ALS, both the upper motor neurons (UMN) and lower motor neurons (LMN) are affected. Diffusion tensor imaging (DTI) is an MR imaging technique that can detect and quantify degeneration of nerve fibers. In recent years, DTI has increasingly been used as a potential quantitative measure of UMN involvement. In ALS, damage to fibers of the corticospinal tract (CST) occurs secondary to UMN destruction. The CST connects, as a major white matter tract, the cerebral motor cortex with the spinal cord. Its fibers between internal capsule and pons form acompact bundle that can be assessed by DTI. Detection of abnormalities within the CST by conventionalMRimaging is limited.[1,2] In contrast, DTI provides an objective quantitative marker of water diffusion within living tissue and represents a surrogate marker for active neuronal degeneration. Refining the method of DTI evaluation may improve our ability to confirm early ALS diagnosis, monitor the course of the disease, and particularly evaluate new therapeutic approaches.

DTI

In DTI-MR images image contrast is modulated by the stochastic movement of water molecules within tissue. Cellular barriers found in highly directionally ordered structures, such as nerve fibers, result in anisotropic water diffusion. This directional dependence of diffusion properties can be described by tensor mathematics. The diffusion tensor is assessed by diffusion-weighted MR imaging.[3] Fractional anisotropy (FA) is a measure of the degree of directionality of diffusion. Its values range from 0 (no directional dependence of the diffusion) to 1 (diffusion along a single direction).

Since the fundamental studies of Ellis et al,[4] patients with ALS have been increasingly subjected to DTI measurements. Especially in the posterior limb of the internal capsule (PLIC), a disease-related reduction of FA has been found in several studies.[1,4-7]

A New DTI Quantification Model

Significant differences between the absolute FA values can be found in groups of age-matched healthy control subjects in several studies.[1,4,5,8] This reflects the variety of the procedures of data acquisition, postprocessing, and data analysis and superimposes the biologic variability of FA. Until now, there has been no standard DTI analysis. Most current studies use region of interest (ROI) approaches for FA quantification, which often include manual ROI delineation in combination with coregistered anatomic MR imaging series. These procedures are vulnerable to mismatch problems, partial volume errors by non-CST contaminations, and interobserver differences. The clinical relevance of quantifying the precision of DTI measures has been emphasized by several authors and was assessed for the corpus callosum and recently for the hippocampus.[9,10] To our knowledge, the reliability of the current methods of FA quantification in the CST has not yet been described.

In this study, we used a probabilistic mixture model that allowed robust assessment of DTI data. The details of the model have been described in recent publications.[11,12] In brief, voxels inside a ROI surrounding the investigated fiber bundle are classified as belonging to:

1 pure fiber,

2 pure background, or

3 a partial volume class that is a mixture of fiber and background. As has been shown recently in the corpus callosum, this procedure makes the results largely independent of observer-specific choices of the ROI.[13] In this study, we quantified the fiber integrity at different locations of the corticospinal tract of patients with ALS and healthy control subjects. The aim was to assess the reproducibility of FA and to optimize the analysis with respect to the measurement location.

Materials and Methods

Subjects

Ten patients (4 women, 6 men) aged from 36 to 76 years (mean/SD, 55/13 years) were classified according to the El Escorial Criteria[14] as having clinically definite ALS. They were staged using the ALS Severity (ALSS) scale,[15] ranging from 0 to 40 points; 40 points means the best clinical outcome. The subscales (each with 1 to 10 points) include speech, swallowing, lower extremities (walking), and upper extremities (dressing and hygiene). The scale is fast and reliable and is optimized for assessment of disease severity. The patients ranged between ALSS 16 and 34 (mean/SD, 28/5). The disease duration was 12 to 60 months (mean/SD, 30/19).

Twenty control subjects (9 women, 11 men) were free of chronic or acute neurologic or psychiatric diseases. They had no regular drug intake, and a standard neurologic examination revealed regular findings in all. The age range was 26–76 years (mean/SD, 48/16).

All study subjects had no contraindications for MR imaging and received the same measurement protocol. Written informed consent to participate in the study was obtained from all participants, and the local institutional review board approved the study.

Clinical examinations and enrollment of study subjects was done by an experienced senior neurologist. Data analysis and evaluation was performed by 3 experienced raters: a senior radiologist, a medical physicist, and a senior neurologist.

MR Imaging Protocol and Data Processing

MR imaging data were acquired on a 1.5T MR system with 30 mT/m maximum gradient strength using a quadrature head coil. Involuntary head movement was limited by lateral fixation. DTI was performed using a single-shot 2D EPI sequence (TR, 8500 ms; TE, 109 ms; section thickness, 2.5 mm; matrix, 128 x 128; resolution, 2.5 x 2.5 mm; acquisition time, 1 minute 10 seconds) resulting in

ON CONNECTIVITY IN THE CENTRAL NERVOUS SYSTEM — A MAGNETIC RESONANCE IMAGING STUDY

DIFFUSION TENSOR IMAGING-BASED FRACTIONAL ANISOTROPY QUANTIFICATION IN THE CORTICOSPINAL TRACT OF PATIENTS WITH AMYOTROPHIC LATERAL SCLEROSIS USING A PROBABILISTIC MIXTURE MODEL

1 image without and 6 with diffusion weighting (b = 1000 s/mm^2) in distinct non coplanar gradient directions. Forty-seven contiguous axial sections were acquired to cover the whole brain down to the brain stem. All subjects received additional anatomic imaging according to a standardized MR imaging protocol that provided standardized positioning and control for image quality and abnormalities.

To increase signal-to-noise ratio (SNR) in the diffusion tensor images, data acquisition was repeated 10 times. Image quality was checked by calculation of the SNR in single non averaged DTI datasets with b = 0. Furthermore, images were evaluated visually to exclude images with large distortion or ghosting. MR images were processed, visualized, and analyzed with software modules implemented in MeVisLab (MeVis, Bremen, Germany). The repeated DTI datasets were resampled to a matrix of 1.25 mm isotropic resolution, spatially matched, and averaged. The diffusion tensor was reconstructed from the resulting DTI dataset as described by Schlüter et al.[11]

DTI Parameter Quantification with the New Model

To separate neighboring fibers, we used the optimal color coding method, which has been described elsewhere.[11, 12] This method assigns the main principal eigenvector directions of the voxels in a complete image or a predefined region to a color scale. Local ambiguity of the coding is minimized by an automatic optimization of the projection plane. It can be used iteratively from large to smaller ROI to separate different projectional fibers. In detail, the process of DTI quantification is as follows.

In a first step, the color-coded DTI dataset is displayed in a 3D viewer, where an evaluation plane can be chosen at arbitrary levels orthogonal to the CST (figure 1). Optimal color coding within the PLIC leads to a visually well detectable color (red) of the central part that is clearly different from the colors of the surrounding fibers. Thus, the central part of the PLIC can be well delineated by a smaller ROI for further classification (figure 2). In the more caudal evaluation planes within the CST, no different
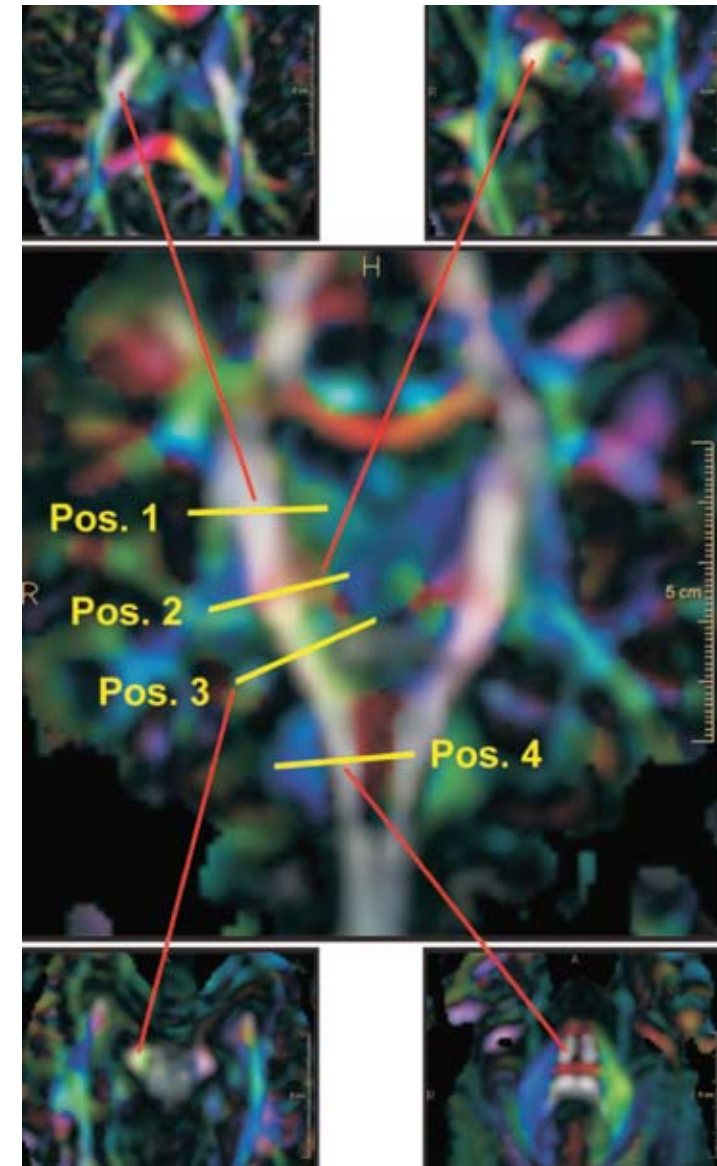
Figure 1 Definition of the evaluation planes along the CST. Coronal view depicts the definition of positions 1 to 4. Axial views show the corresponding reformatted sections. The end points of the red lines correspond to the right CST location within the axial sections.

ON CONNECTIVITY IN THE CENTRAL NERVOUS SYSTEM — A MAGNETIC RESONANCE IMAGING STUDY

DIFFUSION TENSOR IMAGING-BASED FRACTIONAL ANISOTROPY QUANTIFICATION IN THE CORTICOSPINAL TRACT OF PATIENTS WITH AMYOTROPHIC LATERAL SCLEROSIS USING A PROBABILISTIC MIXTURE MODEL
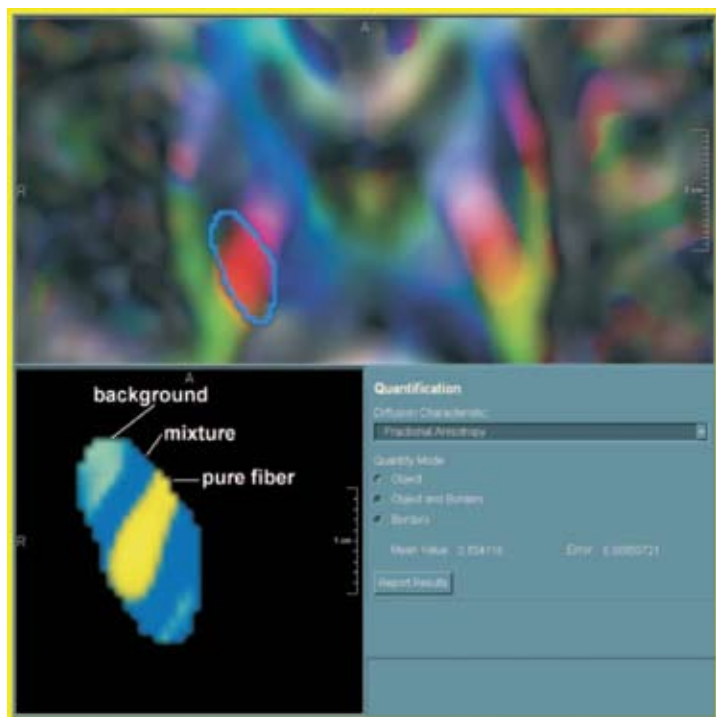
Figure 2 FA quantification procedure. Optimal color-coding in the right branch of the CST at the level of the internal capsule. Top, ROI delineation with fiber bundles of interest (red) and the bordering fibers (green, blue). Bottom left, probability map of ROI; yellow, light green, and blue area voxels belong to fiber, background, or mixture tissue, respectively.

projectional fibers with similar main direction could be identified.

In a second step, a ROI is placed that coarsely circumscribes the voxels containing the selected fiber tissue plus the surrounding background voxels. The probabilistic mixture model is applied to the voxels inside the ROI. Partial volume effects are explicitly modeled by a uniformly distributed mixture of the 2 pure tissue classes ("fiber" and "nonfiber"). The model parameters are adapted to the ROI histogram of the diffusion anisotropy by a maximum likelihood mixture model clustering algorithm.[16,13] After clustering inside the fiber of interest, arbitrary combinations of the eigenvalues of the diffusion tensor (eg, FA or other quantitative DTI parameters) can be calculated.

Figure 2 shows the quantification procedure at the PLIC, including optimal color coding, ROI delineation, and clustering. In our study, FA in a specific ROI was calculated as the mean value in the "pure fiber" class (yellow). The total postprocessing time for quantification of FA at a specific level of the CST was less than 2 minutes.

ROI Positioning along the CST

The path of the CST was identified on the DTI colormapwith evaluation planes chosen orthogonal to the main fiber direction at different levels of the left and right branch. The datasets were evaluated either section-by-section in 1.25 mm steps along the CST or at 4 distinct levels (figure 1). Position 1 is at the center of the internal capsule at the level of the maximal medial extension of the left and right thalamus, position 2 is at the caudal border of the internal capsule at the level of the medial bend of the CST (as can be located in the coronal view), position 3 is in the midbrain at the level of the cerebral peduncles, and position 4 is at the mid-pons level as seen in the sagittal view.

At position 1, the CST fibers were located and evaluated in the PLIC. We chose ROIs in the posterior half of the PLIC in accordance with findings of Holodny et al.[16] (figure 2). At positions 2, 3, and 4, ROIs were chosen to circumscribe all CST fiber voxels. In figure 1, the end points of the red lines correspond to the right CST location within the axial sections.

SNR

Image quality was checked by calculation of the SNR in single non averaged DTI datasets with b = 0. SNR was defined as the ratio of the mean MR image signal intensity in the posterior limb of the internal capsule to the SD of the signal intensity in a background ROI outside the brain. A SNR of at least 20 has been recommended for a reliable quantification of DTI parameters.[17]

Reproducibility of FA

The coefficients of variation (CV) of repeated measurements (intrarater, scan-rescan, inter-rater) were calculated according to the method of Bland and Altman.[18]

Intrarater Variability

The intrarater variability was assessed by 19 double measurements of FA on 1 control subject at positions along the left and right branches of the CST, ranging from the upper margin of the internal capsule down to the cerebral peduncles. The CV was calculated as the mean of the absolute differences of the data pairs divided by the mean of all FA values. The data were evaluated by 1 observer with a time interval of at least 1 week between the measurements.

Scan-Rescan Variability

To measure the scan-rescan variability, 1 normal control subject was scanned 2 times 1 week apart. The orientation of the image blocks was varied slightly to simulate the variability of realistic imaging conditions: in the first scan, the sections were aligned parallel to the lower borders of the corpus callosum; in the second scan, an orientation orthogonal to the posterior border of the brain stem was chosen. The resulting position differences between the scans were compensated by linear scaling with respect to the CST location of the pons and position 2 (figure 1). FA was evaluated by 1 observer at 23 positions along the CST ranging from internal capsule to the cerebral peduncles. Scan-rescan CV was calculated from the differences of the data pairs.

Inter-Rater Variability

The inter-rater variability was assessed by 3 independent observers on 2 healthy subjects and 2 patients with ALS. FA was measured at the typical measurement positions 1 to 4 along the CST each in 3 adjacent sections (figure 1). All combinations of data pairs at each position were analyzed, and the CVinter-rater was calculated from the differences of the data pairs in all subjects.

Optimization of the Measurement Position along the Pyramidal Tract

To optimize the evaluation position, the DTI datasets of 2 patients with ALS and 2 control subjects were evaluated in small steps of 1.25 mm along the CST, ranging from the upper border of the internal capsule to the middle of the pons. The CST was covered by 25 to 30 measurements of FA on both the left and right branches. For comparison of the courses of the quantitative DTI parameters, the data of each subject were transformed linearly to a uniform position scale with respect to the CST locations of the pons (as the origin of the scale) and position 2.

Age-Correction of the FA Results

Age dependence of the FA results of the control group was modelled by linear regression, to account for an age correction of the data. An age-correction operation was performed by linear scaling according to the linear regression of the control group on all data, assuming that the patient data were subjected to the same age dependence as the control subjects.

Analysis of Group Differences between Patients with ALS and Control Subjects

The statistical significance of the group differences between patient and control group of the age-corrected mean FA values was evaluated by unpaired t testing and by the "difference versus SD ratio" (DSR). The DSR is the ratio of the difference of the mean FA between the patient and control groups and the SD of the

control group. It is a composite measure of the significance of the measured group difference and the stability of the measurement; if 2 evaluation strategies yield the same mean intergroup difference, then the evaluation method with the lower variability should be preferred.

Corrrelation of FA with Clinical Disease Status

Because the patients with ALS in this study presented at different stages of the disease, a high intersubject FA variability had to be expected. Although it was no major aim of this study to use DTI to stage ALS, we analyzed our data for a correlation between FA and disease stage and duration. The dependence of the age-corrected FA on disease status and duration was examined by bivariate correlation analysis with the ALSS score as well as disease duration. All statistical tests were performed at the level of significance of 5% using SPSS software (ver.12; SPSS, Chicago, Ill).

Results

SNR

Signal-to-noise gain due to averaging (n=10) was considered by multiplication by (n). SNR was calculated for 10 control subjects and 10 patients and ranged from 51 to 63. This exceeds the SNR minimum of 20, which has been recommended for a reliable DTI quantification.[17]

Reproducibility of FA Quantification

Intrarater, scan-rescan, and interrater reproducibilies of the FA measurements are shown in Table 1 by the CV, the mean variability, and mean values of FA. Regarding intrarater and scan-rescan reproducibility, the values were calculated for the mean of all measurements at all positions along the CST. The inter-

Table 1: Intrarater, scan-rescan, and inter-rater variability of FA measurements along the CST

	Mean of All Positions			Inter-Rater Variability at Different Positions along the CST			
	Intrarater	Scan-Rescan	Inter-rater	1	2	3	4
CV	2.4%	3.0%	5.7%	4.5%	4.6%	7.9%	6.0%
Mean value of abs. differences	0.016	0.020	0.034	0.028	0.030	0.051	0.030
FA$_{mean}$	0.67	0.66	0.602	0.619	0.658	0.642	0.492

Note:—FA indicates fractional anisotropy; CST, corticospinal tract; CV, coefficient of variation defined as mean value of absolute differences divided by FA$_{mean}$; FA$_{mean}$, mean value of FA measurements of the respective variability assessment. See Fig 1 for definition of positions 1 to 4.

Table 1

rater reproducibility was differentiated further and is presented for the mean of all positions and for the single positions 1 to 4. The CV at the positions 1 and 2 was significantly smaller than at the positions 3 and 4. This indicated that positions 1 and 2 are probably superior measurement locations for DTI quantification.

Optimization of the Measurement Position

Figure 3 shows typical courses of FA along the CST for 2 patients with ALS (triangles) and 2 healthy control subjects (circles) dependent on the normalized distance to the pons for the left and right branches of the CST. The 4 gray bars mark the different ranges, which have been identified as positions 1 to 4 in all measurements.

The gross course of FA is similar in all analyzed subjects: from the center of the internal capsule (position 1) to the midbrain (position 3), there is an increase in FA with few individual local maxima. Below position 3, there is a steep decrease of FA down to position 4. At the level of the pons (position 4), we find high variability of FA. Comparing the 2 patients with the 2 control subjects, we find good agreement of FA values at the positions 1, 2, and 3 for the healthy subjects, whereas there are differences between the patient results depending on position and side (left/right).

Thus positions 1 and 2 seem to be best suited for DTI evaluation because FA has a small increase in these ranges. Position 3, on the other hand, is not well suited because it lies within the range of steep slope of the FA curve, so that small variations in position can result in high FA changes. Position 4 also seems to be less well suited to FA quantification because of high FA variability. Based on these results, we concentrated our further evaluation
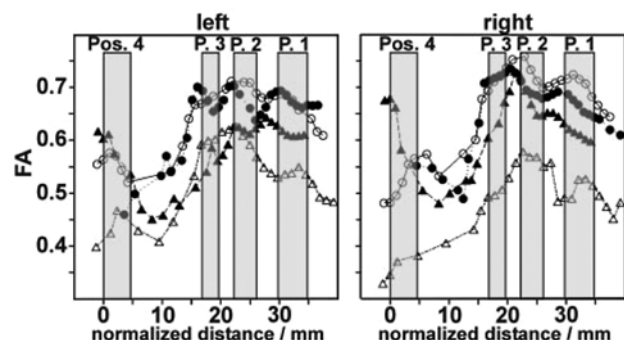
Figure 3 Individual FA courses along the CST. Circles, healthy subject 1 and healthy subject 2; triangles: patient 1 and patient 2. Gray bars mark the ranges of position 1 to 4.

on positions 1 and 2. Because FA courses still showed local maxima and minima in this range we compared the following evaluation strategies: FA mean value calculated from 3 adjacent sections:

A in position 1,

B in position 2,

C in the middle position between positions 1 and 2, and

D within the range between positions 1 and 2.

Patient and Control Data

Optimal Evaluation Strategy under Consideration of the Age Dependence of FA

We studied FA results by all 4 evaluation methods regarding age dependency. Figure 4 shows the scatter plots of FA versus age, including the linear regression lines of the control group.

The FA values of the control subjects showed an age-dependent decrease of -0.10% - 0.21% per year (evaluation method A, -0.11%; B, -0.21%; C, -0.17%; D, -0.10%). We found no sex-specific differences within the results of the control subject group (data not shown.). The inter-individual variability of FA in the control group was considerably lower when using evaluation method C than with the other evaluation strategies. The +/- 95% confidence range of the regression was 0.03 in C compared with 0.06 (A), 0.07 (B), and
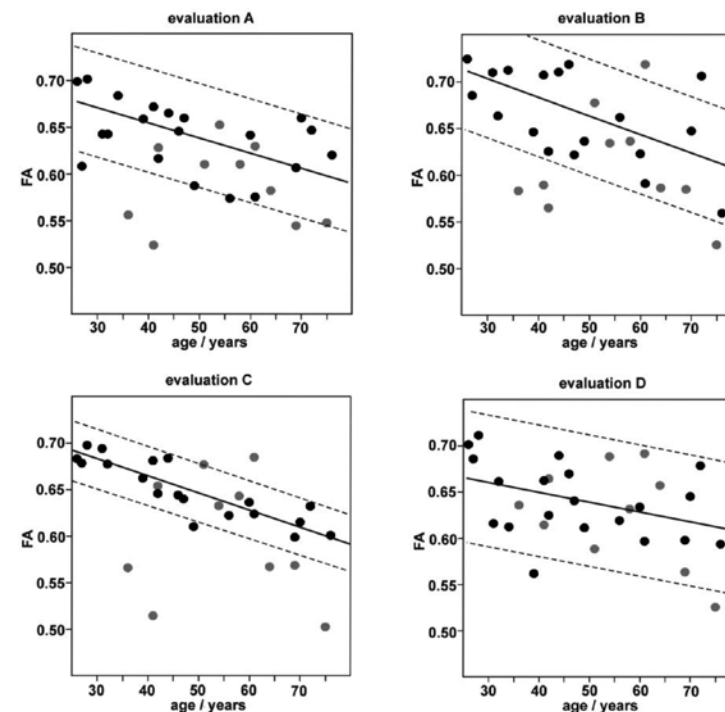
Figure 4 FA as measured using evaluation strategies. A, B, C, and D are dependent on subject age. Mean values of corresponding measurements in the left and right branch of the CST. Black circles, control group. Gray circles, patients with ALS. Lines, linear regression of the control group with 95% confidence range.

0.08 (D) respectively. Thus, from the point of view of maximal stability of measurement results, evaluation strategy C (ie, FA measurement at the center between positions 1 and 2) seems to be optimal for quantification of FA in the CST.

In the patient group, because of the variability of disease induced effects, the range of measured FA values was generally broader than in the group of healthy control subjects. The quality of discrimination between the patient group and the control group gained by the different evaluation strategies was further evaluated by examining the age-corrected data. In Table 2, the age-corrected mean FA values and SDs of the patient and control groups were compared for the different evaluation strategies.

Table 2: Age-corrected mean FA for patient and control groups by different evaluation strategies

	Group	Evaluation Strategy			
		A	B	C	D
FA$_{mean}$	Patients ($n = 10$)	0.644 ± 0.049	0.728 ± 0.075	0.693 ± 0.076	0.672 ± 0.064
(Age corrected) ± SD	Control subjects ($n = 20$)	0.694 ± 0.045	0.770 ± 0.048	0.732 ± 0.020	0.691 ± 0.045
Significance of group difference		$P = .001$	$P = .011$	$P = .004$	$P = .162$
DSR		1.12	0.86	1.96	0.43

Note:—FA indicates fractional anisotropy; FA$_{mean}$, mean value of FA measurements of the respective variability assessment; DSR, difference vs SD ratio.

Table 2

The statistical significance of the group differences and the DSR were also denoted. Although the group differences gained by evaluation strategies A and C were both highly significant, strategy A showed the most significant differences. However, the DSR was clearly highest when using strategy C, because of the very low variability of FA results in the control group. Although evaluation strategy B also led to significant group differences, the results were less satisfactory because of the high SD of the control group results. Strategy D yielded no significant difference between the patient group and the control group.

In summary, the evaluation strategies A and C (ie, FA measurement at position 1 and at the center between positions 1 and 2, respectively) both seem well suited to monitor diseaserelated changes in FA in the CST of patients with ALS. Whether the more prominent FA differences between patients and control subjects (strategy A) or the superior stability of the FA measurements as in strategy C are advantageous in clinical studies cannot be decided at this point.

Correlation between fa and Clinical Parameters after Age Correction of the Data

We used evaluation strategies A and C for FA quantification and corrected for age as described above. Bivariate correlation analysis between the age-corrected FA and the ALSS score as well as the disease duration revealed a significant correlation between FA and the disease duration for both evaluation strategies (P=.011 and P=.010 strategy A and C, respectively) with the Pearson correlation coefficient r = -0.543 and - 0.589, respectively. In contrast no significant correlations between FA and the ALSS score (P = .79 and P = .68, respectively) were found.

Discussion

DTI assessment of fiber integrity in the CST of patients with ALS has the potential to give valuable quantitative information about the involvement of UMN in this disease. Most current methods use an ROI-based approach, whereas the fiber containing areas are identified on coregistered anatomic MR imaging series.[1, 4, 5, 8, 10, 19] This is a time-consuming process that is subject to measurement errors and partial volume effects as a result of the small fiber calibers and usually poor image resolution of the DTI series.

The probabilistic mixture model for DTI quantification used in this study[11, 13] is applied directly on the DTI dataset. The optimal planar color-coding scheme of the DTI-based color maps visualizes small differences in fiber directionality even where different fiber bundles lie directly adjacent to each other. The mixture model uses an automatic classification of voxels inside an ROI as fiber, nonfiber, or mixture. The complete procedure of FA quantification at a selected location takes less than 2 minutes.

In the present study, the probabilistic mixture model was evaluated in the CST. To our knowledge, this is the first study in which the reproducibility of a DTI quantification method on the CST has been investigated. The high stability and reproducibility of FA assessment by the model was shown. The inter-rater reproducibility of FA measurement at single selected levels ranged from 4.5% (PLIC) to 7.9% (midbrain), which corresponds to an absolute FA variability of +/- 0.028 to +/- 0.051 respectively. This variability represents the sensitivity limit for the detection of FA changes within the CST in a realistic clinical setting with several evaluators. For a valuable application as a diagnostic tool, it is certainly important that DTI can monitor early ALS effects. So far, however, there is only very limited information about FA decrease rates in the longitudinal course of ALS.[6] Further longitudinal studies with a larger number of patients are necessary before the suitability of DTI quantification methods for early disease monitoring of ALS can be sufficiently evaluated.

We found the course of FA, from the PLIC through the cerebral peduncles to the pons, is in accordance with that reported for other studies.[2, 5, 19] High FA values as found in the PLIC are

130

131

ON CONNECTIVITY IN THE CENTRAL NERVOUS SYSTEM — A MAGNETIC RESONANCE IMAGING STUDY

DIFFUSION TENSOR IMAGING-BASED FRACTIONAL ANISOTROPY QUANTIFICATION IN THE CORTICOSPINAL TRACT OF PATIENTS WITH AMYOTROPHIC LATERAL SCLEROSIS USING A PROBABILISTIC MIXTURE MODEL

interpreted to result from coherent, tightly packed fibers. Below the cerebral peduncles, many fibers leave the CST, leading to an FA decrease. At the level of the pons, the CST splits into multiple smaller bundles, which results in increased measurement variability, as we have found in the pons.[20]

Our optimization of the measurement location showed that FA should be quantified at the level of the caudal half of the PLIC. This region is probably characterized by an especially high CST fiber density. The result corresponds well to a recent study by Abe et al,[7] who located significant group differences between patients with ALS and control subjects in the caudal part of the PLIC by voxel-based morphology. Measurements at the center of the internal capsule (strategy A) and at the caudal border of the internal capsule (strategy C) were clearly superior to the other evaluation strategies, whereas strategy C had the best reproducibility of FA measurement. The 2 superior measurement positions are defined by 2 anatomically well defined locations of the CST (figure 1). They can be located precisely and are thus methodologically suited for intersubject comparisons and longitudinal studies.

The control group data revealed a considerable linear decrease of FA with increasing age (-0.11% per year for A and -0.17% per year for C), which has to be taken into account when results are classified as normal or abnormal. This age dependence has also been described in a study by Salat et al,[20] who reported an FA decrease of -0.2% per year within the PLIC. The normal FA values decrease from FA = 0.70/0.67 (evaluation strategies C/A) at the age of 20 years to FA = 0.60/0.61 at 80 years, with a variability of +/- 0.03/+/- 0.06. Disregarding the subject's age, FA values below 0.57/0.55 (evaluation strategies C and A) can be classified as abnormal.

Our preliminary analysis revealed a significant correlation between the age-corrected FA results and the duration of the disease but not the ALSS score. In general, this agrees with other studies in which a disease-related FA decrease within the PLIC has been described.[1, 4, 5, 6] Regarding the correlation between the DTI parameters and clinical disability scores, there are inconsistent results in the different studies in literature. There are several possible explanations for the lack of correlation between the

disease status and FA in this study: the ALSS score is estimated by several clinical findings, including LMN signs, and may be relatively unspecific for CST involvement. ALS-related pathology in the CST can be heterogeneous in grade and location,[2, 8] such that a larger patient population is a prerequisite for statistically significant results.

There are other methodologic study limitations: small calibre fibers cannot be quantified reliably by the method because dominant partial volume effects prevent the classification of "pure-fiber" voxels. Acquisitions with a higher image resolution could reduce this effect. Different projectional fibers with the same FA and direction that lie adjacent to each other cannot be distinguished by the optimal color-coding method. In such structures as the brain stem, which is transversed by numerous major motor and sensory white matter fibers, this can affect the reliability of DTI quantification.

Conclusion

The probabilistic mixture model is well suited for DTI quantification in the CST. The processing time is relatively low, and its high reproducibility and stability have been shown. It is an important future challenge to develop uniform standards of evaluation in the growing field of clinical DTI applications to allow for multi-center comparisons. In particular, the need for highly reproducible and robust quantification procedures will emerge should effective treatment options for ALS be found. In this study, we have established a valuable basis for further DTI studies in the CST on a larger number of patients with motor neuron diseases such as ALS.

References

1   **Graham JM,** Papadakis N, Evans J, et al. Diffusion tensor imaging for the assessment of upper motor neuron integrity in ALS. Neurology 2004;63:2111–19

2   **Wang S,** Melhem ER. Amyotrophic lateral sclerosis and primary lateral sclerosis: the role of diffusion tensor imaging and other advanced MRbased techniques as upper motor neuron markers. Ann NY Acad Sci 2005;1064:61–77

3   **Basser PF,** Pierpaoli C. Microstructural and physiological features of tissue elucidated by quantitative diffusion-tensor MRI. J Magn Reson B 1996; 111:209–19

4   **Ellis CM,** Simmons A, Jones DK, et al. Diffusion tensor MRI assesses corticospinal tract damage in ALS. Neurology 1999;53:1051–58

5   **Toosy AT,** Werring DJ, Orrell RW, et al. Diffusion tensor imaging detects corticospinal tract involvement at multiple levels in amyotrophic lateral sclerosis. J Neurol Neurosurg Psychiatry 2003;74:1250–57

6   **Jacob S,** Finsterbusch J, Weishaupt JH, et al. Diffusion tensor imaging for longterm follow-up of corticospinal tract degeneration in amyotrophic lateral sclerosis. Neuroradiology 2003;45:598–600

7   **Abe O,** Yamada H, Masutani Y, et al. Amyotrophic lateral sclerosis: diffusion tensor tractography and voxel based analysis. NMR Biomed 2004;17:411–16

8   **Cosottini M,** Giannelli M, Siciliano G, et al. Diffusion-tensor MR imaging of corticospinal tract in amyotrophic lateral sclerosis and progressive muscular atrophy. Radiology 2005;237:258–64

9   **Pfefferbaum A,** Adalsteinsson E, Sullivan EV. Replicability of diffusion tensor imaging measurements of fractional anisotropy and trace in brain. J Magn Reson Imaging 2003;18:427–33

10 **Müller MJ,** Mazanek M, Weibrich C, et al. Distribution characteristics, reproducibility, and precision of region of interest-based hippocampal diffusion tensor imaging measures. AJNR Am J Neuroradiol 2006;27:440–46

11 **Schlüter M,** Stieltjes B, Rexilius J, et al. Unique planar color coding of fiber bundles and its application to fiber integrity quantification. IEEE International Symposium on Biomedical Imaging; 2004 Apr 15–18; Arlington.

12 **Schlüter M,** Stieltjes B, Hahn HK, et al. Detection of tumor infiltration in axonal fiber bundles using diffusion tensor imaging. Int J Med Robot Comp Assist Surg 2005;1:80–86

13 **Stieltjes B,** Schlüter M, Didinger B, et al. Diffusion tensor imaging in primarybrain tumors: reproducible quantitative analysis of corpus callosum infiltration and contralateral involvement using a probabilistic mixture model. Neuroimage 2006;31:531–42

14 **Brooks BR,** Miller RG, Swash M, et al. World Federation of Neurology ResearchGrouponMotor Neuron Diseases. El Escorial revisited: revised criteria for the diagnosis of amyotrophic lateral sclerosis. Amyotroph Lateral Scler Other Motor Neuron Disord 2000;5:293–99

15 **Hillel AD,** Miller RM, Yorkston K, et al. Amyotrophic lateral sclerosis severity scale. Neuroepidemiology 1989;8:142–50

16 **Holodny AI,** Gor DM, Watts R, et al. Diffusion-tensor MR tractography of somatotopic organization of corticospinal tracts in the internal capsule: initial anatomic results in contradistinction to prior reports. Radiology 2005;234:649–53

17 **Hunsche S,** Moseley ME, Stoeter P, et al. Diffusion-tensor MR imaging at 1.5 and 3.0 T: initial observations. Radiology 2001;221:550–56

18 **Bland JM,** Altman DG Statistical methods for assessing agreement between two methods of clinical measurement. Lancet 1986;8:1(8476):307–10

19 **Stieltjes B,** Kaufmann WE, van Zijl PC, et al. Diffusion tensor imaging and axonal tracking in the human brainstem. Neuroimage 2001;14:723–35

20 **Salat DH,** Tuch DS, Greve DN, et al. Age-related alterations in white matter microstructure measured by diffusion tensor imaging. Neurobiol Aging 2005;26:1215–27

ON CONNECTIVITY IN THE CENTRAL NERVOUS SYSTEM — A MAGNETIC RESONANCE IMAGING STUDY

DIFFUSION TENSOR IMAGING-BASED FRACTIONAL ANISOTROPY QUANTIFICATION IN THE CORTICOSPINAL TRACT OF PATIENTS WITH AMYOTROPHIC LATERAL SCLEROSIS USING A PROBABILISTIC MIXTURE MODEL

— 8 —

Reproducible evaluation of spinal cord DTI using an optimized inner volume sequence in combination with probabilistic ROI analysis

F. Laun, B. Stieltjes, M. Schlüter, R. Rupp, L.R. Schad

The purpose of this work was to reliably acquire and evaluate diffusion tensor data of the cervical spine. We describe an optimized, time-efficient inner-volume echo planar imaging sequence. Multislice capability is achieved by restoring the magnetization in neighbouring slices early during the twice refocused diffusion preparation. The acquired diffusion images showed compelling image quality. Using a probabilistic ROI-analysis, evaluation of FA and ADC values was stable and the standard deviation of five measurements was below 4.5% for each value. Absolute FA values of a healthy subject were 0.66 ± 0.02 at C2 and in the range of 0.57 ± 0.03 to 0.61 ± 0.03 at the other vertebraes. Absolute ADC-values ranged from 1.14 ± 0.04 μm^2/ms at C1 to 1.37 ± 0.05 μm^2/ms at C5. The FA values of a patient with acute ischemic spinal trauma were significantly lower. Here, absolute values ranged from 0.36 to 0.42, showing that DTI may serve as surrogate marker for tissue integrity.

Introduction

Diffusion tensor imaging (DTI) is a versatile imaging technique which can reveal structural integrity and directional information of neuronal tissue. It is used in clinical routine for stroke diagnosis[1] and its potential clinical value is under evaluation for neurodegenerative diseases[2,3] and for the evaluation of brain tumor infiltration[4]. Methods for performing brain DTI are relatively well established, but DTI of the spinal cord is still challenging due to the required high resolution, the susceptibility differences of the involved tissues, and the pulsation of the surrounding CSF. The development of a robust, reproducible assessment of spinal cord fiber integrity is of great clinical interest in neurodegenerative diseases like Multiple Sclerosis or spinal cord injury.

Several methods for improved DTI acquisition have been proposed recently. Multishot techniques allow high resolutions but are sensitive to motion-induced phase instabilities. These phase instabilities can be corrected considerably in post-processing schemes using navigator echoes[5,6]. Line scan imaging is a multishot technique which overcomes the aforementioned phase problem at cost of time efficiency[7,8]. Nonetheless, single shot techniques are preferable since they 'freeze' motion and are inherently insensitive to motion-induced phase instabilities. Single shot Echo-Planar Imaging (EPI) is commonly used since it is fast, signal to noise efficient and unlike turbo spin echo sequences, not limited by SAR thresholds. The drawback of EPI is its sensitivity to field inhomogeneity, especially when long readout trains are used. Readout trains can be shorten by using parallel imaging[9,10], partial Fourier acquisition and inner volume (IV) techniques[11]. While parallel imaging and partial Fourier acquisition are commonly available on clinical scanners, IV-techniques are usually in house developments. Wheeler-Kingshott et al.[12,13] introduced the ZOOM – EPI technique which is favourable for axial image acquisition although it is not possible to acquire contiguous slices for sagittal images. To overcome this problem, Jeong et al.[14] proposed an IV-technique that has multislice capability since it restores magnetization after the readout train. In a later work, Jeong et al.[15] proposed a more efficient strategy to restore the

magnetization, however they employed stimulated echoes image for image acquisition. Here, we propose an efficient alternative strategy for multislice IV-imaging by incorporating the magnetization restoration in the diffusion preparation.

Apart from optimal acquisition schemes, the reproducible evaluation of DTI-derived measures is critical if one aims at using DTI for clinical evaluation. The acquired diffusion data is typically post processed using hand drawn specified regions of interest (ROIs). Especially in small structures like the spinal cord, slight shifts in ROI will lead to large, user induced variations and will hamper clinical application where differences between healthy and affected tissue may be minimimal. We have recently presented a method for fast, reproducible ROI-analysis of DTI-derived parameters in the human brain[16]. Here, we evaluate this probabilistic tissue classification algorithm on DTI data of the cervical spine.

Materials and methods

MRI Sequence Description

Figure 1 a shows the timing table of the sequence. Diffusion weighting is achieved by a twice-refocused spin echo diffusion preparation[17].

The 90° RF-excitation pulse is applied in slice-selection direction and the first 180° refocusing pulse is applied in phase-encoded direction to limit field of view (FOV). The second 180° pulse is applied globally instead of in phase-encoded direction to reduce ghosting artefacts. The two 180° refocusing pulses are separated by a time τ. The signal is acquired with a standard EPI readout train and is phase corrected by three gradient echoes which are acquired after the 90° excitation pulse.

Figure 1 b shows the RF pulses in the imaged slice and the surrounding volume during the imaging process. There are three separate regions. Region I lies in the same plane as the FOV and experiences only the 90° excitation pulse. The signal decays on a T2* time scale, is spoiled by the blips of the refocusing pulses, and is negligible during the EPI readout. In region II, all three RF pulses are applied and here a spin echo is generated at time TE. The FOV
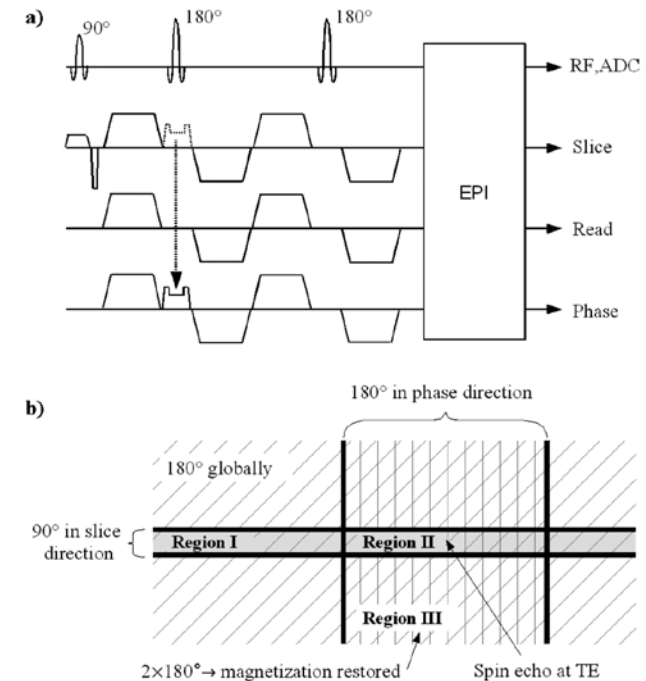
Figure 1 a) Timing table of the proposed sequence. The first 180° pulse is applied in phase-encoded direction to limit FOV. The second 180° pulse is applied globally to restore longitudinal magnetization and to enable multislice acquisition. b) Principle of the multislice enabled inner volume DTI sequence. The FOV lies in region II which is the only region experiencing a spin echo at time TE. Magnetization in region III is restored to allow multslice acquisition. The transversal magnetization of spins in region I decays on a T2* timescale and is spoiled by the gradient blips of the slice selection gradient.

of the next imaging slice shifts towards region III. Spins in region III experience two 180° refocusing pulses so that the inverted magnetization is restored. Nonetheless, a part of the magnetization is lost since the inverted longitudinal magnetization MZ decays on a T1 time scale as described by the Bloch equation[18]

$$M_z(\tau) = M_0 - (M_0 - M_z(0))e^{-\tau/T_1}$$

where M$_0$ is the equilibrium magnetization. Therefore, it is advantageous to minimize τ with a lower limit of TE/2.

Phantom and Subject Preparation and Measurement

To prove that the magnetization restoration during the diffusion preparation is more efficient than magnetization restoration after the EPI readout train, a water phantom doped with NiSO4 and NaCl (1.25 g NiSO4.6H2O+5 g NaCl per 1 kg water) was measured. Phantom images were acquired using three inner volume (IV) sequences:

1 A conventional IV-sequence without magnetization restoration
2 An IV-sequence with magnetization restoration by a second 180° RF pulse after the EPI readout
3 An IV-sequence with magnetization restoration during the diffusion preparation

Imaging parameters were: FOV = 128 x 128 mm^2, base resolution = 64, TE = 75 ms, slice thickness = 5 mm, 11 slices, 1 average. The effective repetition time TReff = TR/number of slices was adapted by varying TR between 1.6 and 16.0 s. The signal intensity of the phantom was determined in all measurements.

The spinal cord of one healthy subject was measured five times with IV-sequence[3]. The measurements were performed on a 3 T MRI system using an 12 channel head coil in combination with a 4 channel neck array (Magnetom TRIO, Siemens Medical Solutions, Erlangen, Germany, gradient strength = 40, 45 mT/m in xy, z direction, slew rate = 180, 220 T/m/s). Parameters were: FOV = 200 x 60 mm^2, resolution = 96 x 29, TR = 6 s, TE = 63 ms, slice thickness = 2.1 mm, 10 slices, 10 averages, b = 0, 650 s/mm^2, 6 directions gradient scheme, bandwidth = 1736 Hz/Px, partial fourier factor = 5/8, fat saturation. The total acquisition time was 7 minutes.

Also, diffusion weighted images of the spinal cord of one patient with acute ischemic spinal trauma were acquired. Parameters were identical to the subject measurement. Subject and patient measurements received the approval of our institutional review board. Written informed consent was obtained.

Image Post Processing

Post processing was conducted with NeuroQlab, (MeVis Research GmbH, Bremen, Germany). The acquired images were registered, magnitude averaged and interpolated to a resolution of 1 x 1 x 2 mm^3 using a cubic B-spline function. The tensor was estimated using a log-linear model. ROIs were placed at consecutive midsagittal positions of the spinal cord (C1 to C7) between the intervertebral discs. The voxels of each ROI were automatically classified into fiber, non fiber, and mixed class voxels using a recently described probabilistic classification method[16]. Apparent diffusion coefficient (ADC) and fractional anisotropy (FA) values were calculated only for the fiber class voxels. The mean and standard deviations were calculated from the 5 measurements. Fiber tracking was applied to the diffusion principal eigenvector field using a deflection based algorithm[19, 20]. Termination criteria was FA < 0.3. The tracking was initialized form two seed ROIs at the C1 and C5 level.

For the classification algorithm, it was assumed that the signal is composed by signal from a fiber class (f), an isotropic background class (b) and a mixture class (m). The partial volumes of these classes are denoted by π_f, π_b and π_m, such that $\pi_f + \pi_b + \pi_m = 1$. The anisotropy index $a = 1 - (\lambda_2 + \lambda_3) / (2\lambda_1)$ was used as measure for the anisotropy. Under certain conditions[4, 16], the anisotropy of the mixture class can be described by $a_m = (1 - \rho)a_f + \rho a_b$, where a_f and a_b are the anisotropy indices of fibre and background class and ρ is the mixture parameter. Let $P(a|f)$, $P(a|b)$ and $P(a|m)$ be the conditional probabilities that a is measured in fiber, background and mixture class. Then, the probability to measure a is $P(a) = \pi_f P(a|f) + \pi_b P(a|b) + \pi_m P(a|m)$. Here, $P(a|f)$ and $P(a|b)$ are modelled by Gaussian distributions with mean values m_f and m_b and variances σ_f and σ_b. Assuming that ρ is uniformly distributed, $P(a|m)$ can be modelled[21] by

$$P(a|m) = \frac{1}{\sqrt{2\pi}} \int_0^1 \frac{d\rho}{\sqrt{\rho^2\sigma_b^2 + (1-\rho)^2\sigma_f^2}} \exp\left(-\frac{((1-\rho)m_f + \rho m_b - a)^2}{2((1-\rho)^2\sigma_f^2 + \rho^2\sigma_b^2)}\right)$$

ON CONNECTIVITY IN THE CENTRAL NERVOUS SYSTEM — A MAGNETIC RESONANCE IMAGING STUDY

REPRODUCIBLE EVALUATION OF SPINAL CORD DTI USING AN OPTIMIZED INNER VOLUME SEQUENCE IN COMBINATION
WITH PROBABILISTIC ROI ANALYSIS
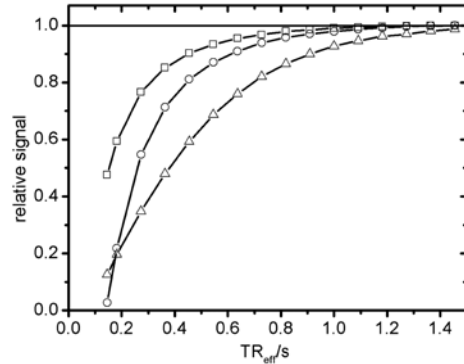
Figure 2 Relative signal intensity in the phantom versus TR$_{eff}$. Using the same TR$_{eff}$, magnetization restoration during diffusion preparation (squares) yields higher signal intensity than both the classical inner volume technique (triangles) and then magnetization restoration after the EPI readout train (circles). The magnetization is restored more efficiently because the time of inversed magnetization is reduced.

The *a*-values of all voxels within the given ROI were plotted in a histogram. Then, the free parameters were detemined using a probabilistic clustering algorithm[22]. With Bayes rule, one finds $P(f\,|\,a) = \pi_f P(f\,|\,a)\,/\,P(a)$. The expectation values for a value Q (e.g. Q = FA) of a ROI with N voxels is calculated by:

$$\langle Q \rangle = \frac{1}{N\pi_f} \sum_{x \in ROI} P(f\,|\,a_x)Q_x$$

Results

Phantom measurements

Figure 2 shows the relative signal intensity versus TR$_{eff}$=TR/number of slices for the phantom measurements.

Using the same TR$_{eff}$, the proposed magnetization restoration during the diffusion preparation (squares) yields higher signal intensity than both the conventional IV-technique (triangles) and the IV-sequence with magnetization restoration after the EPI readout train (circles). Thus, using the proposed sequence,
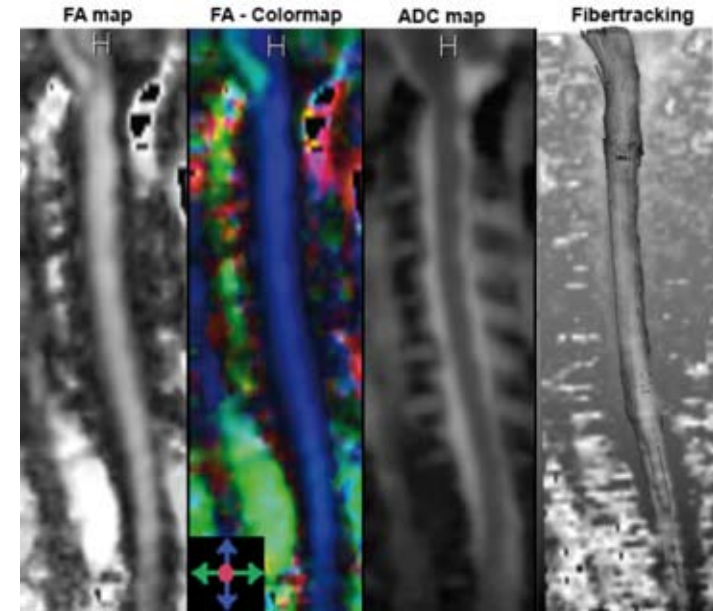
Figure 3 FA map, FA colormap, ADC map and fibertracking result.

the time of inversed magnetization is reduced and therefore, the longitudinal signal is restored more efficiently.

Probabilistic ROI-Analysis of DTI-Derived Parameters of the Spinal Cord

Figure 3 shows a FA map, a FA-colormap, an ADC map and diffusion weighted images of a mid-sagittal slice of the healthy spinal cord obtained in the subject measurements. Visually, the FA is constant over the range of the cervical spinal cord. On the colormap, the orientation of the principal eigenvector is color encoded, e.g. blue signifies a cranio-caudal orientation, the main fiber direction is represented correctly. On the ADC map, the CSF which surrounds the spinal cord is markedly more intense then the spinal cord. At height of the vertebral discs, slight image distortions are visible, but altogether, the image quality is compelling.

ON CONNECTIVITY IN THE CENTRAL NERVOUS SYSTEM — A MAGNETIC RESONANCE IMAGING STUDY

REPRODUCIBLE EVALUATION OF SPINAL CORD DTI USING AN OPTIMIZED INNER VOLUME SEQUENCE IN COMBINATION WITH PROBABILISTIC ROI ANALYSIS

Figure 4 A large ROI is exemplarily hand drawn on a mid-sagittal slice of the spinal cord including the spinal cord and CSF. Its voxels are automatically classified into fiber (yellow), non fiber (green) and mixed class (partial volume) voxels (blue).

In figure 4, a large ROI is shown exemplarily on a mid-sagittal slice of the spinal cord. Its voxels are automatically classified into fiber (yellow), non fiber (green) and mixed class (partial volume) voxels (blue). Since the ROI does not have to be drawn precisely, the evaluation process is fast and independent of the actual windowing and shape of the ROI.

Figures 5 a and 5 b show the determined FA and ADC values at different mid-sagittal positions of the spinal cord. The evaluation was stable, the standard deviation of all values was below 4.5% in the five repeated measurements. The mean FA is constant from C1 (FA = 0.61 ± 0.03) to C7 (FA = 0.57 ± 0.02). Only at C2, the mean FA is slightly increased (FA = 0.66 ± 0.02). The ADC shows a variation of 0.2 μm^2/ms between smallest and largest value. It is smallest at C1 (ADC = 1.14 ± 0.04 μm^2/ms) and largest at C5 (ADC = 1.37 ± 0.05 μm^2/ms) and decreases at lower levels of the spinal cord (ADC = 1.19 ± 0.04 μm^2/ms). The small standard deviation (below 4.5%) shows that the combination of acquisition and classification is stable and reproducible allong the complete cervical spinal cord.

Figure 6 shows a FA map, a FA colormap and an ADC map of a mid-sagittal slice of a patient with acute ischemic spinal injury. At the level of the lesion, the diffusion anisotropy vanishes. The image quality is comparable to the subject measurements and the classification is independent on ROI variation as shown before in the healthy subject measurements. Determin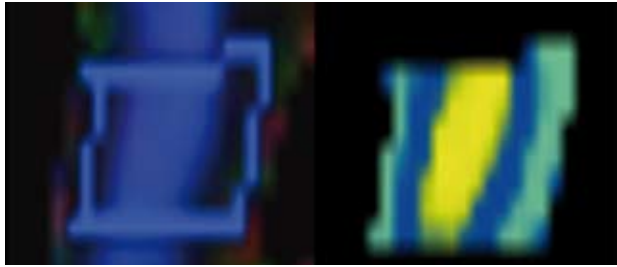ed absolute values are listed in table 1. The measured FA is markedly decreased (FA » 0.4 when compared to the healthy subject (FA » 0.6).

	C1	C2	C3	C4	C4
FA	0,384	0,335	0,367	0,424	0,370
ADC (μm²/ms)	1,219	1,385	1,222	1,233	1,1230

Table 1 FA and ADC values of the patient measurements. Compared to the healthy subject, the FA is significantly decreased, while the ADC is slightly increased.
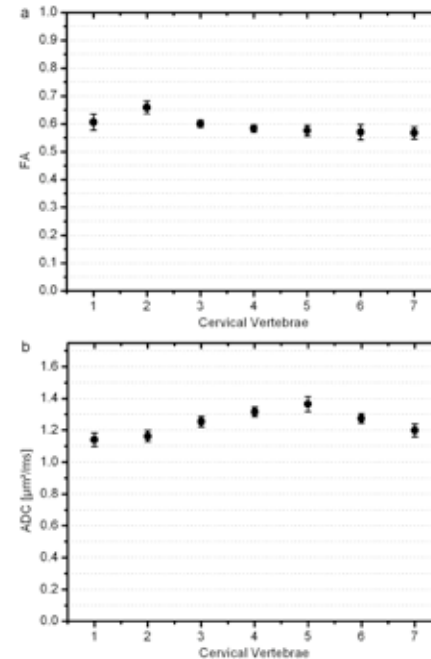
Figure 5 Measured FA (a) and ADC (b) at different mid-saggital positions of the healthy spinal cord (C1 to C7) as evaluated with the probabilistic classification approach. The mean and the standard deviation are calculated from 5 measurements. The measurement is stable, the standard deviation at all levels of the cervical spine was below 4.5%.

Discussion

The aim of this work was to develop a robust method to obtain DTI-derived parameters of the spinal cord. This is indispensable for detection of relatively small changes of spinal cord integrity

ON CONNECTIVITY IN THE CENTRAL NERVOUS SYSTEM — A MAGNETIC RESONANCE IMAGING STUDY

REPRODUCIBLE EVALUATION OF SPINAL CORD DTI USING AN OPTIMIZED INNER VOLUME SEQUENCE IN COMBINATION WITH PROBABILISTIC ROI ANALYSIS

FA map   **FA - Colormap**   **ADC map**

Figure 6 FA map, FA colormap and ADC map of a mid-sagittal slice of a patient with with acute ischemic spinal injury. The image quality is as good as in the subject measurement. The FA around the lesion is markedly decreased to about 0.4.

that may occur in disease and under therapy. The method to obtain robust parameters consists of two steps: an MR sequence which yields constant image quality needs to be developed and a post processing scheme which minimizes user-independent diffusion values should be applied.

Compared to conventional inner volume (IV) techniques and previously published IV-techniques with magnetization restoration[14], the approach proposed here is more signal-efficient and allows the usage of a twice-refocused spin echo diffusion preparation which diminishes eddy current induced image

distortions. The proposed MR imaging sequence constantly yielded compelling image quality and enabled tissue classification of the cervical spine. The slight image distortions at the level of the vertebral discs had only minor influence on the total image quality. ADC and FA evaluation was stable at the full length of the cervical spine, the evaluated FA and ADC values of the same subject varied by less than 4.5%.

As shown in previous publications[16], the tissue classification proved to be robust for a wide range of tensor shapes and initial ROI sizes, where it was successfully applied to detect small pathological changes in FA of the corpus callosum (about 15%). In the patient measurements presented here, the employed methods allowed a reliable determination of the FA. The fractional anisotropy was clearly diminished when compared to the subject measurements. Hence, the determination of the FA may be a well suited surrogate marker for tissue integrity of the spine in future studies.

The measured ADC value at the C5 level was increased by about $0.2\ \mu m^2/ms$ compared to the ADC at the C1 level. Kharbanda et al. presented data[23] indicating that CSF pulsation has a stronger influence on diffusion measurements at the lower cervical spinal cord. This can lead to an increased partial volume effect and to an additional spin dephasing in voxels with non-uniform spin velocity. The spin dephasing reduces the measured signal and increases the measured diffusion strength, which could explain the observed slight increase of ADC found in our experiments.
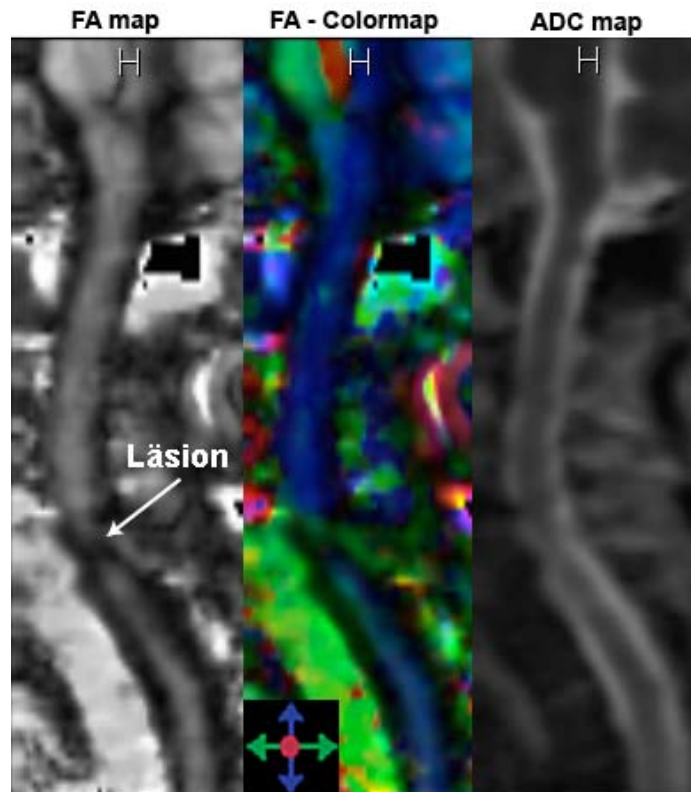
Despite the good reproducibility, the determination of the true absolute FA and ADC values is still a challenge. Partial volume effects between the spinal cord and the surrounding CSF may not only occur in plane but also in slice-selection direction. Complete CSF suppression[24] by inversion recovery could be an option for measurements with a reduced partial volume effect. However, inversion recovery was not implemented since this combination suffers from a reduced SNR efficiency. Moreover, partial volume effects also occur between grey and white matter tissue since the imaging resolution is currently at the brink of distinguishing properly between grey and white matter.

Measured FA values are well within the range reported in

148   149

ON CONNECTIVITY IN THE CENTRAL NERVOUS SYSTEM — A MAGNETIC RESONANCE IMAGING STUDY

REPRODUCIBLE EVALUATION OF SPINAL CORD DTI USING AN OPTIMIZED INNER VOLUME SEQUENCE IN COMBINATION WITH PROBABILISTIC ROI ANALYSIS

previous publications. However, there is a wide spread of reported values. E.g. Mamata et al.[25] reported FA values of 0.66 ± 0.03 to 0.70 ± 0.05, Clarke et al.[26] reported FA = 0.64, Wheeler-Kingshott reported FA = 0.55 at C1 and FA values ranging from 0.65 ± 0.03 at C2 to 0.58 ± 0.03 at C6. Ries[27] et al. measured FA values ranging from 0.65 to 1.02, with an average FA = 0.83 ± 0.11. Here, the measured FA may be larger than one if megative eigenvalues are measured due to noisy images. Bammer et al.[28] reported FA values of the WM matter of 0.60 ± 0.03 and of the GM of 0.18 ± 0.03, while Wilm et al.[29] reported FA = 0.67 ± 0.10 for the WM and 0.56 ± 0.14 for the grey matter, Rossi et al.[30] reported FA = 0.74 ± 0.04. This wide spread of reported values may reflect the effect of conventional ROI analysis with its inherent user dependence, and may also be influenced by the a wide range of employed sequence types, like EPI[28,29,30], ZOOM-EPI[13], line scan diffusion imaging[25] and fast spin echo sequences[28]. Also, the employed image resolution, signal to noise ratios, field strengths and acquisition times varied, which causes different severity of partial volume, noise bias and patient motion artefacts. Thus, care has to be taken when comparing different studies which used varying sequences and post processing schemes.

An alternative method to decrease the echo train length is parallel imaging[10]. One advantage of parallel imaging is that TR_{eff} may be chosen even shorter than with magnetization restoring inner volume imaging. Even when magnetization restoration is used, the signal intensity decreases due to the time of magnetization inversion between the 180° pulses. On the other hand, using parallel imaging, pulsation effects of surrounding tissue like the heart, the lungs and the aorta may degrade overall image quality, whereas these regions cancelled out using IV. Also, parallel imaging is not favourable when the coil sensitivity does not change significantly in phase-encoded direction and thus, with suboptimal coil design, SNR decreases due to an enlarged g-factor. For brain studies, head coils with 32 or more channels start to become available for clinical scanners. But for the cervical and the thoracal spine, acceleration factors larger than three will not be available on most clinical scanners in the coming years. Moreover, with IV, the echo train length can be shortend

more drastically and independently of the employed coil design.

In conclusion we present an optimized combination of imaging and evaluation method for spinal cord DTI. It proves to be robust over several measurements and the DTI-derived parameters are evaluated in a user independent fashion. This enables the use of DTI for evaluation of spinal cord imaging. It was shown that the measured FA of the spine in a patient with acute ischemic spinal cord injury is markedly decreased. Hence, the FA may be a surrogate marker for spinal cord function and tissue integrity. This will be evaluated further in ongoing studies.

150

151

ON CONNECTIVITY IN THE CENTRAL NERVOUS SYSTEM — A MAGNETIC RESONANCE IMAGING STUDY

REPRODUCIBLE EVALUATION OF SPINAL CORD DTI USING AN OPTIMIZED INNER VOLUME SEQUENCE IN COMBINATION WITH PROBABILISTIC ROI ANALYSIS

References

1 **Warach S,** Chien D, Li W, Ronthal M, Edelman RR. Fast Magnetic Resonance Diffusion-Weighted Imaging of Acute Human Stroke. Neurology. 1992;42:1717-1723.

2 **Horsfield M,** Jones D. Application of Diffusion-Weighted and Diffusion Tensor MRI to White Matter Diseases: a Review. NMR in Biom. 2002;15:570-577.

3 **Lim KO,** Helpern JA. Neuropsychiatric Applications of DTI - a Review. NMR in Biomedicine. 2002;15:587-593.

4 **Stieltjes B,** Schlüter M, Didinger B, Weber MA, Hahn HK, Parzer P, Rexilius J, Konrad-Verse O, Peitgen HO, Essig M. Diffusion Tensor Imaging in Primary Brain Tumors: Reproducible Quantitative Analysis of Corpus Callosum Infiltration and Contralateral Involvement Using a Probabilistic Mixture Model. Neuroimage. 2006;31:531-542.

5 **Atkinson D,** Counsell S, Hajnal JV, Batchelor PG, Hill DLG, Larkman DJ. Nonlinear Phase Correction of Navigated Multi-coil Diffusion Images. Magn Reson Med. 2006;56:1135-1139.

6 **Liu C,** Bammer R, Kim D, Moseley ME. Self-Navigated Interleaved Spiral (SNAILS): Application to High-Resolution Diffusion Tensor Imaging. Magn Reson Med. 2004;52:1388-1396.

7 **Gudbjartsson H,** Maier SE, Mulkern RV, Mórocz IA, Patz S, Jolesz FA. Line Scan Diffusion Imaging. Magn Reson Med. 1996;36:509-519.

8 **Murphy BP,** Zientra GP, Huppi PS, Maier SE, Barnes PD, Jolesz FA, Volpe JJ. Line Scan Diffusion Tensor MRI of the Cervical Spinal Cord in Preterm Infants. J Magn Reson Imaging. 2001;13:949-953.

9 **Cercignani M,** Horsfield MA, Agosta F, Filippi M. Sensitivity-Encoded Diffusion Tensor MR Imaging of the Cervical Cord. Am J Neuroradiol. 2003;24:1254–1256.

10 **Pruessmann KP,** Weiger M, Scheidegger MB, Boesiger P. SENSE: Sensitivity Encoding for Fast MRI. Magn Reson Med. 1999;42:952-962.

11 **Feinberg DA,** Hoenninger JC, Crooks LE, Kaufman L, Watts JC, Arakawa M. Inner Volume MR Imaging: Technical Concepts and their Application. Radiology. 1985;156:743-747.

12 **Wheeler-Kingshott CA,** Trip SA, Symms MR, Parker GJ, Barker GJ, Miller DH. *In Vivo* Diffusion Tensor Imaging of the Human Optic Nerve: Pilot Study in Normal Controls. Magn Reson Med. 2006;56:446-451.

13 **Wheeler-Kingshott CA,** Hickman SJ, Parker GJ, Ciccarelli O, Symms MR, Miller DH, Barker GJ. Investigating Cervical Spinal Cord Structure Using Axial Diffusion Tensor Imaging. Neuroimage. 2002;16:93-102.

14 **Jeong EK,** Kim SE, Guo J, Kholmovski EG, Parker DL. High-Resolution DTI with 2D Interleaved Multislice Reduced FOV Single-Shot Diffusion-Weighted EPI (2D ss-rFOV-DWEPI). Magn Reson Med. 2005;54:1575-1579.

15 **Jeong EK,** Kim SE, Kholmovski EG, Parker DL. High-Resolution DTI of a localized volume using 3D single-shot diffusion weighted Stimulated Echo-Planr Imaging (3D ss-DWSTEPI). Magn Reson Med. 2006;56:1173-1181.

16 **Schlüter M,** Stieltjes B, Hahn HK, Rexilius J, Konrad-Verse O, Peitgen HO. Detection of Tumor Infiltration in Axonal Fiber Bundles Using Diffusion Tensor Imaging. Int J Med Robot Comput Assist Surg. 2005;1:80-86.

17 **Reese T,** Heid O, Weisskoff RM, Wedeen VJ. Reduction of Eddy-Current-Induced Distortion in Diffusion MRI Using a Twice-Refocused Spin Echo. Magn Reson Med. 2003;49:177-182.

18 **Torrey H.** Bloch Equations with Diffusion Terms. Phys Rev. 1956;104(3):563-565.

19 **Lazar M,** Weinstein DM, Tsuruda JS, Hasan KM, Arfanakis K, Meyerand ME, Badie B, Rowley HA, Haughton V, Field A, Alexander AL. White Matter Tractography Using Diffusion Tensor Deflection. Hum Brain Mapp. 2003;18(4):306-21.

20 **Weinstein D,** Kindlmann G, Lundberg EC. Tensorlines: Advection Diffusion based Propagation through Diffusion Tensor Fields. Proceedings IEEE Visualization. San Francisco, CA, 1999;249–253.

21 Noe A, Gee JC. Partial Volume Segmentation of Cerebral MRI Scan with Mixture Model Clustering. Information Processing in Medical Imaging: 17th International Conference. LNCS 2082. Springer-Verlag, Heidelberg, p.423-430.

22 **Laidlaw DH,** Fleischer KW, Barr AH. Partial-volume Bayesian Classification of Material Mixtures in MR Volume Data Using Voxel Histograms. IEEE Trans Med Imag 1998;17(1),74-86.

23 **Kharbanda HS,** Alsop DC, Anderson AW, Hackney DB. Effects of Cord Motion on Diffusion Imaging of the Spinal Cord. Magn Reson Med. 2006;56:334-339.

24 **Hirsch JG,** Bock M, Essig M, Schad LR. Comparison of Diffusion Anisotropy Measurements in Combination with the FLAIR-Technique. Magn Reson Imaging. 1999;17:705-716.

25 **Mamata H,** Jolesz FA, Maier SE. Apparent Diffusion Coefficient and Fractional Anisotropy in Spinal Cord: Age and Cervical Spondylosis-Related Changes. J Magn Reson Imaging 2005; 22:38-43.

26 **Clark CA,** Barker GJ, Tofts PS. Magnetic Resonance Diffusion Imaging of the Human Cervical Spinal Cord *in vivo*. Magn Reson Med 1999;41:1269-1273.

27 **Ries M,** Jones RA, Dousset V, Moonen CTW, Diffusion Tensor MRI of the Spinal Cord. Magn Reson Med 2000;44:884-892.

28 **Bammer R,** Augustin M, Prokesch RW, Stollberger R, Fazekas F. Diffusion-Weighted Imaging of the Spinal Cord: Interleaved Echo-Planar Imaging is Superior to Fast

152

153

ON CONNECTIVITY IN THE CENTRAL NERVOUS SYSTEM — A MAGNETIC RESONANCE IMAGING STUDY

REPRODUCIBLE EVALUATION OF SPINAL CORD DTI USING AN OPTIMIZED INNER VOLUME SEQUENCE IN COMBINATION WITH PROBABILISTIC ROI ANALYSIS

Spin-Echo. J Magn Reson Imaging 2002;15(4):364-73.

29 **Wilm BJ,** Svensson J, Henning A, Pruessmann KP, Boesinger P, Kollias SS. Reduced
Field-of-View MRI Using Outer Volume Suppression for Spinal Cord Diffusion
Imaging. Magn Reson Med 2007;57:625-630.

30 **Rossi C,** Boss A, Lindig TM, Martirosian P, Steidle G, Maetzler W, Claussen CD,
Klose U, Schick F. Diffusion tensor imaging of the spinal cord at 1.5 and 3.0 Tesla.
Rofo 2007;179(3):219-24.

154

— 9 —

Manganese Enhanced Magnetic Resonance Imaging in a Contusion Model of Spinal Cord Injury in Rats – correlation with motorfunction

N. Walder, A.H. Petter-Puchner, H. Redl, M. Essig, B. Stieltjes

Objectives: Various models of spinal cord injury in rodents have been established and various techniques for lesion quantification have been implemented. Measurement of the extent of the underlying injury is essential to monitor the reproducibility of the experimental injury and for assessment of therapeutic effects. In this study we tested manganese enhanced magnetic resonance imaging (MEMRI) for post-mortem quantification of experimental SCI in rats. Materials and Methods: 12 rats were subjected to contusion injuries at the 11th thoracic vertebra, followed by MnCl2 injections into the cisterna magna. After observation for 3 days, post-mortem MEMRI-features were correlated with values of locomotion testing and histology. Results: MnCl2 yielded a strong contrast enhancement of the uninjured spinal cord, whereas no enhancement was observed at the injury site and caudally. MRI findings correlate closely with values of locomotor rating. Conclusions: MEMRI represents a reliable method for visualization and functional assessment of spinal cord integrity in rats.

Introduction

In past decades, various models of experimental spinal cord injury (SCI) have been implemented (e.g. contusion, hemisection) to adequately test promising therapeutic strategies[1,2] and techniques to assess the neurological deficits have been applied[3,4,5]. However, current methods like histology or locomotor rating scale have certain limitations, and a lack of standardization of clinical read-out measures hampers direct comparison of injury models and therapeutic outcomes[6].

Magnetic resonance imaging (MRI) of acute spinal injury provides excellent visualization of neurological and soft-tissue structures noninvasively[7]. Manganese enhanced magnetic resonance imaging (MEMRI) has been used successfully for the visualization of neuronal circuits and activity patterns of the brain in different animal models[8,9,10]. Mn^{2+} is a paramagnetic ion which leads to a strong contrast enhancement in T_1-weighted MRI. Its chemical properties resemble calcium, which results in an active transport of Mn^{2+} into intact active neurons via voltage-gated Ca^{2+} channels, followed by a fast, anterograde microtubuli-based transport and transport across active synapses. Thus Mn^{2+} leads to contrast enhancement of intact neurons, whereas there is a lack in Mn^{2+} uptake and contrast enhancement in injured neurons[6,11]. Recently, it has been demonstrated that MEMRI represents a sensitive *in vivo* method for monitoring neuronal activity and functionality within the injured spinal cord of mice[6]. Sharp trauma was used in this study for SCI. One limitation of sharp trauma is poor control of the inflicted injury.

The objective of this study was to establish MEMRI as an objective and non-invasive post-mortem method for both structural and functional assessment of spinal cord contusion injury in rat. We correlated the imaging derived parameters of manganese uptake with clinical parameters of locomotion testing as well as histology, using an impactor device that yields reproducible contusion injury[12].

Materials and Methods

12 male Sprague-Dawley rats, weighing 250-300 g were obtained from the Institut fuer Labortierkunde und –genetik der Medizinischen Universität Wien (Himberg, Austria). The protocol was in accordance with national and international guidelines on the use of laboratory rats and approved by the city government of Vienna. Surgical procedures were carried out at the Ludwig Boltzmann Institute for Experimental and Clinical Traumatology (Vienna); MRI of collected specimens was performed at the German Cancer Research Center (DKFZ, Heidelberg, Germany). Prior to surgery, rats were randomized into two groups (n=6 each).

Surgery

Twelve rats were anesthetized with intraperitoneal injections of Ketasol [®] (Ketaminhydrochloride 100 ml/mg, Dr. E. Graeub AG, Bern, Switzerland) and Rompun [®] (Xylazine-Hydrochloride, γ-Hydroxybenzoacidmethyl-esterate, 2%, Bayer, Leverkusen, Germany). Core body temperature was measured with a rectal probe and maintained at 37-38°C with a heating pad until recovery.

A laminectomy was carried out on each rat at the level of the 11th thoracic vertebra (TH11) and a contusion injury was evoked using the Infinite Horizon Impactor (Precision Systems and Instrumentation, LLC, Lexington, KY, USA). This device allows for application of standard-force contusion injuries to the spinal cords of mice and rats. Impact force and displacement are selectable displayed as time-dependent curves[12, 13]. Rats were subjected to injuries with an impact force of 50 kilodyne (kdyn or 0.05 x 103 Newton; group 1, n = 6) or 150 kdyn (or 0.15 x 103 Newton; group 2, n = 6), respectively. The wound was closed in anatomical layers.

MnCl$_2$ Injections

MnCl$_2$-injections were administered immediately after surgery. Rats were placed on a Styrofoam block, with 90° declination of the head. 80 μl of a 0.8M MnCl$_2$-solution was manually injected into the cisterna magna via the membrana atlanto-occipitalis using a 27-gauge needle.

Post surgery animal care

Post-operative management was identical for all rats in the study. Subcutaneous (sc.) injections of 10 ml Ringer's solution and antibiotics (Peni-Strepto [®], 50,000 IU, Virbac Lab., Carros, France) were administered promptly after surgery as well as once daily until euthanization. Rats were housed under simulated daylight conditions with alternating 12-hour light-dark cycles. Standard rat food and water was provided and rats were checked daily for signs of infection or dehydration. When necessary, manual bladder expression was carried out until spontaneous urination occured

Locomotion testing

Tests were performed by observers unaware of injury force on day 3 post-injury using the locomotor rating scale by Basso, Beattie and Bresnahan (BBB-score)[4]. It allows separate assessment of hind-limb function using a scale from 0 to 21, where 0 denotes total paraplegia and 21 denotes full function of the hind-limb. The rating 10 stands for "occasional weight supported plantar steps, no forelimb-hindlimb coordination". All rats were euthanized after locomotion testing on day 3.

Euthanization

All animals were euthanized after observation for 3 days. Rats were anesthetized as previously described. After intravenous injection of 0.3 ml of Heparin (1000 I.E.,Heparin ImmunoÒ, EBEWE Pharma Ges.m.b.H Nfg.KG, Unterach, Austria) rats were transcardially perfused with 50ml of saline, followed by 50 ml of buffered formaldehyde solution (4.5%, VWR, Prolabo, Leuven, Belgium).

ON CONNECTIVITY IN THE CENTRAL NERVOUS SYSTEM — A MAGNETIC RESONANCE IMAGING STUDY

MANGANESE ENHANCED MAGNETIC RESONANCE IMAGING IN A CONTUSION MODEL OF SPINAL CORD INJURY IN RATS – CORRELATION WITH MOTORFUNCTION

The vertebral column was excised from the first cervical to the second lumbar vertebra, implicating the lesion site. Samples were stored in formaldehyde solution for further proceedings. Lesion site was distinguishable by the laminectomy.

MRI

For MRI, the excised vertebral columns were stored in 15 ml polypropylene-tubes with a diameter of 23 mm, in order to avoid motion artefacts. The tubes were filled with formaldehyde solution for conservation of the samples. The position of the lesion was marked on the tubes.

MRI was performed at room temperature on a clinical 1.5-T-scanner (Siemens Symphony, Erlangen, Germany) with a dedicated custom-made animal volume resonator[6] using a 3D-FLASH imaging pulse sequence with the following parameters: TR/TE 14.0/5.22 ms, flip angle 30°, 28 partitions, partition thickness: 0.5 mm, FOV 80 mm, matrix size 512 times 512, voxel size 0.15 times 0.15 mm, 32 averages. Imaging was performed perpendicular to the spinal cord. Imaging time was 60 minutes per sample.

Histology

After MRI the vertebral columns were opened and the lower thoracic spinal cord containing the lesion was excised from each sample. The spinal cord at TH 11 was explanted, including the site of maximum damage which was determined by the hemorrhagic contusion mark. After embedding in paraffin, transverse sections (5μm) were taken at 100 μm intervals. Serial sections were stained with hematoxylin-eosine, Cresyl echt violet stain and luxol blue. At the site of maximum injury, sections were examined for the extent of damaged neuronal tissue, hemorrhage and macrophages as a sign of inflammation. These parameters were graded from zero to three by the pathologist. Zero indicated no, 1 moderate, 2 strong and 3 maximum alteration in comparison to tissue from native rats, based on the following criteria:

Demyelination:

0 - no demyelination
1 - up to 5% of cross sectional area demyelinated
2 - 6 - 30% of cross sectional area demyelinated
3 - more than 30% of cross sectional area demyelinated

Vacuolization:

0 - no vacuolization
1 - up to 5% of cross section area vacuolized
2 - 6 - 30% of cross section area vacuolized
3 - more than 30% of cross section area vacuolized

Macrophages:

0 - no macrophages
1 - 1 - 10 macrophages per high power field of lesion (HPF, 400 x magnification)
2 - 11 - 50 macrophages per high power field of lesion (HPF, 400 x magnification)
3 - more than 50 macrophages per high power field of lesion (HPF, 400 x magnification)

Hemorrhage:

0 - no extravasation of erythrocytes in cross section area
1 - extravasation of erythrocytes in up to 5% of cross section area
2 - extravasation of erythrocytes in 6 - 30% of cross section area
3 - extravasation of erythrocytes in more than 30% of cross section area

Data processing and statistical analysis

Images were evaluated using the scanner software package (Syngo, Siemens Erlangen, Germany). The spinal cord was outlined on axial slices and the mean signal was calculated. A region of interest was placed outside the animal contours for noise measurement. SNR in the most proximal slice was set to 100% and SNRs in consecutive slices were scaled accordingly expressing relative

ON CONNECTIVITY IN THE CENTRAL NERVOUS SYSTEM — A MAGNETIC RESONANCE IMAGING STUDY

MANGANESE ENHANCED MAGNETIC RESONANCE IMAGING IN A CONTUSION MODEL OF SPINAL CORD INJURY IN RATS — CORRELATION WITH MOTORFUNCTION

160

161

SNRS (%SNR) as previously described[6]. Statistics were performed using SAS/STAT (SAS Institute GmbH, Heidelberg, Germany). Mean and standard deviation (SD) were calculated for %SNR and values of locomotor rating of each group. Differences in %SNR and mean values of locomotor rating between both groups were assessed with T-TEST (99% confidence). Relation between %SNRS at the lesion site and locomotor rating was determined using Pearson's correlation.

Results

MRI

The described sequence yielded good image quality for *postmortem* imaging of the spinal cord. In all rats, injection of MnCl2 into the cisterna magna yielded a consistently strong contrast enhancement of the uninjured spinal cord in T_1-weighted MRI (figure 1b). In SCI, manganese uptake by active neuronal tissue resulted in signal enhancement, reflected by a high SNR in the neuronal tissue cranial to the injury site, followed by a decrease in SNR both at and caudal to the lesion (figure 1a). The decline of SNR first seemed slightly cranial to the defined lesion localization at TH11. Contrast enhancement in the intact spinal cord yielded a clear depiction of the gray matter in the typical butterfly form (figure 1b). Gray matter could not be delineated either at or caudal to injury site (figure 1c, d). %SNR results of group 1 (50 kDyn) showed a mean of 60.9 and an SD of 2.5. No application failure occurred in group 1. SNR results of group 2 (150 kDyn) showed a mean of 39.8 and an SD of 5.5. No application failure occurred in group 2. The mean %SNR was significantly lower in the 150 kDyn group than in the 50 kDyn group (P < 0.0002).

Locomotor rating

Locomotor rating results of group 1 (50 kDyn) showed a mean of 19.7 and an SD of 1.0; results of group 2 (150 kDyn) showed a mean
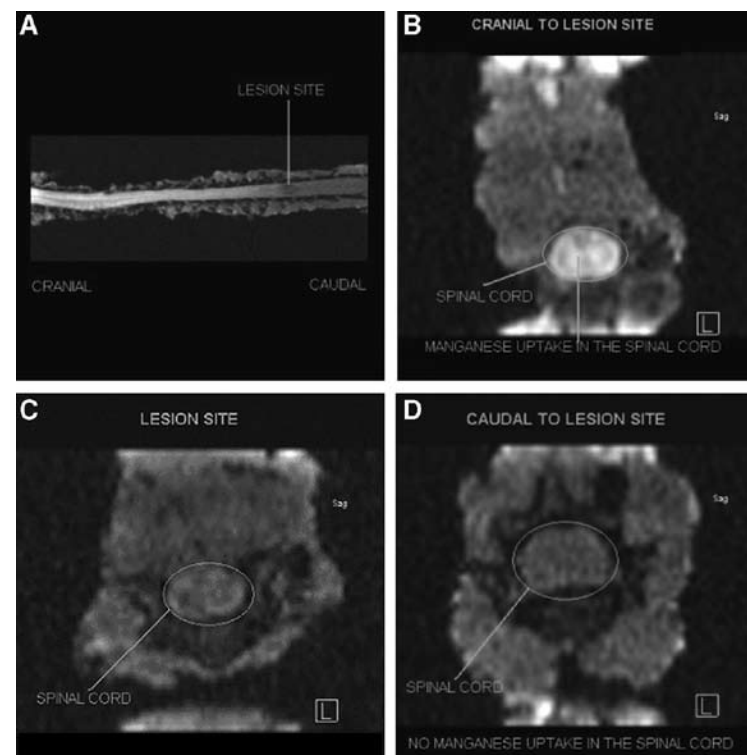
Figure 1 A, MEMRI of SCI. Strong contrast enhancement of intact neuronal tissue cranial to lesion site, followed by a decrease in SNR at lesion site, and lack of enhancement caudal to lesion. B, Axial MRI of the spinal cord, cranial lesion site. Pronounced signal enhancement of the "butterfly"-shaped gray matter. C, Axial MRI of the lesion. Deficiency of manganese uptake results in absence of signal enhancement. D, Axial MRI of the spinal cord, caudal to lesion site. Shows no signal enhancement of neurons. Cause of SNR decrease in this section of the spinal cord has not yet been investigated.

of 6.5 and an SD of 3.2. The mean locomotor rating for the 150 kDyn group was significantly lower than for the 50 kDyn group (P < 0.0003). Comparison of locomotor rating values of both groups on day 3 postinjury is depicted in figure 2. Group 1 (50 kdyn) showed explicitly higher values than group 2 (150 kdyn), inferring that a lower injury force results in improved motor function of the hind limbs. Group 1 values ranged from 18 to 21, denoting consistent plantar stepping with forelimb-hindlimb coordination

ON CONNECTIVITY IN THE CENTRAL NERVOUS SYSTEM — A MAGNETIC RESONANCE IMAGING STUDY

MANGANESE ENHANCED MAGNETIC RESONANCE IMAGING IN A CONTUSION MODEL OF SPINAL CORD INJURY IN RATS
— CORRELATION WITH MOTORFUNCTION

Figure 2 Locomotor rating values on day 3 postinjury. A, Results of group 1 (50 kdyn) ranged from 18 to 21, mean of 19.7. B, Increased impairment of motor function in group 2 (150 kdyn). Values ranged from 1 to 11, mean of 6.5.

Figure 3 MRI %SNR at lesion site. A, Results of group 1 (50 kdyn), mean %SNR of 60.9. B, Lower values in group 2 (150 kdyn), mean %SNR of 39.8.
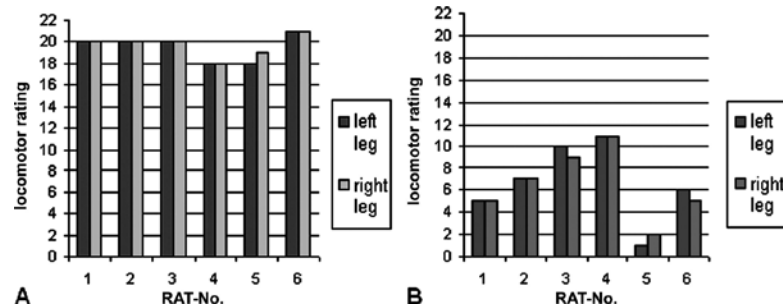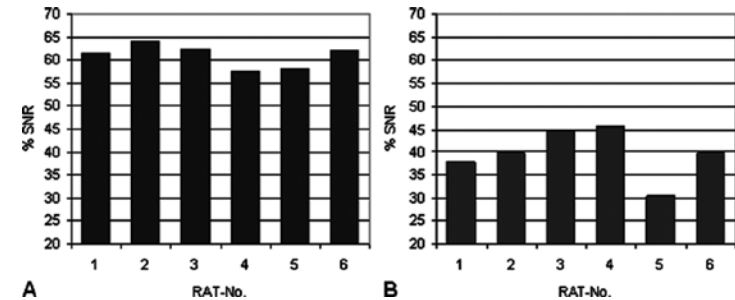
during gait, and permanent toe clearance and parallel paw position at initial contact and lift-off of the hindlimb, varying in points of trunk instability and ability to keep the tail up. Group 2 values ranged from 1 to 11, with 1 denoting slight movement of 1 or 2 joints and 11 denoting frequent to consistent weight-supported plantar steps without forelimb-hindlimb coordination. A score of 7, which is approximately the mean in this group, denotes extensive movement of all 3 joints.

Correlation of MRI and locomotor rating

Comparison of %SNR at lesion sites of both groups is shown in figure 3 According to the locomotor rating results, group 1 showed higher values of %SNR than group 2. In figure 4, %SNRs of all rats are depicted depending on average locomotor rating values, showing an almost linear correlation of these 2 parameters. Calculation of Pearson correlation yielded a value of 0.99 (P = 0.001).

Histology

Histologic evaluation of the lesions supports MRI findings. Group 1 samples indicated a higher degree of tissue integrity. Semiquantitative parameters of neuronal damage, such as
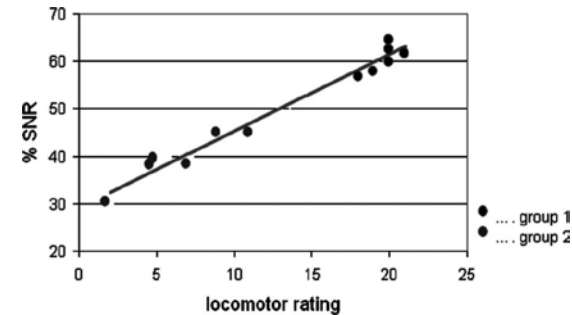
Figure 4 Correlation of %SNR with the locomotor rating values: MEMRI features of group 1 and group 2 plotted against the locomotor rating values. R = 0.99.

demyelination and vacuolization, were minor when compared with samples of group 2, and signs of hemorrhage and inflammation, characterized by invasion of macrophages. No parameter was graded 3 (maximum alteration) in group 1 or group 2. Results of the histologic grading are listed in Table 1.

Figure 5 shows spinal cord slices and semiquantitative evaluation of an animal of group 1; figure 6 shows corresponding slices and evaluation of an animal of group 2.

ON CONNECTIVITY IN THE CENTRAL NERVOUS SYSTEM — A MAGNETIC RESONANCE IMAGING STUDY

MANGANESE ENHANCED MAGNETIC RESONANCE IMAGING IN A CONTUSION MODEL OF SPINAL CORD INJURY IN RATS
– CORRELATION WITH MOTORFUNCTION

	No. Samples	
	Group 1 (50 kdyn)	Group 2 (150 kdyn)
Demyelination		
Grade 0	3	0
Grade 1	3	3
Grade 2	0	3
Vacuolization		
Grade 0	0	0
Grade 1	6	4
Grade 2	0	2
Macrophages		
Grade 0	3	0
Grade 1	2	2
Grade 2	1	4
Hemorrhage		
Grade 0	1	0
Grade 1	5	3
Grade 2	0	3

Table 1 Histological evaluation of group 1 and group 2.

Figure 5 Typical histology example from group 1. No demyelination or occurrence of macrophages could be observed. Vacuolization (arrow v) and hemorrhage (arrow h) were mild and correspondingly graded 1. Parameters were generally graded minor in this group when compared with group 2. Only 1 sample from this group was graded 2 in terms of macrophages.
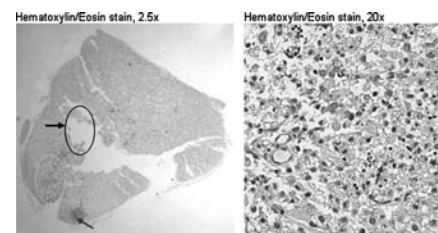
Figure 6 Typical histology example from group 2. Demyelination (arrow d) and vacuolization (arrow v) were moderate and therefore graded 2. The parameter "macrophages" (arrow m) was graded 2; only hemorrhage (arrow h) was reported as mild and therefore graded 1. All parameters in this group were graded 1 or 2 (moderate or strong alteration), no parameter was graded 0. Gradings of demyelination and macrophages were especially higher than group 1, representing higher degree of injury and neuronal damage.

Discussion

This study demonstrates for the first time that MEMRI is an objective method for both structural depiction and functional assessment of spinal cord contusion injury in rats, as the MRI features of spinal cord impairment correlate with clinically derived values and are also in accordance with histology findings. Both MEMRI and locomotor rating show that the applied contusion model for SCI yields reproducible SCI with minimal variance in each group. Variations within the groups are most likely due to parameters that influence injury outcome, especially in the early phase (ie, immunologic condition, slight age differences). The MEMRI method is minimally invasive, preventing additional damage to the neuronal tissue and allows for *in vivo* measurements in rats in the future. Thus, MnCl2 injection into the cisterna magna allows objective quantification of the functional status of the spinal cord *in vivo*, providing the possibility for kinetic follow-ups of injury development and therapeutic outcome. One potential disadvantage of Mn2+ is its neurotoxicity at higher concentrations that can lead to manganism, marked by symptoms of tremors, gait disorders, compromised motor skills, and abnormal balance. In accordance with previous reports,[6] we did not observe any of these symptoms of extrapyramidal motor system dysfunction at the concentrations used. One reason may be that MnCl2 dilutes quickly when injected into cerebrospinal fluid (CSF). Also, manganism described in mine workers is due to chronic exposure to manganese that may have different toxicologic effects when compared with a single exposure[14].

Currently, various techniques are used to evaluate sci, but all techniques have their limitations. Common procedures of lesion depiction, like histology and anterograde or retrograde tracing techniques, are limited to the structural assessment of the damage and require invasive preparation of the spinal cord, risking secondary damage to neuronal tissue. Behavioral tests, such as the locomotor rating scale, allow functional *in vivo* assessment of impairment but do not allow visualization of the neuronal tissue and the underlying mechanisms of sci. Well-trained observers are required to ensure objective results.

With the variety of procedures to assess spinal cord integrity and recovery, a general problem is the lack of standardization among different laboratories, complicating the comparison of successful therapies.

One clinical application of MRI to study the condition of neuronal white matter is diffusion tensor imaging (DTI). It has recently been shown that DTI can be used as a stable and observer-independent *in vivo* measure for the comparative assessment of white matter integrity[15]. The method allows imaging of fiber tracts by measuring water diffusion and anisotropy as markers of neuronal tissue integrity. Commonly used for the depiction of neurologic diseases concerning the brain, ie, Alzheimer disease, microangiopathy and paraneoplastic diseases, the reproducibility of this method was recently validated, also for higher-field MRI techniques[16]. DTI continues to gain acceptance in spinal cord imaging[17] and it was recently demonstrated that *in vivo* derived DTI parameters are sensitive and specific biomarkers for spinal cord white matter damage in mice[18]. In comparison to MEMRI, DTI provides information about the structural integrity of the tissue but cannot assess tissue viability, it mainly detects changes in fiber integrity when secondary loss of axons leads to a reduction in axon count.

Mn2+ is a divalent ion which mimics Ca2+ and is therefore actively transported into intact neurons via voltage-gated calcium channels; its uptake is reduced in injured, disconnected neurons. Uptake is followed by axonal transport at a rate that depends on injection volume and functional status of the neuronal tissue[19]. After cisterna magna injection of MnCl2, Mn2+ is directly distributed via the csf and leads to strong contrast enhancement

of intact neuronal tissue in T_1-weighted MRI, whereas there is a lack of enhancement in injured neurons[6,11]. Thus, MEMRI offers both structural and functional information about neuronal tissue.

Pautler et al were the first to use Mn2+ for the depiction of neuronal pathways in the olfactory system of mouse brains[19]. Since then, various tract-tracing studies have been performed on different species, laying the foundation of Mn2+-enhanced functional studies in the central nervous system[20-23]. A recent publication describes the use of Mn2+ for depiction of sci in a rat hemisection model via direct injection of MnCl2 into the white matter of the spinal cord[23]. Stieltjes et al[6] described the use of MEMRI for functional depiction of sci in the mouse *in vivo*. As in our study, MnCl2 was injected into the csf, without requiring an additional laminectomy. That minimizes injection-induced trauma. One major disadvantage of the used transection model carried out at the level of TH 7/8 in that study is poor control by nature of sharp trauma models.

In our study, the decrease of snr first seems slightly cranial to the defined lesion location, surely due to the spreading of apoptosis and inflammatory response after spinal cord injury[24, 25]. The lack in snr caudal to the lesion could partly be connected with this spreading of injury. Stieltjes et al[6] observed a similar behavior in enhancement. They investigated if a block in csf circulation after sci could be a reason for signal decrease in the caudal part of the spinal cord, as Mn2+ is distributed via the csf in the uninjured spinal canal. But gadolinium-diethylenetriamine penta-acetic acid (DTPA) injection into the cisterna magna showed that the injury had not led to a complete disruption of the csf circulation.

The excellent correlation we observed in this study between 2 distinct *in vivo* techniques of sci quantification is very promising. Further research is warranted to evaluate the precise relationship between applied contusion pressure and final clinical outcome.

ON CONNECTIVITY IN THE CENTRAL NERVOUS SYSTEM — A MAGNETIC RESONANCE IMAGING STUDY

MANGANESE ENHANCED MAGNETIC RESONANCE IMAGING IN A CONTUSION MODEL OF SPINAL CORD INJURY IN RATS — CORRELATION WITH MOTORFUNCTION

MnCl$_2$ enhanced MRI represents a standardizable and reliable method for postmortem depiction and quantification of spinal cord contusion injuries in rats. As MRI features of lesion quantification correlate closely with results of clinical assessment of motor function, MEMRI yields a measure of functional postmortem imaging of spinal cord integrity and severity of SCI, additionally providing a structural depiction of the spinal cord. Our method can be used in laboratories without an on-site imaging facility that otherwise prevents *in vivo* imaging. Also, our results indicate that *in vivo* MEMRI of rat spinal cord seems feasible using the procedure described.

1 **Rosenzweig ES,** McDonald JW. Rodent models for treatment of spinal cord injury: research trends and progress toward useful repair. Curr Opin Neurol. 2004 Apr;17(2):121-31.

2 **Kwon BK,** Oxland TR, Tetzlaff W. Animal models used in spinal cord regeneration research. Spine. 2002 Jul 15;27(14):1504-10

3 **McEwen ML,** Springer JE. Quantification of locomotor recovery following spinal cord contusion in adult rats. J Neurotrauma. 2006 Nov;23(11):1632-53.

4 **Basso DM,** Beattie MS, Bresnahan JC. (1995) A sensitive and reliable locomotor rating scale for open field testing in rats. Journal of Neurotrauma, 12:1-21.

5 **Rivlin AS,** Tator CH. Objective clinical assessment of motor function after experimental spinal cord injury in the rat. J Neurosurg 1977; 47: 577-581.

6 **Stieltjes B,** Klussmann S, Bock M et al. Manganese-enhanced magnetic resonance imaging for *in vivo* assessment of damage and functional improvement following spinal cord injury in mice. Magn Reson Med. 2006 May; 55(5):1124-31.

7 **Slucky AV,** Potter HG. Use of magnetic resonance imaging in spinal trauma: indications, techniques, and utility. J Am Acad Orthop Surg. 1998 May-Jun;6(3):134-45

8 **Aoki I,** Wu YJ, Silva AC et al. *In vivo* detection of neuroarchitecture in the rodent brain using manganese-enhanced MRI. Neuroimage. 2004 Jul;22(3):1046-59.

9 **Van der Linden A,** Verhoye M, Van Meir V et al. *In vivo* manganese-enhanced magnetic resonance imaging reveals connections and functional properties of the songbird vocal control system. Neuroscience. 2002;112(2):467-74.

10 **Saleem KS,** Pauls JM, Augath M et al. Magnetic resonance imaging of neuronal connections in the macaque monkey. Neuron. 2002 May 30;34(5):685-700.

11 **Watanabe T,** Michaelis T, Frahm J. Mapping of retinal projections in the living rat using high-resolution 3D gradient-echo MRI with Mn2+-induced contrast. Magn Reson Med. 2001 Sep;46(3):424-9.

12 **Scheff SW,** Rabchevsky AG, Fugaccia I et al. Experimental modeling of spinal cord injury: characterization of a force-defined injury device. J Neurotrauma. 2003 Feb;20(2):179-93.

13 **John JP,** Pintsov O, Petter-Puchner A et al. Nitric oxide and oxygen radical attack on GDP-dissociation inhibitor 2 (GDI-2) in spinal cord injury of the rat. J Proteome Res. 2007 Apr; 6(4): 1500-9.

14 **Schuler P,** Oyanguren H, Maturana V et al. Manganese poisoning; environmental and medical study at a Chilean mine. Ind Med Surg. 1957 Apr; 26(4): 167-73.

15 **Deppe M,** Duning T, Mohammadi S, et al. Diffusion-tensor imaging at 3 T : detection of white matter alterations in neurological patients on the basis of

ON CONNECTIVITY IN THE CENTRAL NERVOUS SYSTEM — A MAGNETIC RESONANCE IMAGING STUDY

MANGANESE ENHANCED MAGNETIC RESONANCE IMAGING IN A CONTUSION MODEL OF SPINAL CORD INJURY IN RATS
— CORRELATION WITH MOTORFUNCTION

normal values. Invest Radiol 2007;42:338-345

16 **Jansen JF,** Kooi ME, Kessels AG, Nicolay K, Backes WH. Reproducibility of quantitative cerebral T2 relaxometry, diffusion tensor imaging, and 1H magnetic resonance spectroscopy at 3.0 Tesla. Invest Radiol 2007;42: 327-337

17 **Ellingson BM,** Ulmer JL, Schmit BD. Optimal diffusion tensor indices for imaging the human spinal cord. Biomed Sci Instrum. 2007;43:128-33

18 **Loy DN,** Kim JH, Xie M, et al. Diffusion tensor imaging predicts hyperacute spinal cord injury severity. J Neurotrauma 2007 Jun; 24(6):979-90

19 **Liu XZ,** Xu XM, Hu R, et al. Neuronal and glial apoptosis after traumatic spinal cord injury. J Neurosci. 1997 Jul 15; 17(14): 5395-406

20 **Carlson SL,** Parrish ME, Springer JE, Doty K, Dossett L. Acute Inflammatory Response in Spinal Cord Following Impact Injury. Exp Neurol. 1998 May;151(1): 77-88.

21 **Pautler RG,** Silva AC, Koretsky AP. *In vivo* neuronal tract tracing using manganese-enhanced magnetic resonance imaging. Magn Reson Med. 1998 Nov;40(5):740-8.

22 **Pautler RG,** Mongeau R, Jacobs RE. *In vivo* trans-synaptic tract tracing from the murine striatum and amygdala utilizing manganese enhanced MRI (MEMRI). Magn Reson Med. 2003 Jul;50(1):33-9.

23 **Leergaard TB,** Bjaalie JG, Devor A et al. *In vivo* tracing of major rat brain pathways using manganese-enhanced magnetic resonance imaging and three-dimensional digital atlasing. Neuroimage 2003 Nov;20(3):1591-600.

24 **Lin YJ,** Koretsky AP. Manganese ion enhances T1-weighted MRI during brain activation: an approach to direct imaging of brain function. Magn Reson Med. 1997 Sep;38(3):378-88.

25 **Bilgen M,** Dancause N, Al-Hafez B et al. Manganese-enhanced MRI of rat spinal cord injury. Magn Reson Imaging. 2005 Sep;23(7):829-32.

172

— 10 —

Manganese-enhanced magnetic resonance imaging for *in vivo* assessment of damage and functional improvement following spinal cord injury in mice

B. Stieltjes, S. Klussmann, M. Bock, R. Umathun, J. Mangalathu, E. Letellier, W. Rittgen, L. Edler, P.H. Krammer, H.U. Kauczor, A. Martin-Villalba and M. Essig

In the past decades, much effort has been invested in developing therapies for spinal injuries. Lack of standardization of clinical read-out measures, however, makes direct comparison of experimental therapies difficult. Damage and therapeutic effects *in vivo* are routinely evaluated using rather subjective behavioural tests. Here we show that manganese-enhanced magnetic resonance imaging (MEMRI) can be used to examine the extent of damage following spinal cord injury (SCI) in mice *in vivo*. Injection of MnCl2 solution into the cerebrospinal fluid (CSF) leads to manganese uptake into the spinal cord. Furthermore, after injury MEMRI-derived quantitative measures correlate closely with clinical locomotor scores. Improved locomotion due to treating the detrimental effects of SCI with an established therapy (neutralization of CD95Ligand) is reflected in an increase of manganese uptake into the injured spinal cord. Therefore, we demonstrate that MEMRI is a sensitive and objective tool for *in vivo* visualization and quantification of damage and functional improvement after SCI. Thus, MEMRI can serve as a reproducible surrogate measure of the clinical status of the spinal cord in mice, potentially becoming a standard approach for evaluating experimental therapies.

Introduction

Traditionally, neuro-anatomical connections have been primarily studied in animals using degeneration methods[1] and anterograde/retrograde tracing techniques[2]. These techniques have two major disadvantages. First, animals need to be sacrificed for further processing for histology precluding longitudinal studies in the same subject. Second, these techniques yield structural information of connections but exclude the possibility of functional assessment.

Mn^{2+} is known to cause a shortening of the T_1 time of water protons in MRI leading to a strong contrast enhancement in T_1-weighted MRI[3]. Mn^{2+} is a divalent ion with chemical properties resembling Ca2+. It is actively transported into neurons via voltage-gated Ca^{2+} channels[4]. Generally, three major applications of MEMRI have developed[5]:
1 as a tissue contrast agent,
2 as a surrogate marker for neuronal cell activity and
3 for tracing of neuronal tracts.

First, after systemic $MnCl_2$ injection in rodents, specific uptake patterns of Mn^{2+} with enrichment within the grey matter of the brain were described[6,7]. Second, Mn^{2+} has been successfully used as a Ca^{2+} analogue to visualize activity-dependent uptake into the rat brain[3]. This has also been shown in songbirds, where an injection of MnCl2 solution into the cortex gave rise to a selective pattern of Mn^{2+} uptake in the brain[8]. Importantly, the amount of uptake was dependent on the level of neuronal activity[9]. Third, Pautler et al. were the first to exploit MEMRI for depicting neuronal connections. Injection of $MnCl_2$ solution into the vitreal chamber enabled visualization of the optical tract in mice[10]. Consecutively, multiple other uses have been described like intracranial $MnCl_2$ injection that resulted in the enhancement of several white matter tracts of the monkey brain[11]. Once inside an axon, Mn^{2+} is transported in both antero- and retrograde direction. Trans-synaptic propagation has also been observed[12].

In the last years the development of MRI techniques for *in vivo* examination of the injured spinal cord has been accelerated. Promising approaches using functional MRI in rodents have been

designed by different groups[13,14]. Similarly, diffusion anisotropy MRI has been applied for quantitative assessment of recovery following SCI in rats[15]. Very recently, the potential use of MEMRI to examine the axonal connectivity after SCI has been explored[16]. Nevertheless, the high intrinsic variability of these methods, although generally functional, renders them unsuitable for quantitative discrimination of minute differences in spinal cord integrity, especially in small animals like mice.

To date, no data is available on the *in vivo* visualization of the functional status of the mouse spinal cord using $MnCl_2$. We hypothesized that an intracerebroventricular (i.c.v.) injection of $MnCl_2$ would lead to spinal Mn^{2+} uptake with the amount of Mn^{2+} uptake into the spinal cord depending on its functional status. We tested this hypothesis in a mouse model of SCI, in which animals were treated with a therapy (neutralizing antibodies against CD95Ligand) that is neuroprotective and leads to axonal regeneration resulting in strong functional improvement[6,17]. Here, we show that MEMRI-derived parameters correlate closely with clinical scores of locomotor function. Therefore, MEMRI may serve as a sensitive *in vivo* method for monitoring neuronal activity and functionality within the spinal cord and, moreover, could provide an objective *in vivo* parameter for the evaluation of damage after SCI and treatment effects.

Materials and Methods

Spinal Cord Injury (SCI)

Animal experiments were approved by the German Cancer Research Center institutional animal care and use committee and the Regierungspräsidium Karlsruhe. For SCI, $MnCl_2$ injection and MRI scan animals were anesthetized using isoflurane. SCI was performed essentially as described before[17]. In brief, after laminectomy at the level Th 7/8 the dorsal 80% of the spinal cord were transected using fine irridectomy scissors leaving only the ventral funiculus intact. This procedure results in complete paraplegia directly after injury. Minor spontaneous recovery of

hind limb function is usually observed in the consecutive weeks. In the double-blind therapy experiment, injured mice received saline solution or were treated with 50 µg neutralizing antibodies directed against CD95Ligand (MFL3; Pharmingen). Antibody and saline were injected intraperitoneally 30 min before SCI as well as twice weekly in the following 5 weeks.

Contrast Agent Injection

For i.c.v. injections anesthetized animals were mounted onto a stereotaxic frame. 0.25 µl 0.8 M $MnCl_2$ solution in saline were injected bilaterally into the lateral ventricles (coordinates: 1 mm caudal to the bregma, 1.5 mm lateral, 1.8 mm depth) using a microinjector (Harvard Apparatus). For cisterna magna injections, 0.5 µl 0.8 M $MnCl_2$ solution or 10 µl 0.5 M Gadolinium-DTPA solution (Magnevist, Schering), respectively, were injected using a 27 g needle attached to a microsyringe as described[18]. The $MnCl_2$ dose for intravenous (i.v.) application into the tail vein was 0.2 mmol/kg and 1 mmol/kg for subcutaneous (s.c.) administration.

Study Groups

The study was divided into several parts. In the first part, the time course experiment of Mn^{2+} uptake into the spinal cord, we performed an i.c.v. injection of $MnCl_2$ solution in one animal and measured the contrast enhancement in the spinal cord 0, 1, 2, 4, 8, 12, 24, 72 and 120 h afterwards. To evaluate alternative application routes, $MnCl_2$ solution was administered either i.v., s.c. or into the cisterna magna (n=2 per group). Imaging was performed 8 to 24 h after injection. In the second part, the comparison of contrast enhancement in the spinal cords of injured and uninjured mice, animals subjected to SCI (n=10) and uninjured controls (n=5) received $MnCl_2$ injections 5 weeks after SCI. MRI followed 60 h later. In the third part, the therapy experiment, $MnCl_2$ solution was injected into antibody-treated and control mice (n=6 per group) at 4 h and 5 weeks after SCI. Imaging was

ON CONNECTIVITY IN THE CENTRAL NERVOUS SYSTEM — A MAGNETIC RESONANCE IMAGING STUDY

MANGANESE-ENHANCED MAGNETIC RESONANCE IMAGING FOR IN VIVO ASSESSMENT OF DAMAGE AND FUNCTIONAL IMPROVEMENT FOLLOWING SPINAL CORD INJURY IN MICE

always performed 60 h after injection. To examine the integrity of the CSF circulation system, Gadolinium-DTPA was injected into the cisterna magna of uninjured (n=2) and injured mice at 5 weeks after SCI (n=6). MRI followed at multiple time points between 5 min and 6 h after injection.

Behavioral Testing

All tests were performed in a double-blind manner. Spinal cord-injured mice were tested in the BBB locomotor and grid walk tests at 1, 2, 3, 4 and 5 weeks after injury. The BBB test was additionally performed after 1 day. All behavioral tests were recorded with a video camera. For assessing the overall locomotor performance the BBB locomotor rating scale was used with slight modifications[17,19]. The BBB scale is a standard measure for analyzing the open field locomotor performance of rats after SCI and grades the functional status of their limbs based on different aspects like joint movement, paw placement, weight support, coordination etc. Complete paraplegia results in a score of 0, while normally functional uninjured animals receive 21 points[19]. Deficits in descending motor control were examined using the grid walk test[17,20]. In this task the animals have to traverse a horizontal ladder-like grid that is elevated above the ground. To cross this runway animals have to place their limbs accurately on the irregularly spaced bars. The numbers of foot placement mistakes for 10 steps of each hind limb are counted and summed up. Uninjured mice usually make none or very few mistakes, whereas paraplegic animals are unable to step and therefore receive 20 error points.

MRI

MRI experiments were performed on a clinical 1.5 T scanner (SIEMENS Symphony, Erlangen, Germany) with a dedicated custom made animal volume resonator using a 3D-FLASH imaging pulse sequence with the following parameters. Mn^{2+} uptake time series experiment: TR = 35.0 ms, TE = 4.1 ms, flip angle = 70°, 60

partitions, partition thickness = 0.2 mm, FOV = 27 x 20 mm, matrix size = 128 x 96, voxel size = 0.2 x 0.2 x 0.2 mm, 22 averages. SCI and therapy experiments: TR = 14.0 ms, TE = 5.22 ms, flip angle = 30°, 28 partitions, partition thickness = 0.5 mm, FOV = 80 x 80 mm, matrix size = 512 x 512, voxel size = 0.15 x 0.15 mm, 32 averages. The experiments were performed in sagittal plane for positioning (3 averages) and in axial plane for detailed spinal cord imaging. Total imaging time was 60 minutes. Cisterna magna injection of $MnCl_2$ experiment: TR = 35.0 ms, TE = 4.1 ms, flip angle = 70°, 60 partitions, partition thickness = 0.2 mm, FOV = 51 x 29 mm, matrix size = 256 x 144, voxel size = 0.2 x 0.2 x 0.2 mm, 22 averages. Cisterna magna injection of Gadolinium-DTPA experiment: TR = 14.0 ms, TE = 5.22 ms, flip angle = 30°, 28 partitions, partition thickness = 0.5 mm, FOV = 80 x 80 mm, matrix size = 512 x 512, voxel size = 0.15 x 0.15 mm, 5 averages.

Data Processing and Statistics

Images were evaluated using the scanner software package (Syngo, SIEMENS, Erlangen, Germany). The spinal cord was outlined on axial slices and the mean signal was calculated. A second region of interest was placed outside the animal contours for noise measurement. Mean SNR and standard deviation (SD) were calculated for each slice. For the therapy experiment post-processing was performed by an observer blinded to the treatment. The signal to noise ratio (SNR) in the most proximal slice (figure 1c, position 3) was set to 100% and SNRs in consecutive slices scaled accordingly expressing relative SNR (%). The area under the curve (AUC) was calculated using the scanner software package (Syngo, SIEMENS, Erlangen, Germany). (The increase of Mn^{2+} uptake depending on the position was assessed by linear regression within the two groups. Correlations between MEMRI and behavioral tests were determined using Kendall's τ. BBB and grid walk scores in antibody-treated mice were compared to saline controls using the Wilcoxon rank sum test.

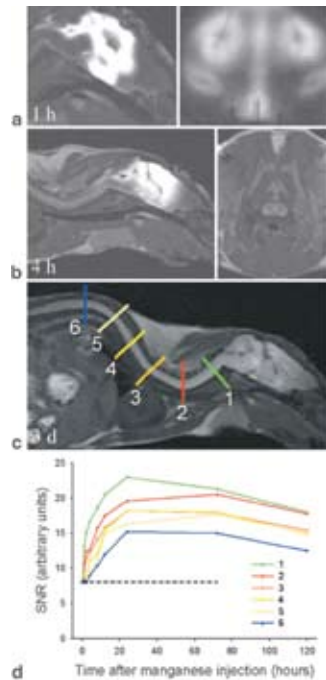ON CONNECTIVITY IN THE CENTRAL NERVOUS SYSTEM — A MAGNETIC RESONANCE IMAGING STUDY

MANGANESE-ENHANCED MAGNETIC RESONANCE IMAGING FOR IN VIVO ASSESSMENT OF DAMAGE AND FUNCTIONAL IMPROVEMENT FOLLOWING SPINAL CORD INJURY IN MICE

Figure 1 Contrast enhancement within the spinal cord after i.c.v.injection of MnCl2. (a) T1-weighted images in sagittal (left) and coronal orientation (right) at 1 h after injection. (b) Sagittal (left) and axial (right) T₁-weighted images at 4 h after injection. (c) Sagittal T1-weighted image showing homogeneous contrast enhancement within the spinal cord at 3 days after injection. (d) Time course of Mn2_ uptake at various levels of the spinal cord. The colored bars in (c) indicate the positions for the time course measurement corresponding to the following levels of the spinal cord: upper (1) and lower (2) cervical, upper (3), middle (4), and lower (5) thoracic, and upper (6) lumbar spinal cord. The dotted black line indicates baseline SNR.

Results

Intracerebroventricular MnCl$_2$ Injection Leads to Spinal Cord Enhancement

To test the suitability of an i.c.v. MnCl$_2$ solution injection for spinal cord imaging we measured the time course of Mn^{2+} enhancement after i.c.v. injection at various positions within the spinal cord. In the early time course, strong contrast enhancement was
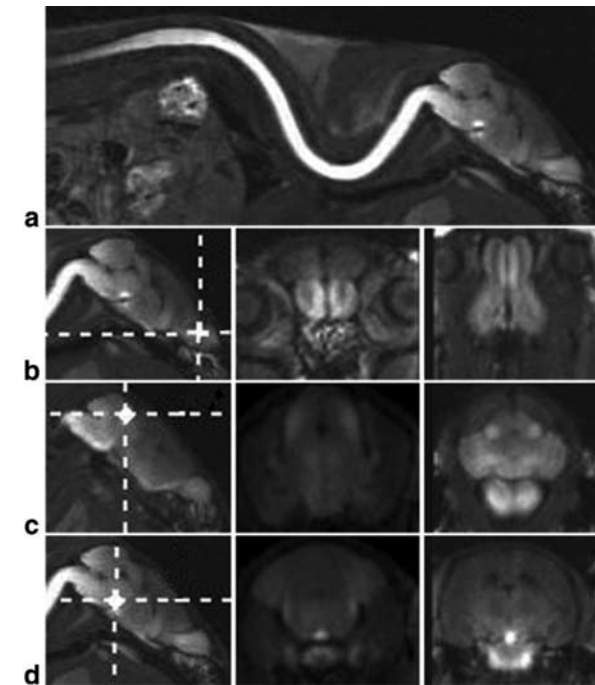
Figure 2 Injection of MnCl2 into the cisterna magna. (a) Sagittal T1-weighted image 24 h after injection into the cisterna magna. (b–d) From left to right sagittal, coronal and axial images at several levels in the brain. The level of the axial and coronal slices is indicated by the dotted white crosses on the sagittal images. Signal enhancement was observed in the rhinocortex (b), the colliculus superior (c), and the pituitary (d) as described previously (22). No significant Mn2- uptake in the motor cortex was observed.

observed in the motor cortex, along the ventricle walls and in both the ventral and the dorsal parts of the cervical spinal cord (figure 1a). Additionally, rapid transport over the CSF was noted with uptake both via the peri-spinal CSF as well as via the CSF within the central channel (figure 1b). Initially, Mn^{2+} was taken up into the spinal tissue directly adjacent to the figure but later the spinal cord showed homogenous Mn2+ distribution (figure 1c). The SNR within the spinal cord rose quickly in the first 24 h after injection. Afterwards, a plateau phase was reached that lasted another 48 h followed by a slow Mn^{2+} wash-out (figure 1d). This plateau reached different levels along the spinal cord with a clear

increase of SNR of two to three times baseline. Residual elevated signal intensity was present up to three weeks after injection, after which the SNR in the spinal cord returned to baseline. Direct injection of $MnCl_2$ solution into the cisterna magna gave rise to a rapid increase of signal primarily along the spinal cord suggesting a direct distribution of Mn2+ via the CSF (figure 2). Also, no uptake in the motor cortex was noted.

Concomitantly, we also tested the suitability of less invasive modes of $MnCl_2$ application. Systemic administration similarly leads to signal enhancement in the brain[6,21]. Mn^{2+} enters the brain primarily via the choroid plexus, from where it is distributed through the CSF into the parenchyma[6]. Thus, we examined Mn2+ uptake into the spinal cord after i.v. and s.c. application. The signal intensity within the spinal cord increased slightly, however, it was strongly reduced in comparison to the i.c.v. administration (data not shown), excluding such alternative routes of administration for examining the spinal cord.

Signal Enhancement is Reduced after SCI

After determining Mn^{2+} enhancement dynamics we tested the effect of SCI on Mn^{2+} uptake. We transected the dorsal 80% of the spinal cord at the level Th7/8, which led to paraplegia. MnCl2 solution was injected five weeks after SCI and imaging performed 60 h later since at that time point a homogeneous Mn2+ uptake at the lesion level could be expected (figure 1d). Contrast enhancement in the spinal cord is shown for representative mice without (figure 3a) and with injury (figure 3b) in the sagittal plane. A clear interruption of contrast enhancement distal to the lesion in the injured mouse can be seen as shown in more detail on the axial slices (figure 3c). To quantify functional impairment we determined SNR within the spinal cord on MRI images measured perpendicular to the spinal cord surrounding the lesion site (figure 3d). Uninjured animals displayed a homogeneous SNR throughout the spinal cord (blue curve in figure 3d); after $MnCl_2$ injection a marked increase in SNR was noted (green). Rostral to the lesion, injured mice (red) showed a SNR comparable to non-
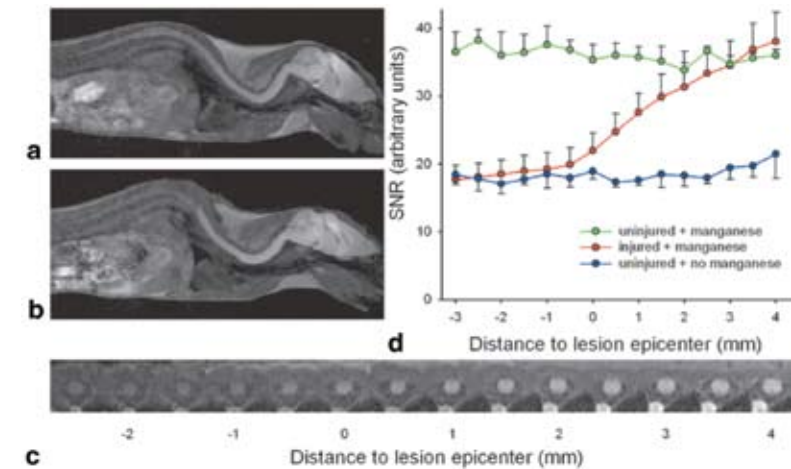
Figure 3 Visualization and quantification of SCI using MEMRI. (a) Continuous contrast enhancement throughout the spinal cord in an uninjured animal. (b) Clear interruption of contrast enhancement distal to the lesion site. Imaging was performed 60 h after SCI and MnCl2 injection. (c) Axial slices of the injured mouse shown in (b). Note the decrease in contrast enhancement around the lesion epicenter. (d) SNR (+/-SD) in the spinal cord of uninjured mice with and without MnCl2 injection (n = 5 per group) and injured mice (n = 10) 5 weeks after SCI. Distance in mm caudal (-) and rostral (+) to the lesion epicenter.

injured animals. Albeit moving further distal towards the lesion epicenter, the SNR gradually dropped approaching background levels at the lesion site and beyond. Thus, there is an injury-dependent reduction of Mn^{2+} uptake following SCI.

To examine whether the reduction of Mn^{2+} uptake is due to a compromised CSF circulation, we injected Gadolinium-DTPA into the cisterna magna of non-injured and SCI mice. Gadolinium-DTPA is a contrast agent that is mainly retained within the CSF[22,23]. In contrast to Mn^{2+}, Gadolinium-DTPA was in all cases detected within the CSF far beyond the site of the lesion, surrounding the lumbar spinal cord (figure 4). This excludes that the decreased Mn^{2+} uptake in injured mice is due to a compromised accessibility of the CSF to the spinal region caudal to the lesion.
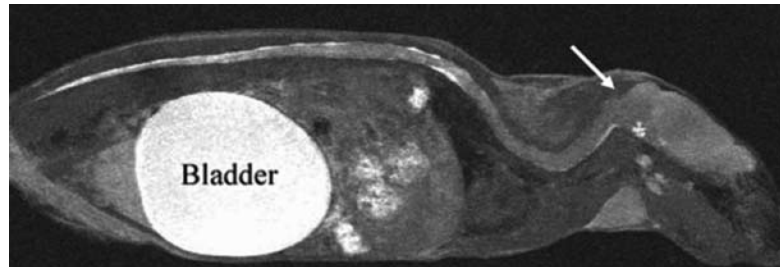
Figure 4 Gadolinium-DTPA injection into the cisterna magna of a spinal cord-injured mouse. Contrast is enhanced in the complete CSF, also caudal to the lesion epicenter. The arrow indicates the injection site.
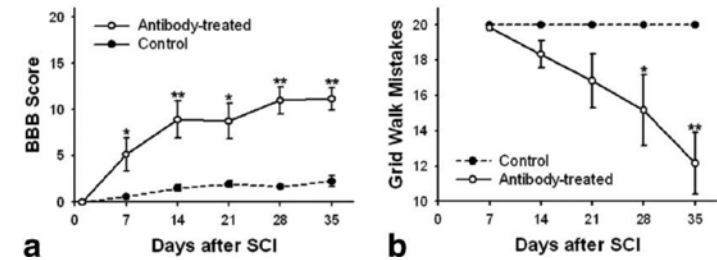

Figure 5 Clinical evaluation of motor function of antibody- and saline-treated mice following SCI. (a) BBB scores in antibody-treated (open circles) and untreated control (filled circles) animals (mean +/-SE; n = 6 per group). The overall locomotor performance significantly improved in the antibody-treated group, while only limited spontaneous recovery was observed in the saline control group (Wilcoxon rank sum test; *P < 0.05, **P > 0.01). (b) Number of grid walk mistakes in antibody-treated (open circles) and untreated control (filled circles) animals (mean +/-SE; n = 6 per group). The number of stepping mistakes significantly decreased in the treated group, while mice in the untreated control group did not regain the ability to step (Wilcoxon rank sum test; *P < 0.05, **P > 0.01).

Mn^{2+} Uptake Correlates with Functional Recovery following SCI

To test function-dependent Mn^{2+} uptake we performed MRI on mice treated with neutralizing antibodies directed against CD95Ligand and their saline-treated control counterparts. We have recently shown that this therapy protects neurons and oligodendrocytes from apoptotic cell death leading to enhanced axonal regeneration and improved functional recovery following SCI[17]. All animals were clinically tested once weekly using the BBB score[19] and a grid walk test[20]. In saline-treated animals minor signs of spontaneous locomotor function recovery were observed as shown before, whereas the anti-CD95Ligand antibody-treated mice improved significantly (figure 5)[17].

To evaluate therapy-induced changes in spinal Mn^{2+} uptake we performed the MEMRI experiment as described for the injured untreated animals. However, MnCl$_2$ solution was injected twice: at first at 4 h and for the second time at 5 weeks after SCI. Images were acquired 60 h later, and the SNR along the spinal cord was measured (figure 6a). We calculated the area under the curve (AUC) for both time points and tested the value of the change in AUC (Δ AUC) as a measure of clinical improvement. In saline-treated control animals Mn^{2+} uptake did not significantly increase with time (linear regression analysis of relative SNR (%) on the distance to the lesion epicenter: p = 0.018, slope -0.269, 95% confidence interval: -0.048 to -0.49, n=6). The relative SNR (%) at 3 d and at 5 weeks

after injury in a representative control animal is depicted in figure 6b together with the axial slices of the spinal cord of this mouse. In contrast, the anti-CD95Ligand antibody-treated animals showed a significant increase of Δ AUC (linear regression analysis: p = 0.0005, slope 1.150, 95% confidence interval: 0.831 to 1.470, n=6). In figure 6c the relative SNR (%) at 3 d and at 5 weeks after injury is shown for a representative treated animal. Importantly, at the early time point after SCI the MRI images of both groups were comparable. A gradual decrease of contrast enhancement along the rostro-caudal axis of the spinal cord was observed; reaching baseline levels at the lesion site, analogous to the curve of the injured untreated animals (compare figure 3). At the late time point, however, the images of treated and control mice differed strikingly. While in control animals the distribution of the Mn^{2+} signal had not changed in comparison to the early measurement, the contrast enhancement pattern was strongly changed in treated mice (figure 6c). Around and especially caudal to the lesion site the Mn^{2+} uptake was significantly increased, indicating preservation of active functional neurons at the level of injury and beyond. Yet, the SNR at and caudal to the lesion site never reached uninjured levels demonstrating residual damage despite treatment.
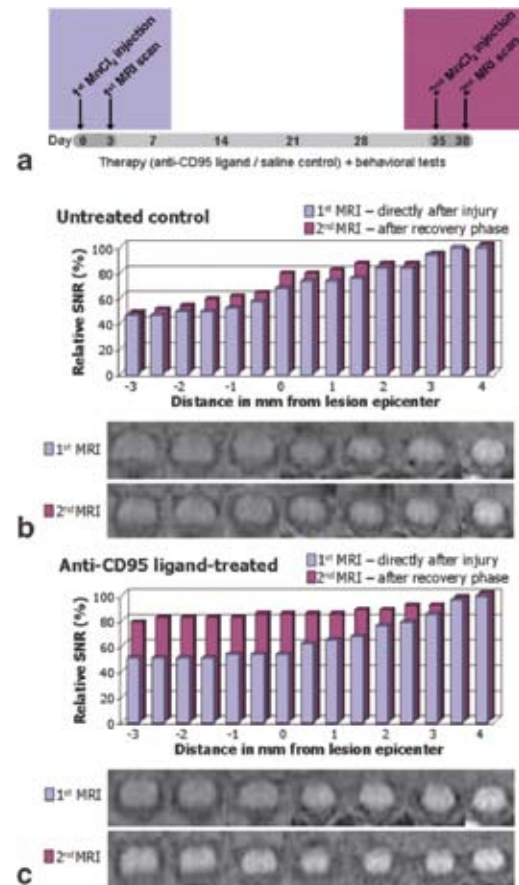
Figure 6 MEMRI for evaluation of therapy effects. (a) Schematic representation of the experiment. (b) Relative SNR (%) in the spinal cord directly after injury and 5 weeks later in a representative saline-treated animal. The axial slices depicted below were used for quantification. (c) Relative SNR (%) in a representative anti-CD95Ligand antibody-treated animal. Note the strong increase in contrast enhancement due to therapy.

The changes in Δ AUC between the early and late time points are plotted against the final behavioral test scores for both treated and control animals (figure 7). For testing the correlation of MEMRI with the clinical scores we ranked the 12 animals based on Δ AUC as well as on their behavioral test scores assuming that preservation of functional neurons is the cause for both increased
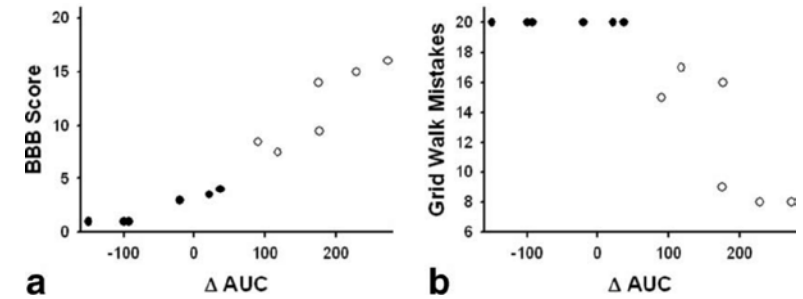

Figure 7 Correlation of MEMRI with behavioral tests for evaluation of therapy effects. The MEMRI-derived quantitative measure AUC for anti-CD95Ligand antibodytreated (open circles) and control mice (filled circles; n = 6 per group) is plotted against the clinical locomotor tests BBB score (a) and the number of mistakes in the grid walk test (b).

spinal Mn^{2+} uptake and improved motor function. A highly significant correlation between the two rankings was found (Kendall's τ = 0.9394, p = 0.000005). Furthermore, the antibody- and saline-treated groups differed significantly with regard to MEMRI as well as BBB and grid walk ranks (Wilcoxon rank sum test; p = 0.0011). In conclusion, MEMRI-derived parameters correlate closely with the clinical status as evaluated using locomotor tests.

Discussion

The main problem in SCI is the interruption of neuronal connections and consecutive loss of neuronal tissue. Despite the general lack of optimism for functional recovery after SCI, in the past decade animal studies brought forward evidence for neuroprotection, axonal regeneration and consequent regain of locomotion and of some primitive forms of sensation after experimental therapy [24,25]. This has led to a great debate about the type and quality of evidence needed to select truly promising candidate therapies. In most animal studies the reported therapeutical success is based upon histological evidence and/or assessment of the overall locomotor activity (e.g. BBB score). Major disadvantages of these methods are the need to sacrifice the animals, the great

ON CONNECTIVITY IN THE CENTRAL NERVOUS SYSTEM — A MAGNETIC RESONANCE IMAGING STUDY

MANGANESE-ENHANCED MAGNETIC RESONANCE IMAGING FOR IN VIVO ASSESSMENT OF DAMAGE AND FUNCTIONAL
IMPROVEMENT FOLLOWING SPINAL CORD INJURY IN MICE

subjectivity and subsequent lack of standardization among the different laboratories. Here we developed an *in vivo* method for the evaluation of spinal cord function using MEMRI. This method has the important advantage of enabling a standardized and more objective follow-up of therapies over time.

The use of MEMRI for the functional assessment after SCI relies on the capacity of Mn^{2+} to mimic Ca^{2+}. Mn^{2+} is predominantly taken up by active neurons and less by the disconnected "electrically silent" ones. The rate of axonal Mn^{2+} transport described within the brain varies from 1.1 to 6.0 mm/h depending on injection volume and functional status of the neuronal tissue[26]. Signal propagation in our experiment was much faster than that calculated for axonal transport. Moreover, experiments have shown that a focal $MnCl_2$ injection into the motor cortex leads to uptake in the corticospinal tract with strong signal decay in the more distal regions of the corticospinal tract without detectable contrast enhancement beyond the midbrain level[26]. This indicates that in our setting visualization of the spinal cord using MEMRI is based on transport of Mn^{2+} via the CSF with local, activity-dependent uptake into the spinal cord. This hypothesis is strengthened by the experiment, in which $MnCl_2$ was injected directly into the cisterna magna. Here, we did not observe uptake in the motor cortex excluding a substantial role for active axonal Mn^{2+} transport via the corticospinal tract as a main route of contrast enhancement of the spinal cord. Instead, a strong contrast enhancement throughout the spinal cord resembling the contrast enhancement after an i.c.v. injection was evident. These findings are in accordance with a recent paper investigating i.p. application of $MnCl_2$ showing uptake only in selected areas of the brain (27). Altogether, our results indicate that MEMRI of the spinal cord after i.c.v. injection is primarily based on the CSF transport of Mn^{2+} and local activity-dependent uptake.

Injury to the spinal cord, especially in the transection model used here, may affect the integrity of CSF circulation[28]. Thus, it might be hypothesized that the near-background levels of Mn^{2+} uptake caudal to the lesion site found in mice directly after injury or in untreated mice five weeks after injury could be due to a block in CSF circulation. However, it is unlikely that the anti-

CD95Ligand therapy acts on this level. Nevertheless, to exclude the possibility that our method merely depicts disruption of the CSF system, we injected Gadolinium-DTPA into the cisterna magna. In all injured and uninjured control mice the contrast agent passed beyond the level of the lesion site into the lumbar spinal cord to a comparable extent. These experiments indicate that transecting the dorsal 80% of the spinal cord – although inducing local damage to the CSF compartment – does not lead to a complete disruption of the CSF circulation. Thus, the specific contrast enhancement and lack of uptake caudal to the lesion site cannot be attributed to impeded CSF circulation.

A recent publication describes Mn^{2+} uptake in the hemi-sected spinal cord of rats after a local injection of $MnCl_2$ solution into the white matter of the spinal cord[16]. The authors discuss their findings exclusively in terms of axonal transport but their images reveal an even stronger Mn^{2+} uptake in the gray matter of the spinal cord than in the surrounding white matter, which indicates that in their experiments primary uptake by functional gray matter, as described in our setting, must also play a strong role. Moreover, in our experiments injection-induced trauma is minimized because an invasive and technically challenging focal injection into the white matter of the spinal cord requiring an additional laminectomy is not necessary. This is crucial for therapy monitoring since additional trauma to the spinal cord makes it more difficult to objectively determine therapy efficacy. Finally, the major advantage of our MEMRI approach is the possibility of quantitative assessment of damage and recovery.

An issue using Mn^{2+} for *in vivo* imaging is its neurotoxicity[29]. In contrast to focal injections into the brain parenchyma, an injection of $MnCl_2$ into the CSF has the advantage of rapid dilution of the toxic agent. Furthermore, in the experiments described here we stayed well within the limits of the known non-toxic dose[30]. Consequently, no alterations of vital or motor functions could be observed following i.c.v. $MnCl_2$ injection. Symptoms of manganism that resemble disorders described as extrapyramidal motor system dysfunction, which are typical for chronic Mn^{2+} exposure, did not develop[31].

188

189

ON CONNECTIVITY IN THE CENTRAL NERVOUS SYSTEM — A MAGNETIC RESONANCE IMAGING STUDY

MANGANESE-ENHANCED MAGNETIC RESONANCE IMAGING FOR IN VIVO ASSESSMENT OF DAMAGE AND FUNCTIONAL IMPROVEMENT FOLLOWING SPINAL CORD INJURY IN MICE

Conclusion

We have devised a fast and safe *in vivo* method for visualization of the spinal cord and quantitative assessment of its functional status. Moreover, we demonstrated that MEMRI could substitute for behavioral tests or at least add to a more objective assessment of the spinal cord's functional status following SCI. This method could become a standard measurement for comparison of different therapies in different laboratories. MEMRI provides a surrogate read-out for damage and functional recovery after SCI. Finally, application of this method could be expanded to the study of other pathologies both in the CNS and the PNS.
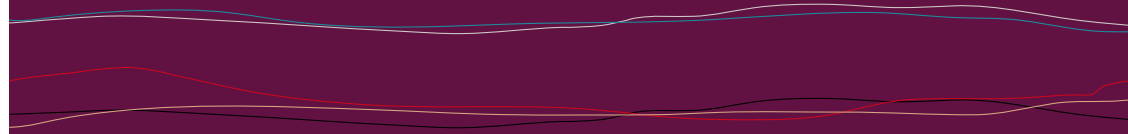
Acknowledgements

References

1   **Jones EG,** Powell TP. An anatomical study of converging sensory pathways within the cerebral cortex of the monkey. Brain 1970;93(4):793-820.

2   **Heimer L,** Robarts M. Neuroanatomical Tract-Tracing Methods. 1981. New York L, Plenum Press.

3   **Lin YJ,** Koretsky AP. Manganese ion enhances T1-weighted MRI during brain activation: an approach to direct imaging of brain function. Magn Reson Med 1997 Sep;38(3):378-88.

4   **Drapeau P,** Nachshen DA. Manganese fluxes and manganese-dependent neurotransmitter release in presynaptic nerve endings isolated from rat brain. J Physiol 1984 Mar;348:493-510.

5   **Koretsky AP,** Silva AC. Manganese-enhanced magnetic resonance imaging (MEMRI). NMR Biomed 2004 Dec;17(8):527-31.

6   **Aoki I,** Wu YJ, Silva AC, Lynch RM, Koretsky AP. *In vivo* detection of neuroarchitecture in the rodent brain using manganese-enhanced MRI. Neuroimage 2004 Jul;22(3):1046-59.

7   **Watanabe T,** Natt O, Boretius S, Frahm J, Michaelis T. *In vivo* 3D MRI staining of mouse brain after subcutaneous application of MnCl2. Magn Reson Med 2002 Nov;48(5):852-9.

8   **Van der Linden A,** Verhoye M, Van Meir V, Tindemans I, Eens M, Absil P, Balthazart J. *In vivo* manganese-enhanced magnetic resonance imaging reveals connections and functional properties of the songbird vocal control system. Neuroscience 2002;112(2):467-74.

9   **Tindemans I,** Verhoye M, Balthazart J, Van der Linden A. *In vivo* dynamic ME-MRI reveals differential functional responses of RA- and area X-projecting neurons in the HVC of canaries exposed to conspecific song. Eur J Neurosci 2003 Dec;18(12):3352-60.

10 **Pautler RG,** Silva AC, Koretsky AP. *In vivo* neuronal tract tracing using manganese-enhanced magnetic resonance imaging. Magn Reson Med 1998 Dec;40(5):740-8.

11 **Saleem KS,** Pauls JM, Augath M, Trinath T, Prause BA, Hashikawa T, Logothetis NK. Magnetic resonance imaging of neuronal connections in the macaque monkey. Neuron 2002 May;34(5):685-700.

12 **Pautler RG,** Mongeau R, Jacobs RE. *In vivo* trans-synaptic tract tracing from the murine striatum and amygdala utilizing manganese enhanced MRI (MEMRI). Magn Reson Med 2003 Jul;50(1):33-9.

13 **Spenger C,** Josephson A, Klason T, Hoehn M, Schwindt W, Ingvar M, Olson L.

190

191

ON CONNECTIVITY IN THE CENTRAL NERVOUS SYSTEM — A MAGNETIC RESONANCE IMAGING STUDY

MANGANESE-ENHANCED MAGNETIC RESONANCE IMAGING FOR IN VIVO ASSESSMENT OF DAMAGE AND FUNCTIONAL IMPROVEMENT FOLLOWING SPINAL CORD INJURY IN MICE

Functional MRI at 4.7 tesla of the rat brain during electric stimulation of forepaw, hindpaw, or tail in single- and multislice experiments. Exp Neurol 2000 Dec;166(2): 246-53.

14 **Lawrence J,** Stroman PW, Bascaramurty S, Jordan LM, Malisza KL. Correlation of functional activation in the rat spinal cord with neuronal activation detected by immunohistochemistry. Neuroimage 2004 Aug;22(4):1802-7.

15 **Nevo U,** Hauben E, Yoles E, Agranov E, Akselrod S, Schwartz M, Neeman M. Diffusion anisotropy MRI for quantitative assessment of recovery in injured rat spinal cord. Magn Reson Med 2001 Jan;45(1):1-9.

16 **Bilgen M,** Dancause N, Al Hafez B, He YY, Malone TM. Manganese-enhanced MRI of rat spinal cord injury. Magn Reson Imaging 2005 Sep;23(7):829-32.

17 **Demjen D,** Klussmann S, Kleber S, Zuliani C, Stieltjes B, Metzger C, Hirt UA, Walczak H, Falk W, Essig M, Edler L, Krammer PH, Martin-Villalba A. Neutralization of CD95 ligand promotes regeneration and functional recovery after spinal cord injury. Nat Med 2004 Apr;10(4):389-95.

18 **Furlan R,** Pluchino S, Marconi PC, Martino G. Cytokine gene delivery into the central nervous system using intrathecally injected nonreplicative viral vectors. Methods Mol Biol 2003;215:279-89.

19 **Basso DM,** Beattie MS, Bresnahan JC. A sensitive and reliable locomotor rating scale for open field testing in rats. J Neurotrauma 1995 Feb;12(1):1-21.

20 **Metz GA,** Merkler D, Dietz V, Schwab ME, Fouad K. Efficient testing of motor function in spinal cord injured rats. Brain Res 2000 Nov;883(2):165-77.

21 **Kuo YT,** Herlihy AH, So P W, Bhakoo KK, Bell JD. In vivo measurements of T1 relaxation times in mouse brain associated with different modes of systemic administration of manganese chloride. J Magn Reson Imaging 2005 Apr;21(4):334-9.

22 **Liu CH,** D'Arceuil HE, de Crespigny AJ. Direct CSF injection of MnCl(2) for dynamic manganese-enhanced MRI. Magn Reson Med 2004 May;51(5):978-87.

23 **Wan XM,** Fu TC, Smith PH, Brainard JR, London RE. Magnetic resonance imaging study of the rat cerebral ventricular system utilizing intracerebrally administered contrast agents. Magn Reson Med 1991 Sep;21(1):97-106.

24 **Klussmann S,** Martin-Villalba A. Molecular targets in spinal cord injury. J Mol Med 2005 Sep;83(9):657-71.

25 **Schwab ME.** Increasing plasticity and functional recovery of the lesioned spinal cord. Prog Brain Res 2002;137:351-9.

26 **Leergaard TB,** Bjaalie JG, Devor A, Wald LL, Dale AM. In vivo tracing of major rat brain pathways using manganese-enhanced magnetic resonance imaging and three-dimensional digital atlasing. Neuroimage 2003 Nov;20(3):1591-600.

27 **Yu, X,** Wadghiri, YZ, Sanes, DH, Turnbull, DH. In vivo auditory brain mapping in mice with Mn-enhanced MRI. Nat Neurosci. 2005 Jul; 8(7):961-8

28 **Falcone S,** Quencer RM, Green BA, Patchen SJ, Post MJ. Progressive posttraumatic myelomalacic myelopathy: imaging and clinical features. AJNR Am J Neuroradiol 1994 Apr;15(4):747-54.

29 **Keen CL,** Ensunsa JL, Clegg MS. Manganese metabolism in animals and humans including the toxicity of manganese. Manganese and its Role in Biological Processes. 2000. New York, Marcel Dekker.

30 **Crossgrove J,** Zheng W. Manganese toxicity upon overexposure. NMR Biomed 2004 Nov;17(8):544-53.

31 **Donaldson J.** The physiopathologic significance of manganese in brain: its relation to schizophrenia and neurodegenerative disorders. Neurotoxicology 1987;8(3):451-62

192

193

ON CONNECTIVITY IN THE CENTRAL NERVOUS SYSTEM — A MAGNETIC RESONANCE IMAGING STUDY

MANGANESE-ENHANCED MAGNETIC RESONANCE IMAGING FOR IN VIVO ASSESSMENT OF DAMAGE AND FUNCTIONAL IMPROVEMENT FOLLOWING SPINAL CORD INJURY IN MICE

Summary

DTI

Diffusion Tensor Imaging (DTI) is a technique that can characterize the spatial properties of molecular water diffusion, also named Brownian motion. Water diffusion or Brownian motion is the random motion of water molecules due to thermal energy present at temperatures above 0 Kelvin. When no directionally ordered boundaries are present, this water motion over time can be described by a sphere, and is called isotropic. The size of this sphere, quantitatively described by the apparent diffusion coefficient (ADC), is determined by the amount of motion restriction. For instance in highly cellular tumors, this restriction is limited and the corresponding ADC is low whereas in areas of tissue necrosis, the water motion is not impeded by cellular structure and the corresponding ADC is high.

The application of DTI to the brain revealed that these spatial properties are anisotropic in white matter (WM). The term anisotropy describes the deviation of the water motion from this sphere shape and the directionality of the resulting ellipsoid has been attributed to highly directionally ordered structures like axons and myelin sheets. Using DTI, both the magnitude of anisotropy and the preferential direction of water diffusion can be quantified. The preferential direction can be described by a vector and these vectors can be connected to generate 3-dimensional fiber tracts. The magnitude of anisotropy can be quantified and is described by the fractional anisotropy (FA). The FA-value ranges between 0 and 1, where 0 represents a perfect sphere and 1 an endlessly long ellipsoid.

In chapter 2 and 3 we showed that, using DTI-based fiber tracking, fiber trajectories both in the brain stem and in the brain hemispheres can be reconstructed and are consistent with knowledge from *post mortem* anatomy. At the brainstem level (chapter 2), it was possible to identify the cortico-spinal tract (CST), the medial lemniscus, and the superior, medial, and inferior cerebellar peduncles. In addition, the cerebral peduncle could be subparcellated into component tracts, namely, the frontopontine tract, the CST, and the temporo-/parieto-/occipitopontine tract. In the cerebrum, we could successfully reconstruct the cores

of several long-association fibers, including the anterior (ATR) and posterior (PTR) thalamic radiations, and the uncinate (UNC), superior longitudinal (SLF), inferior longitudinal (ILF), and inferior fronto-occipital (IFO) fasciculi. An important observation from our first DTI study on the brain stem (chapter 2) was, that when tract reconstruction parameters were changed, the result of the fiber tracking was influenced significantly. Reconstruction parameters include the minimum FA and the angle between two vectors in adjacent voxels. We could show that for the reconstruction of each fiber tract, optimal initial parameters could be found. With an FA threshold of 0.25-0.35, and an angular threshold of 0.75 or higher, the identified trajectories were likely to be valid and relatively reproducible. Nonetheless, a certain user bias remained present.

In chapter 3 we described a similar approach for reconstruction of association tracts in the cerebrum. Furthermore, we tried to address the challenge of intra-individual variation. To analyze normal and pathological variations in patterns of these reconstructed axonal tracts, we generated statistical maps for each tract system. To achieve this, we standardized ten individual brains into the Talairach coordinate brain reference frame using elastic warping, overlaid the normalized tracts and calculated the amount of overlap. Thus we could determine a normalized fiber core, with high levels of overlap, and increased variation in the more peripheral branches. This method offered a more generalized approach for the evaluation of fiber tracts in normal development and disease, but may also confound small changes due to the normalization process.

In chapter 2, 3 and 4 we also showed the first potential clinical applications of DTI. In chapter 2 we demonstrated how DTI may aid the planning of neurosurgical procedures. In a patient with a meningioma, we showed a clear deviation of the cortico-spinal tract which was not visible on conventional imaging. In chapter 3, we demonstrated that DTI can detect small changes in fiber integrity in neurodegenerative diseases. In a case of X-linked Adrenoleukodystropy we observed selective involvement of the corpus callosum using DTI, which correlated with neuropsychological findings. In chapter 4, we studied the effect of primary brain tumors on white matter anatomy. By comparing two patients, we could see different effects such as dislocation with low

probability of infiltration and at another location infiltration without an apparent effect on fiber orientation. It must be noted however, that we could not conclude whether T_2 hyperintensity along fiber tracts indicated infiltrating tumor or Wallerian degeneration. Thus, for the evaluation of tract infiltration more detailed and reproducible methods for quantification of fiber integrity need to be developed.

As discussed before, the methods for fiber visualization and measurement of fiber integrity suffer from user induced variability. Although we could show that DTI has the potential to yield additional information on fiber integrity and loss of organization in disease, this user-dependent variance reduces the sensitivity of the method to small changes in fiber integrity. In chapter 5, we described a novel method of depiction of fiber direction and introduced a reproducible region of interest (ROI) based fiber clustering. Based on anisotropy properties, a large ROI is clustered in fiber, partial volume and non-fiber automatically. We showed that using this method, user variability due to ROI placement was minimized. In chapter 6 we further evaluated the reproducibility of this method and applied it to the evaluation of the infiltration pattern in primary brain tumors. The proposed quantification method proved to be highly reproducible both in healthy controls and patients. Fiber integrity in the corpus callosum was measured using this quantification method and the profiles of fractional anisotropy provided additional information of the possible extent of infiltration of primary brain tumors compared to conventional imaging. This yielded additional information on the nature of ambiguous contra lateral lesions in patients with primary brain tumors. The results showed that DTI derived parameters can be determined reproducibly and may have a strong impact on evaluation of contra lateral extent of primary brain tumors. In chapter 7 we applied the same method, previously employed in the corpus callosum, to the cortico-spinal tract (CST). We could demonstrate that the evaluation method was also suited for DTI quantification in another tract besides the corpus callosum. The processing time is relatively low, and a high reproducibility and stability could be shown. Furthermore, we could show that using this method, degeneration of the cortico-spinal tract in

Amyotrophic Lateral Sclerosis (ALS) could be quantified.

Methods for performing brain DTI are relatively well established, but DTI of the spinal cord is still challenging due to the required high resolution, the susceptibility differences between the adjacent tissue, and the pulsation of the surrounding cortico spinal fluid (CSF). The development of a robust, reproducible assessment of spinal cord fiber integrity could be of great clinical interest for neurodegenerative diseases like multiple sclerosis or spinal cord injury. In chapter 8, we introduced an improved pulse sequence for spinal cord imaging. Compared to conventional inner volume (IV) techniques and previously published (IV-techniques with magnetization restoration, the approach we proposed was more signal-efficient and allows the usage of a twice-refocused spin echo diffusion preparation which diminishes eddy current induced image distortions. We could show that this sequence constantly yielded compelling image quality.

Furthermore, we could show that using the aforementioned quantification method (chapter 5), FA evaluation was stable at the full length of the cervical spine, the evaluated FA and ADC values of the same subject varied by less than 4.5% when combining both rescan and re-evaluation induced variability. Also, it was shown that the measured FA of the spine in a patient with acute ischemic spinal cord injury was markedly decreased. Hence, the FA may be a surrogate marker for spinal cord integrity and may serve as an indicator for final outcome after spinal trauma.

MEMRI

Manganese ions (Mn^{2+}) are known to cause a shortening of the T_1 time of water protons in MRI leading to a strong contrast enhancement in T_1-weighted MRI. Mn^{2+} has chemical properties resembling those of calcium ions (Ca^{2+}). Thus, it is actively transported into neurons via voltage-gated Ca^{2+} channels. Manganese enhanced magnetic resonance imaging (MEMRI) has been used successfully for the visualization of neuronal circuits and activity patterns of the brain in different animal models. Although MEMRI is an established method for studies

of the animal brain, the application of MEMRI to the spinal cord remained to be developed. We hypothesized that an intraventricular injection of $MnCl_2$ would lead to Mn^{2+} uptake by the spinal cord with the amount of Mn^{2+} uptake depending on the spinal cord's functional status. We were able to demonstrate that MEMRI can be used as a reliable method for *post mortem* depiction and quantification of spinal cord contusion injuries in rats (chapter 9). As MRI features of lesion quantification correlated closely with results of clinical assessment of motor function, MEMRI yielded a measure of functional imaging of the rat spinal cord integrity and level of spinal cord injury, in addition to providing structural depiction of the spinal cord.

In chapter 10, we implemented the same method for imaging the murine spinal cord. We could show that MEMRI may serve as an *in vivo* method for visualization of the spinal cord in mice and that it enabled quantitative assessment of its functional status. Moreover, we demonstrated that MEMRI could substitute behavioural tests or at least add to a more objective assessment of the murine spinal cord's functional status following spinal cord injury. Also, we could show that MEMRI can monitor therapy effects in experimental spinal cord treatment thus yielding an objective parameter for the evaluation of the efficacy of treatment.

Concluding remarks

In this thesis we demonstrated that MRI can be used for the detection of axonal tracts both in animal models and in the human brain. The proposed techniques offer a unique insight into the white matter connections of the brain.

Using MEMRI, both white matter tracts as well as functional grey matter could be depicted. Since Mn^{2+} is only transported into vital neuronal tissue, it is a true surrogate marker for neuronal integrity in the spinal cord. Thus, as we could demonstrate, it can serve as an *in vivo* marker for experimental therapy of spinal cord injury. Now, other groups have adapted this approach and it may evolve as a standard laboratory test for the pre-clinical *in vivo* and *post mortem* evaluation of experimental drugs for treatment of

spinal cord injury in animal models. However, due to the known neurotoxicity of Mn^{2+}, human applications in this form are unlikely.

The interpretation of human *in vivo* DTI data in is more complicated. Although we could demonstrate the feasibility of the reconstruction of fiber tracts using DTI data, we could also show that the representation of this data strongly depends on the intrinsic settings of fiber tracking algorithms. This may not have strong consequences for neuroscience research, but in a clinical environment, e.g. as a method for intraoperative planning, accuracy is paramount.

Also, for quantitative measures describing the fiber integrity derived from DTI data, a similar problem arises. Whereas Mn^{2+} is a true marker of vitality of neuronal tissue, parameters such as the fractional anisotropy (FA) are reflecting the underlying tissue microstructure rather than its vitality. We could show that the FA is a sensitive parameter for the detection of infiltration of gliomas in surrounding brain tissue, but the evaluation is so far limited to defined regions of fiber tracts.

A current line of research is aiming at generating three-dimensional maps of the infiltration likelihood. Such an approach is clearly desirable but is hampered by several limitations of DTI. First, in crossing regions, in using the tensor model, the FA is artificially low as it would be due to tumor infiltration thus leading to ambiguity. Also, mass effects of the tumor may lead to an initial increase of FA followed later by a decrease as a late effect of Wallerian degeneration. Thus, such tracts would initially be classified as not affected but may already be functionally impaired. Another confounding effect may result from oedema. In the presence of moderate tumor associated oedema, the measured FA may be reduced without a true structural change in white matter architecture. This may lead to the false assumption that in these regions, white matter tracts may be infiltrated.

In conclusion, caution is needed considering the evaluation of DTI derived parameters of fiber integrity. Nonetheless, DTI yields valuable information on fiber integrity and is a valuable tool for studies of normal and pathological brain development, neuronal degeneration and for the evaluation of gliomas.

Nederlandse samenvatting

DTI
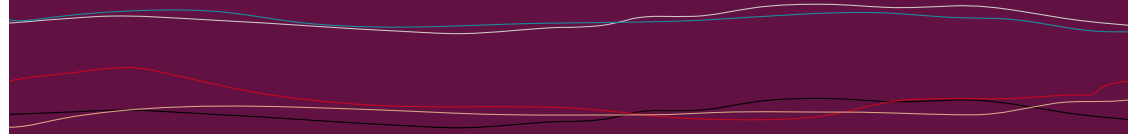
Diffusion tensor imaging (DTI) is gebaseerd op de Brownse molecuulbewegingen van voornamelijk aan water gebonden protonen. Deze beweging beschrijft het fenomeen, dat door de aanwezige thermische energie, waterdeeltjes op microscopisch niveau vrij bewegen. Deze vrije beweging geldt echter alleen als er geen structuren aanwezig zijn die deze beweging belemmeren. In weefsel zorgt de aanwezigheid van structuren zoals celwanden ervoor, dat deze bewegelijkheid niet vrij is. Hoe meer deze beweging belemmerd wordt, des te kleiner is de middels DTI te meten apparent diffusion coëfficiënt (ADC), een maat voor de bewegelijkheid van deze deeltjes. In tumoren met een sterke groei, bijvoorbeeld, liggen cellen dicht op elkaar en is de gemeten ADC klein, terwijl in gebieden met necrose zonder celstructuren, de ADC hoog is.

In tumoren is de ADC in grote mate onafhankelijk van de richting waarin de ADC gemeten wordt, het deeltje kan zich in alle richtingen ongeveer even sterk bewegen. De diffusie is bolvormig en wordt als isotroop beschreven. In de hersenen, vooral in zenuwbanen, is deze bewegelijkheid echter anisotroop of ellipsoïde. Dit richtingsafhankelijke bewegingsprofiel wordt toegeschreven aan de aanwezigheid van axonen en myeline. De langste as van deze ellips verloopt parallel aan de richting van de zenuwbanen. Hoe langer en dunner de ellips, des te dichter liggen de zenuwbanen op elkaar. De vorm van het diffusiepatroon, van bolvormig tot een oneindig lange ellips, wordt beschreven door de fractional anisotropy (FA). Deze FA heeft een waarde van nul tot één, waar nul een bol, en één een oneindig lange ellips representeert. Zo kan door middel van DTI zowel de axonale oriëntering als ook de integriteit van zenuwbanen worden bepaald.

In hoofdstuk 2 en 3 toonden we aan, dat door middel van detectie van zenuwbanen op basis van DTI, ook fiber tracking genoemd, zenuwbanen in de hersenstam en het cerebrum kunnen worden gereconstrueerd. Met behulp van deze techniek konden we de volgende banen visualiseren: tractus cortico-spinalis, lemniscus medialis, pedunculus cerebelli inferior, medialis en superior op het niveau van de hersenstam. Verder konden we binnen de pedunculus cerebri de tractus fronto-pontinis, tractus cortico-spinalis en de tractus temporalis, parietalis en occipitalis onderscheiden. In het cerebrum konden we volgende banen visualiseren: de radiatio thalamica anterior en posterior, de uncus, de fasciculus longitudinalis superior en inferior en de fasciculus fronto-occipitalis.

Een belangrijke observatie uit deze eerste publicaties was, dat de gevonden vorm van een zenuwbaan sterk afhankelijk is van de gebruikte techniek. Relevante parameters zijn ondermeer de minimale FA en de hoek tussen twee op elkaar aansluitende vectoren. Deze twee factoren werden onderzocht en optimale waarden voor de reconstructie werden gevonden. Met een minimale FA tussen 0,25-0,35 en een hoekverhouding › 0,75 konden relatief valide en reproduceerbare resultaten worden behaald. De vorm van de gevonden zenuwbaan blijft echter sterk afhankelijk van de door de gebruiker gebruikte instellingen.

In hoofdstuk 3 gebruikten we dezelfde methode voor de reconstructie van zenuwbanen in de hersenen. Hier trachtten we ook een mogelijkheid te vinden om normale intra-individuele variatie te onderscheiden van pathologische veranderingen. We ontwikkelden een methode voor standaardisering van DTI data in de Talaraich ruimte door middel van elastische registratie. Na deze normalisatie berekenden we de mate van overlap in gezonde proefpersonen en konden zo sterk vertegenwoordigde kernbanen en grotere variatie in de periferie van de hersenen vaststellen. Deze methode biedt de mogelijkheid om verschillende populaties te vergelijken en zo verschillen tussen gezond en pathologisch weefsel te herkennen. Door de normalisatie kunnen kleine veranderingen echter ook gemaskeerd worden.

In hoofdstuk 2, 3 en 4 komen ook de eerste potentiele klinische toepassingen van DTI aan bod. In hoofdstuk 2 lieten we, aan de hand van een patiënt met een meningioom, zien dat DTI een verschuiving van zenuwbanen zichtbaar kan maken, hetgeen kan helpen bij de planning van neurochirurgische ingrepen. In hoofdstuk 3 lieten we zien, dat het in principe mogelijk is met behulp van DTI door adrenoleukodystrofie veroorzaakte kleine veranderingen in de integriteit van zenuwbanen te meten.

In hoofdstuk 4 bestudeerden we de verschillende effecten van hersentumoren op de organisatie van het omliggende hersenweefsel. Door patiënten met elkaar te vergelijken, konden we verschillen vaststellen tussen verplaatsing van normaal hersenweefsel met een kleine waarschijnlijkheid op infiltratie en infiltratie zonder noemenswaardige verplaatsing. Een eenduidig verschil tussen infiltratie en Wallerse degeneratie kon echter niet worden gemaakt. Ook bleek het noodzakelijk, voor de detectie van minimale veranderingen in de integriteit van zenuwbanen, een betere methode voor de kwantificatie te ontwikkelen.

In hoofdstuk 5 beschreven we een nieuw ontwikkelde stabiele kwantificatie methode. Hiervoor wordt in een ruime region-of-interest (ROI) een clustering toegepast waarmee automatisch deze ROI wordt verdeeld in zenuwbaan, partieel volume en niet-zenuwbaan. We konden laten zien dat met deze methode de door de operator geïntroduceerde variatie sterkt kan worden gereduceerd. In hoofdstuk 6 evalueerden we deze variatie verder en pasten de methode toe om infiltratiepatronen van hersen-tumoren beter te kunnen beschrijven. We vonden, dat door metingen aan het corpus callosum, de verbreiding van de tumor beter kon worden beoordeeld dan op basis van conventionele MRI. Dit hielp ook om de aard van onduidelijke contralaterale lesies beter te identificeren. In hoofdstuk 7 evalueerden we dezelfde methode die we eerder toepasten in het corpus callosum (hoofdstuk 5 en 6) in de tractus cortico-spinalis. Ook hier bleek de methode een grote reproduceerbaarheid te bezitten en was het mogelijk om bij patiënten met amyotrofe lateraal sclerose degeneratieve veranderingen vast te stellen.

Methoden voor DTI van de hersenen zijn inmiddels wijd verbreid. DTI van het ruggenmerg daarentegen is nog steeds een grote uitdaging vanwege de inhomogeniteit van het lokale magneetveld, de benodigde resolutie en pulsatie van liquor cerebrospinalis. De toepassing van DTI bij multiple sclerose (MS) of spinaal trauma zou van grote klinische betekenis kunnen zijn mits deze problemen kunnen worden opgelost. In hoofdstuk 8 introduceerden we een nieuwe meetmethode voor DTI van het ruggenmerg. We lieten zien dat de voorgestelde methode duidelijk efficiënter is dan bestaande methoden wat betreft

SNR. Hierdoor is een hogere resolutie voor de afbeelding van het ruggenmerg mogelijk. Verder konden we aantonen dat de toegepaste methode ongevoelig is voor liquorpulsaties en veldinhomogeniteit. Ook konden we de integriteit van het gehele cervicale ruggenmerg bepalen en in kombinatie met de bovengenoemde kwantificatiemethode (hoofdstuk 5) bedroeg de gezamenlijke variatie van gemeten FA maximaal 4,5%. Deze methode werd toegepast bij een patiënt met spinaal trauma waar een significante afname van de FA aangetoond kon worden. Daarmee lijkt het mogelijk te zijn de FA te gebruiken als surrogaat parameter om de prognose van spinaal trauma te voorspellen.

MEMRI

Contrastmiddel wordt in de radiologie zeer algemeen ingezet, bijvoorbeeld om tumoren beter zichtbaar te maken. Het effect van een contrastmiddel is daarbij gebaseerd op de interactie van het element Gadolinium met water in de omgeving. Door deze interactie wordt de zogenaamde T_1-tijd van weefsel verkort, waardoor dit weefsel in een MRI scan zeer contrastrijk, en daardoor goed herkenbaar wordt. Gadolinum is in een groot complex gebonden en wordt voornamelijk in weefsel opgenomen waar de bloedvaten lekken, zoals in tumoren.

Een ander element dat in principe dezelfde werking heeft als Gadolinium is Mangaan (Mn^{2+}). Ook Mn^{2+} veroorzaakt een verkorting van de T_1-tijd van protonen en kan zodoende als contrastmiddel worden ingezet. Het interessante is, dat Mn^{2+} als ion zeer klein is en direct in cellen kan worden opgenomen, iets wat met een Gadolinium-complex niet mogelijk is. Mn^{2+} is een divalent ion met chemische eigenschappen die lijken op die van Ca^{2+}. Het wordt daardoor actief in neuronen opgenomen via calciumkanalen, die Ca^{2+} de neuronen in pompen om neurotransmitters af te geven. Op basis van deze eigenschappen wordt manganese enhanced magnetic resonance imaging (MEMRI) voor de beeldvorming van neuronale verbindingen en voor de afbeelding van functioneel actieve hersengebieden in verschillende diermodellen benut. Omdat grote doses Mn^{2+}

neurotoxisch zijn, wordt deze methode uitsluitend bij proefdieren toegepast.

In de hersenen wordt MEMRI al enige tijd benut, maar voor het ruggenmerg was deze methode nog niet ontwikkeld. We veronderstelden dat, wanneer $MnCl_2$ in de liquor wordt geïnjecteerd, Mn^{2+} in het ruggenmerg wordt opgenomen en dat de hoeveelheid opgenomen Mn^{2+} correleert met de functionele status van het ruggenmerg.

In onze initiële experimenten (hoofdstuk 9) konden we bevestigen dat MEMRI geschikt is als methode om de structurele en functionele integriteit van het ruggenmerg *post mortem* vast te leggen. Omdat kwantitatieve MEMRI-maten sterk correleren met de mate van klinisch meetbare schade na trauma aan het ruggenmerg, kan MEMRI zoals wij het hebben ontwikkeld gezien worden als functionele beeldvorming van het ruggenmerg.

In hoofdstuk 10 werd MEMRI voor *in vivo* beeldvorming van het ruggenmerg bij muizen geoptimaliseerd. Hier konden we bewijzen dat MEMRI ook *in vivo* correleert met de functionele status van het ruggenmerg, zowel bij gezonde muizen als ook na trauma. Verder konden we laten zien dat middels MEMRI therapie-effecten van experimentele medicatie ter behandeling van traumatische veranderingen van het ruggenmerg objectief gemeten kunnen worden.

Conclusie

Samenvattend kan worden gezegd dat we twee methoden hebben ontwikkeld die het mogelijk maken het zenuwstelsel en vooral de verbindingen in de hersenen en het ruggenmerg zowel bij proefdieren (MEMRI) als ook bij mensen (DTI) te visualiseren. Deze methoden bieden nieuwe mogelijkheden om ziektes die het zenuwstelsel aantasten beter te diagnosticeren en te begrijpen. Verder bieden ze de mogelijkheid nieuw ontwikkelde medicijnen objectief te beoordelen.

Door middel van MEMRI konden de zenuwbanen en zenuwcentra worden afgebeeld. Omdat Mn^{2+} alleen in vitaal weefsel wordt opgenomen is het een goede surrogaatparameter voor neuronale

activiteit in het ruggenmerg. Zo konden we aantonen dat deze methode geschikt is als een *in vivo* meting van de effectiviteit van experimentele therapieën ter behandeling van de gevolgen van spinale traumata. Deze methode wordt momenteel ook door andere groepen benut en kan zich ontwikkelen tot een standaard test voor de preklinische beoordeling van therapieën voor spinaal trauma, *post mortem* en *in vivo*. Door de neurotoxiciteit is het helaas niet waarschijnlijk dat MEMRI in deze vorm voor humaan onderzoek kan worden toegepast.

Vergeleken met MEMRI is de interpretatie van DTI gecompliceerder. Alhoewel we konden laten zien dat het mogelijk is om zenuwbanen te visualiseren, konden we tegelijkertijd ook bewijzen dat de vorm van de gevonden banen sterk afhankelijk is van instellingen van de fiber tracking techniek. Dit is wellicht niet van groot belang bij onderzoek in de neurowetenschappen, maar klinisch, bijvoorbeeld voor DTI als potentiële methode voor de planning van operatieve ingrepen, is dit een groot probleem.

Ook de kwantitatieve waarden zijn bij MEMRI eenvoudiger te interpreteren. De opname van Mn^{2+} is een direct teken voor de vitaliteit van neuronaal weefsel. Veranderingen in DTI gerelateerde kwantitatieve waarden (o.a. ADC en FA) zijn naast de neuronale integriteit, van vele andere factoren zoals oedeem afhankelijk en leveren structurele informatie die niet direct met de functionaliteit van het weefsel overeenkomt. We konden laten zien, dat het mogelijk is door middel van de FA de infiltratieve groei van gliomen beter te detecteren, maar met de huidige methode kan maar een deel van het zenuwstelsel worden onderzocht.

Nieuw onderzoek is er op gericht, infiltratie van tumorweefsel driedimensionaal vast te stellen, maar dit wordt bemoeilijkt door een aantal beperkingen van DTI. Ten eerste worden kruisingen van zenuwbanen in het DTI model niet als zodanig herkent en in deze gebieden wordt een kunstmatig lage FA gemeten. Omdat een afname in FA ook bij infiltratie gemeten kan worden is het moeilijk in kruisingen een eenduidige uitspraak te kunnen doen over infiltratie. Verder kan druk van de tumor op het omgevende gezonde weefsel leiden tot een verhoging van de FA die pas later, door Wallerse degeneratie, tot een afname in de FA leidt. Ook in gebieden met oedeem kan het moeilijk zijn neuronale schade en

oedeemeffecten van elkaar te onderscheiden.

Samenvattend kan worden gezegd dat de kwantitatieve waarden die aan DTI ontleend worden voorzichtig moeten worden geïnterpreteerd maar dat ze tevens waardevolle informatie kunnen leveren. DTI is een nuttige methode voor humaan *in vivo* onderzoek naar de normale ontwikkeling van het brein en afwijkingen hiervan. Tevens kan het worden ingezet bij de detectie van neurodegeneratieve ziektes en hersentumoren.

List of publications

- Intravoxel Incoherent Motion MRI for the Differentiation Between Mass Forming Chronic Pancreatitis and Pancreatic Carcinoma. Klauß M, Lemke A, Grünberg K, Simon D, Re TJ, Wente MN, Laun FB, Kauczor HU, Delorme S, Grenacher L, **Stieltjes B. Invest Radiol.** 2011 Jan;46(1):57-63.
- Biopsy Targeting Gliomas: Do Functional Imaging Techniques Identify Similar Target Areas? Weber MA, Henze M, Tüttenberg J, **Stieltjes B**, Meissner M, Zimmer F, Burkholder I, Kroll A, Combs SE, Vogt-Schaden M, Giesel FL, Zoubaa S, Haberkorn U, Kauczor HU, Essig M. **Invest Radiol**. 2010 Sep 8. [Epub ahead of print]
- Automated MR morphometry to predict Alzheimer's disease in mild cognitive impairment. Fritzsche KH, **Stieltjes B**, Schlindwein S, van Bruggen T, Essig M, Meinzer HP. Int J Comput **Assist Radiol Surg.** 2010 May 4. [Epub ahead of print]
- The hematopoietic factor granulocyte-colony stimulating factor improves outcome in experimental spinal cord injury. Pitzer C, Klussmann S, Krüger C, Letellier E, Plaas C, Dittgen T, Kirsch F, **Stieltjes B**, Weber D, Laage R, Martin-Villalba A, Schneider **A. J Neurochem.** 2010 May;113(4):930-42. Epub 2010 Feb 25.
- Opportunities and pitfalls in the quantification of fiber integrity: what can we gain from Q-ball imaging? Fritzsche KH, Laun FB, Meinzer HP, **Stieltjes B. Neuroimage.** 2010 May 15;51(1):242-51.
- Gray Matter Alterations in First-Admission Adolescents with Schizophrenia. Henze R, Brunner R, Thiemann U, Parzer P, Richterich A, Essig M, Resch F, **Stieltjes B. J Neuroimaging.** 2010 Jun 21. [Epub ahead of print]
- Reduced prefrontal and orbitofrontal gray matter in female adolescents with borderline personality disorder: Is it disorder specific? Brunner R, Henze R, Parzer P, Kramer J, Feigl N, Lutz K, Essig M, Resch F, **Stieltjes B. Neuroimage.** 2009 Aug 4. [Epub ahead of print]
- Variational Principles in Image Processing and the Regularization of Orientation Fields. Cisternas J, Gálves M, **Stieltjes B**, Laun FB. **International Journal of Bifurcation and Chaos**, 2009, Aug (8), 2705-2716
- Image Guided Personalization of Reaction-Diffusion Type Tumor Growth Models Using Modified Anisotropic Eikonal Equations. Konukoglu E, Clatz O, **Stieltjes B**, Mandonnet E, Delingette H, Ayache N. **IEEE Trans Med Imaging**. 2010 Jan;29(1): 77-95. Epub 2009 Jul 14.
- An *in vivo* verification of the intravoxel incoherent motion effect in diffusion-weighted imaging of the abdomen. Lemke A, Laun FB, Simon D, **Stieltjes B**, Schad LR. **Magn Reson Med.** 2010 Dec;64(6):1580-5.
- Novel spherical phantoms for Q-ball imaging under *in vivo* conditions.

Moussavi-Biugui A, **Stieltjes B**, Fritzsche K, Semmler W, Laun FB. Magn Reson Med. 2010 Aug 25. [Epub ahead of print].

- Longitudinal changes in fiber tract integrity in healthy aging and mild cognitive impairment: a DTI follow-up study. Teipel SJ, Meindl T, Wagner M, **Stieltjes B**, Reuter S, Hauenstein KH, Filippi M, Ernemann U, Reiser MF, Hampel H. **J Alzheimers Dis.** 2010;22(2):507-22.

- On the effects of dephasing due to local gradients in diffusion tensor imaging experiments: relevance for diffusion tensor imaging fiber phantoms. Laun FB, Huff S, **Stieltjes B. Magn Reson Imaging.** 2009 May;27(4):541-8. Epub 2008 Oct 31.

- How background noise shifts eigenvectors and increases eigenvalues in DTI. Laun FB, Schad LR, Klein J, **Stieltjes B. MAGMA.** 2009 Jun;22(3):151-8. Epub 2008 Dec 9.

- Differentiation of pancreas carcinoma from healthy pancreatic tissue using multiple b-values: Comparison of apparent diffusion coefficient and intra voxel incoherent motion derived parameters. Lemke A, Laun FB, Klauß M, Re T J, Simon D, Delorme S, Schad L, **Stieltjes, B. Invest Radiol.** 2009 Dec;44(12):769-75.

- Sensory function in severe semilobar holoprosencephaly. Liasis A, Hildebrand D, Clark C, Katz X, Gunny R, **Stieltjes B**, Taylor D. **Neurocase.** 2009 Jan 19:1-9.

- Reproducible evaluation of spinal cord DTI using an optimized inner volume sequence in combination with probabilistic ROI analysis. Laun F, **Stieltjes B**, Schlüter M, Rupp R, Schad LR. **Z Med Phys.** 2009;19(1):11-20.

- Diffusion weighted imaging in medicine. **Stieltjes B. Z Med Phys.** 2009;19(1):1.

- Manganese Enhanced Magnetic Resonance Imaging in a Contusion Model of Spinal Cord Injury in Rats- Correlation with Motorfunction. Walder N, Petter A, Redl H, Essig M, **Stieltjes B. Invest Radiol**, May;43(5):277-83.

- MRI for identification of progression in brain tumors: from morphology to function. Weber MA, Giesel FL, **Stieltjes B. Expert Rev Neurother.** 2008 Oct;8(10):1507-25.

- Diffusion tensor imaging in ALS using a new probabilistic mixture model for fiber Integrity quantification. Schimrigk S, Bellenberg B, Schlüter M , **Stieltjes B**, Drescher R, Lukas K, Hahn H, Przuntek H, Köster O. AJNR **Am J Neuroradiol.** 2007 Apr; 28(4): 724-30

- Functional imaging for brain tumors (Perfusion, DTI and MR spectroscopy). Essig, M., Giesel, F, **Stieltjes B**, Weber MA. **Radiologe.** 2007 May 16

- Treatment options for arteriovenous malformations. Weber MA, Ahlhelm F, Essig M, Reith W, **Stieltjes B. Radiologe**, 2007 Okt; 47(10): 893-9

- Comparison of manual direct and automated indirect measurement of hippocampus Using magnetic resonance imaging. Giesel FL, Thomann PA, Hahn HK, Politi M, **Stieltjes B**, Weber MA, Pantel J, Wilkinson ID, Griffiths PD, Schröder J, Essig M. **EurJ Radiol.** 2008 May;66(2):268-73. Epub 2007 Jul 23.

- *In vivo* assessment of damage and functional improvement following spinal cord

injury using manganese-enhanced MRI. **Stieltjes B**, Klussmann S, Martin-Villalba A, Bock M, Edler L, Krammer PH, Kauczor HU, Essig. M. **Magn Reson Med** 2006 May;55(5):1124-31

- Diffusion Tensor Imaging in Primary Brain Tumors: Reproducible Quantitative Analysis of Corpus Callosum Infiltration and Contralateral Involvement Using a Probabilistic Mixture Model. **Stieltjes B**, Schlüter M, Didinger B, Weber MA, Hahn HK, Parzer P, Rexilius J, Konrad-Verse O, Peitgen HO, Essig M. **Neuroimage** 2006 Jun; 31(2):531-42

- Functional magnetic resonance imaging for defining the biological target volume. Kauczor HU, Zechmann C, **Stieltjes B**, Weber MA. **Cancer Imaging.** 2006 Jun;1;6:51-5

- Detection of Tumor Infiltration in Axonal Fiber Bundles Using Diffusion Tensor Imaging. Schlüter M, **Stieltjes B**, Hahn HK, Rexilius J, Konrad-Verse O, Peitgen H-O. **Int J Medical Robotics and Computer Assisted Surgery.**2005; 1(3): 80-86

- Intracerebral manifestation of an atypical monoclonal plasma cell hyperplasia depicted by MR perfusion and diffusion tensor imaging and MR spectroscopy. Weber MA, Viehoever A, **Stieltjes B**, Zoubaa S, Wildemann B, Baudendistel K, Kauczor HU. AJR **Am J Roentgenol.** 2005 Sep;185(3):784-7.

- Neutralization of CD95 ligand promotes regeneration and functional recovery after spinal cord injury. Demjen D, Klussmann S, Kleber S, Zuliani C, **Stieltjes B**, Metzger C, Hirt UA, Walczak H, Falk W, Essig M, Edler L, Krammer PH, Martin-Villalba A. **Nat Med.** 2004 Apr;10(4):389-95.

- Perfusion MRI in CNS disease: current concepts. Essig M, Giesel F, Le-Huu M, **Stieltjes B**, von Tengg H, Weber MA. **Neuroradiology.** 2004 Dec;46 Suppl 2:s201-7

- Diffusion tensor imaging. Theory, sequence optimization and application in Alzheimer's disease. **Stieltjes B**, Schluter M, Hahn HK, Wilhelm T, Essig M. (2003) **Radiologe.** 2003 Jul;43(7):562-5.

- Imaging cortical association tracts in the human brain using diffusion-tensor-based Axonal tracking. Mori S, Frederiksen K, van Zijl PC, **Stieltjes B**, Kraut MA, Solaiyappan M, Pomper MG (2002). **Magn Reson Med.** Feb;47(2):215-23.

- Brain white matter anatomy of tumor patients evaluated with diffusion tensor imaging. Mori S, Frederiksen K, van Zijl PC, **Stieltjes B**, Kraut MA, Solaiyappan M, Pomper MG. (2002) **Ann Neurol.** Mar;51(3):377-80

- Diffusion tensor imaging and axonal tracking in the human brainstem. **Stieltjes B**, Kaufmann WE, van Zijl PC, Fredericksen K, Pearlson GD, Solaiyappan M, Mori S. (2001). **Neuroimage.** Sep;14(3):723-35.

- *In vivo* visualization of human neural pathways by magnetic resonance imaging. Mori S, Kaufmann WE, Pearlson GD,Crain BJ, **Stieltjes B**, Solaiyappan M, van Zijl PC. **Ann Neurol.** 2000 Mar;47(3):412-4.

Curriculum Vitae

Bram Stieltjes werd op 7 november 1974 geboren te Ede. In 1993 behaalde hij het eindexamen vwo waarna hij met de studie Medische Biologie aan de Vrije Universiteit in Amsterdam begon. Na het behalen van de propedeuse in 1994, startte hij met de studie Geneeskunde aan de Erasmus Universiteit in Rotterdam. Tijdens deze studie volgde hij meerdere buitenlandse stages. In 1997 volgde hij, in het kader van een Erasmus beurs, een zes weken durende stage Klinische Oncologie aan de University of Nottingham in Engeland (Prof. Charmichael). Daarop volgde in 1999 in het kader van een Sokrates beurs een drie maanden durende klinische stage radiologie aan de Universität Heidelberg in Duitsland (Prof. Kaufmann) en in het kader van een beurs van de Johns Hopkins University, een 6 maanden durende wetenschappelijke stage bij de afdeling Experimental MRI aan de Johns Hopkins University (Prof. Mori/ Prof. v. Zijl). Na het behalen van het doctoraalexamen in 1999 volgde een periode van 6 maanden onderzoek als Research Fellow aan de Johns Hopkins University wederom op de afdeling Experimental MRI (Prof. Mori).

In 2002 behaalde hij het artsexamen aan de Erasmus Universiteit in Rotterdam. In dat zelfde jaar begon ook een gecombineerd traject van wetenschappelijk onderzoek en opleiding tot radioloog aan de afdeling Radiologie van het Deutsche Krebschforschungszentrum (DKFZ) in Heidelberg (Prof. van Kaick, Prof. Kauczor, Prof. Delorme, Prof. Essig).

In 2005 won Stieltjes de Contrast Media Research Young Investigator Award voor de in dit proefschrift beschreven methode voor MEMRI van het ruggenmerg. Verder werd voor het werk aan de in dit proefschrift beschreven methode voor infiltratie bij gliomen in 2008 de Kurt Decker Preis voor onderzoek in neuroradiologie uitgereikt door de Duitse Vereniging voor Neuroradiologie. In 2009 won hij de International Cancer Imaging Research Award voor de presentatie "Diagnosis and differentiation of pancreatic lesions using DWI-based IVIM-imaging", uitgereikt door de International Cancer Imaging Society.

214